

# Development of a GEM Based Time Projection Chamber Prototype Using a Pixelized Readout System

DISSERTATION

zur Erlangung des akademischen Grades eines  
Doktors der Naturwissenschaften  
(Dr. rer. nat.)

vorgelegt von

**M.Sc. Saiqa Shahid,**

geboren in Akora Khattak (Pakistan),

eingereicht bei der Naturwissenschaftlich-Technischen Fakultät  
der Universität Siegen

Siegen 2014



# Development of a GEM Based Time Projection Chamber Prototype Using a Pixelized Readout System

DISSERTATION

zur Erlangung des akademischen Grades eines  
Doktors der Naturwissenschaften  
(Dr. rer. nat.)

vorgelegt von

**M.Sc. Saiqa Shahid,**

geboren in Akora Khattak (Pakistan),

eingereicht bei der Naturwissenschaftlich-Technischen Fakultät  
der Universität Siegen

Siegen 2014

---

Gutachter der Dissertation: Professor Dr. Ivor Fleck  
Professor Dr. Markus Risse  
Datum der Disputation: 23. September 2014

---

Gedruckt auf alterungsbeständigem holz- und säurefreiem Papier.

Lost but not forgotten...  
Daddy and Sayem



## ABSTRACT

---

A Time Projection Chamber (TPC) is an ideal candidate for the tracking system in experiments of particle physics as it has a low material budget and a large number of possible track points. Gas Electron Multipliers (GEMs) in combination with a highly segmented readout device give the possibility to achieve a very good performance in track reconstruction by getting good spatial and momentum resolutions.

A TPC prototype with a drift length of 30 cm, using a triple GEM stack for amplification and a CMOS chip (Timepix chip) as a readout has been successfully operated at the University of Siegen. The Timepix chip consists of  $256 \times 256$  identical elements, which can measure either time or charge of a particle track through the TPC. Each one of these pixels has a size of  $55 \mu\text{m} \times 55 \mu\text{m}$ .

In order to avoid charging up effects of the used GEMs and to maintain a constant gain during time, GEMs coated with a carbon layer, which is supposed to have a thickness of approx.  $0.1 \mu\text{m}$ , have been used. The resistivity of the diamond like carbon is in the range of  $10^{15} \Omega\text{m}$ . The gain of the GEMs can be also increased by reducing the spark production between both GEM sides, so that higher electric fields can be applied.





## ZUSAMMENFASSUNG

---

Die geringe Materialbelegung und die große Anzahl an Messpunkten zur Spurrekonstruktion machen eine Zeitprojektionskammer (TPC) zum idealen Kandidaten für die Verwendung in Teilchendetektoren. Gas-Electron-Multipliers (GEMs) in Verbindung mit einem hochauflösenden Ausleesesystem sorgen für eine hohe Effizienz des Detektors, was eine gute Orts- und Impulsauflösung möglich macht.

Eine TPC mit einer Länge von 30 cm und der Verwendung eines Stapels bestehend aus drei GEMs in Verbindung mit einem CMOS Chip (Timepix Chip) als Ausleesesystem konnte an der Universität Siegen erfolgreich in Betrieb genommen werden. Der Timepix Chip besteht aus  $256 \times 256$  identischen Elementen, die entweder die Ankunftszeit oder die Ladung einer Teilchenspur messen können. Jeder dieser Pixel hat eine Größe von  $55 \mu\text{m} \times 55 \mu\text{m}$ .

Um Effekte wie das elektrische Aufladen der Plastiksicht (Kaptonsicht) in GEMs zu vermeiden und eine zeitlich stabile Gasverstärkung zu erzielen, wurden GEMs verwendet, die mit einer dünnen Karbonschicht überzogen wurden, welche eine Schichtdicke von etwa  $0,1 \mu\text{m}$  besitzen sollte. Der spezifische Widerstand dieser Karbonschicht beträgt etwa  $10^{15} \Omega\text{m}$ . Durch die Reduzierung von elektrischen Entladungen zwischen der Ober- und Unterseite von GEMs kann die maximale Verstärkung erhöht werden, da in diesem Fall höhere elektrische Feldstärken in den GEMs erzeugt werden können.



# CONTENTS

---

1	INTRODUCTION	1
2	PARTICLE PHYSICS	3
2.1	The Standard Model of Particle Physics . . . . .	3
2.1.1	Particles in the Standard Model . . . . .	3
2.1.2	Interactions of Particles . . . . .	4
2.1.3	Unanswered Questions of the Standard Model . . . . .	6
2.1.4	Supersymmetrical Standard Model . . . . .	7
2.2	The International Linear Collider . . . . .	8
2.2.1	Motivation for a Linear Collider . . . . .	8
2.2.2	Technical Parameters of the International Linear Collider (ILC) . . . . .	9
2.2.3	International Large Detector . . . . .	11
2.3	Physics at the ILC . . . . .	12
2.3.1	Higgs Mechanism at ILC . . . . .	13
2.3.2	supersymmetry (SUSY) at ILC . . . . .	15
3	INTERACTION OF PARTICLES WITH MATTER	17
3.1	Interaction of Photons with Gas Atoms . . . . .	17
3.1.1	Double Photon Absorption . . . . .	19
3.2	Interaction of Charged Particles with Gas Atoms . . . . .	20
3.2.1	Interaction of Heavy Charged Particles with Gas Atoms	20
3.2.2	Interaction of Light Charged Particles with Gas Atoms .	21
3.2.3	Number of Created Electron-Ion Pairs . . . . .	22
3.3	Motion of Charge Carriers in Gases . . . . .	23
3.3.1	Drift Velocity of Electrons . . . . .	23
3.3.2	Drift of Ions . . . . .	24
3.4	Diffusion . . . . .	24
3.4.1	Diffusion in Electric Fields . . . . .	26
3.4.2	Diffusion in Magnetic Fields . . . . .	26
3.5	Properties of Different Gas Mixtures . . . . .	28
3.5.1	Conditions for the Nobel Gas . . . . .	28
3.5.2	Conditions for the Quencher . . . . .	29
4	TIME PROJECTION CHAMBER	31
4.1	Working Principle of a Time Projection Chamber . . . . .	31

## Contents

4.2	Primary Ionisation in the TPC . . . . .	33
4.3	Methods of Gas Amplification . . . . .	34
4.3.1	Multi-Wires . . . . .	34
4.3.2	MicroMegas . . . . .	35
4.3.3	Gas Electron Multipliers . . . . .	36
4.3.4	GEM Stack . . . . .	40
4.3.5	Discharge Possibility . . . . .	41
4.3.6	Carbon Coated GEMs . . . . .	42
4.4	Ion Back Drift in TPCs . . . . .	43
4.5	Possible Readout Systems for TPC . . . . .	44
4.5.1	Readout with Pads . . . . .	44
4.5.2	Readout with Pixel chip . . . . .	45
4.6	Advantages of a TPC . . . . .	45
4.7	TPC for the International Large Detector . . . . .	46
5	EXPERIMENTAL SETUP IN SIEGEN . . . . .	49
5.1	High Voltage and Gas System . . . . .	49
5.1.1	High Voltage System . . . . .	49
5.1.2	Gas System . . . . .	51
5.2	The Test Chamber . . . . .	52
5.2.1	Mechanical Overview . . . . .	53
5.2.2	Pad Plane for Signal Readout . . . . .	54
5.3	The TPC Prototype . . . . .	56
5.4	Properties of the GEMs used at Siegen . . . . .	57
5.4.1	Properties of Standard GEMs . . . . .	57
5.4.2	Properties of Carbon Coated GEMs . . . . .	59
5.5	The Timepix-Chip . . . . .	60
5.5.1	Internal Structure of the Timepix-Chip . . . . .	61
5.5.2	USB Readout System . . . . .	65
5.5.3	Virtex-6 FPGA ML605 . . . . .	66
5.5.4	Software for the Readout . . . . .	67
5.6	Scintillator Hodoscope for TPC Prototype . . . . .	67
5.7	Ionisation Methods . . . . .	69
5.7.1	UV-Laser . . . . .	69
5.7.2	X-Ray-Sources . . . . .	69
5.7.3	Beta-Ray-Sources . . . . .	70
5.7.4	Cosmic Muons . . . . .	70
6	CALIBRATION OF TIMEPIX CHIP . . . . .	73
6.1	Timepix Operating Software . . . . .	73
6.2	Threshold Equalisation . . . . .	75

6.3	Charge Calibration . . . . .	77
6.4	Timewalk Compensation . . . . .	79
6.5	Threshold Offset Calibration . . . . .	81
6.6	Time Delay Compensation . . . . .	82
7	CARBON COATED GEMS . . . . .	83
7.1	Creation of Carbon Layers . . . . .	83
7.2	Investigation of Carbon Coating . . . . .	84
7.3	Experimental Setup . . . . .	86
7.4	Pad Readout Calibration of Test Chamber . . . . .	87
7.5	Measurement of GEM Behaviours . . . . .	90
7.6	Long Time Measurements of Gain Stability . . . . .	95
8	DATA WITH TPC PROTOTYPE . . . . .	101
8.1	Calibration with USB device . . . . .	101
8.2	Data with USB Device . . . . .	103
8.2.1	Laser Measurements . . . . .	103
8.2.2	Source Measurements . . . . .	105
8.3	Data Taking with Virtex 6 Readout System . . . . .	106
8.3.1	Measurement of the Drift Velocity . . . . .	106
8.3.2	Measurements with Cosmic Muons . . . . .	112
8.4	MarlinTPC . . . . .	113
8.5	Data Analysis with MarlinTPC . . . . .	115
8.5.1	Conversion Chain . . . . .	115
8.5.2	Calibration Chain . . . . .	115
8.5.3	Reconstruction Chain . . . . .	116
8.5.4	Analysis Chain . . . . .	121
9	CONCLUSION AND OUTLOOK . . . . .	129
A	TOS COMMANDS . . . . .	131
A.1	Commands for Initialisation of Chip . . . . .	131
A.2	Commands for Threshold Equalisation . . . . .	131
A.3	Commands for Charge Calibration . . . . .	131
A.4	Commands for TimeWalk Compensation . . . . .	132
A.5	Commands for Triggered/Untriggered Measurement . . . . .	132
A.6	List of other Commands . . . . .	133
B	LCIO PARAMETERISATION . . . . .	135
B.1	Calculation of $d_0$ . . . . .	135
B.2	Calculation of $z_0$ . . . . .	135
B.3	Calculation of $\lambda$ . . . . .	136

## Contents

B.4	Calculation of $\phi$ . . . . .	137
C	CALIBRATION AND MEASUREMENT RESULTS	139
C.1	Charge Calibration for Test Chamber . . . . .	139
C.2	Charge Distributions for Different Voltages . . . . .	141
C.3	Time Distribution for Different Voltages . . . . .	142
D	TPC AT UNIVERSITY OF SIEGEN	143
D.1	Small Test Chamber . . . . .	143
D.2	Large TPC Prototype . . . . .	144
D.3	Printed Circuit Board as Base for Test Chamber . . . . .	145
D.4	Virtex 6 FPGA Setup . . . . .	146
E	DATA WITH TPC PROTOTYPE	147
E.1	Data with Virtex 6 using using cosmic muons . . . . .	147
F	CARBON COATING	149
F.1	Correlation between Gas Gain and Temperature resp. Pressure	149
F.2	Correlation between Gas Gain and GEM Voltage . . . . .	151
F.3	SICON Data Sheet . . . . .	152
F.4	Carbon Coating inside GEM Holes . . . . .	153

## LIST OF FIGURES

---

Figure 2.1	Unification of interactions in a supersymmetrical standard model . . . . .	8
Figure 2.2	Schematic picture of the International Linear Collider . . . . .	10
Figure 2.3	Concept view of the International Large Detector . . . . .	12
Figure 2.4	Quadrant side view of the ILD model with its sub detectors . . . . .	13
Figure 2.5	Cross sections of different physics processes available at the ILC . . . . .	14
Figure 2.6	Feynman diagram of Higgs-strahlung process . . . . .	15
Figure 2.7	Simulation of mass recoiling from decaying Z boson . . . . .	15
Figure 3.1	Interaction of photons with matter . . . . .	18
Figure 3.2	Specific energy loss $dE/dx$ of heavy particles inside a TPC . . . . .	22
Figure 3.3	The drift velocity of electrons . . . . .	24
Figure 4.1	Sketch of a TPC . . . . .	32
Figure 4.2	Schematic of a multi-wire chamber . . . . .	35
Figure 4.3	Schematic layout of a Micromegas . . . . .	36
Figure 4.4	Picture of GEM under the microscope . . . . .	37
Figure 4.5	Sketch of a standard CERN GEM with all necessary parameters . . . . .	38
Figure 4.6	Electric field lines between two GEM sides . . . . .	39
Figure 4.7	Gain of GEM stacks as a function of voltage difference . . . . .	41
Figure 4.8	Pad readout used for TPC at University of Siegen. . . . .	44
Figure 4.9	Spatial resolution of a GEM based TPC inside a magnetic field . . . . .	46
Figure 4.10	Drawing showing the main parts of the TPC for a future LC . . . . .	47
Figure 5.1	High voltage and gas system for the TPC Prototype . . . . .	50
Figure 5.2	Screen shot of the LabView Software . . . . .	51
Figure 5.3	Schematic of the gasmonitor . . . . .	52
Figure 5.4	Spectrum of the gas monitor for $\text{ArCH}_4$ . . . . .	53
Figure 5.5	Sketch of the test chamber . . . . .	55
Figure 5.6	Drawing of the test chamber at the University of Siegen . . . . .	55
Figure 5.7	Layout sketch of the pad readout from the test chamber . . . . .	56
Figure 5.8	Sketch of the TPC prototype . . . . .	57
Figure 5.9	Sketch of the Tomepix chip . . . . .	60
Figure 5.10	Complete Electronical Circuit inside one pixel of the Tomepix chip . . . . .	61

List of Figures

Figure 5.11	Graphical scheme of the $ToT$ and $ToA$ modes of the Timepix chip . . . . .	63
Figure 5.12	Picture of the USB device for the Timepix chip . . . . .	65
Figure 5.13	Photos of the FPGA card and the intermediate board . . . . .	66
Figure 5.14	Scheme of the working principle of the FPGA firmware [Lup14] . . . . .	67
Figure 5.15	Sketch of the hodoscope setup for the TPC prototype . . . . .	68
Figure 5.16	Momentum spectrum of cosmic muons on sea level . . . . .	71
Figure 5.17	Energy loss of MIPs in matter . . . . .	72
Figure 6.1	Mask pattern for Timepix calibration and data acquisition . . . . .	75
Figure 6.2	Output of TOS for the threshold equalisation . . . . .	76
Figure 6.3	Signal shape for the $ToT$ calibration . . . . .	77
Figure 6.4	Sample $ToT$ distribution for a test pulse with 200 mV signal height . . . . .	78
Figure 6.5	Plot of the average $ToT$ values from all pixels against signal height . . . . .	79
Figure 6.6	Time difference $\Delta T$ between two signals with different pulse heights . . . . .	80
Figure 6.7	Plots of the timewalk compensation. . . . .	80
Figure 6.8	Rectangular pulse shape for the S-Curve calibration . . . . .	81
Figure 6.9	Plots of the S-Curve calibration. . . . .	82
Figure 7.1	Setup scheme of the chamber for PACVD coating . . . . .	84
Figure 7.2	Comparison of the surface of a coated and an uncoated GEM . . . . .	85
Figure 7.3	Chemical structure of Kapton . . . . .	86
Figure 7.4	Analysis of the thickness of the carbon coating . . . . .	87
Figure 7.5	Electrical circuit of the calibration setup . . . . .	88
Figure 7.6	Screenshot of the oscilloscope for the calibration . . . . .	89
Figure 7.7	Linear fit for the plot of charge against MCA channel numbers . . . . .	89
Figure 7.8	Gas gain of a single SICAN GEM for different mixing ratios . . . . .	91
Figure 7.9	Comparison of GEMs with coated and uncoated surfaces . . . . .	91
Figure 7.10	Gain of two carbon coated GEMs in a stack . . . . .	92
Figure 7.11	Comparison of gain stabilities for uncoated and SICAN coated GEMs . . . . .	93
Figure 7.12	Setup for determining the resistivity of a carbon coated GEM . . . . .	94
Figure 7.13	Comparison of currents for two different GEM coatings . . . . .	95



Figure 7.14	Comparison of gain stabilities for SICON and SICAN coated GEMs . . . . .	96
Figure 7.15	Fit through the gain stabilities for SICON and SICAN coated GEMs . . . . .	97
Figure 7.16	Changing of gain during time for coated and uncoated GEMs . . . . .	99
Figure 7.17	Atmospheric fluctuations and measured charge of GEMs	99
Figure 8.1	Threshold equalisation done by the Pixelman software	101
Figure 8.2	Sample calibration frame and distribution with the USB device . . . . .	102
Figure 8.3	Position of the entry and exit holes for the laser beam .	105
Figure 8.4	Signals for different distances between the laser and the GEMs . . . . .	106
Figure 8.5	Recorded laser signals with different frequencies . . . .	107
Figure 8.6	Recorded signals with different radioactive sources . .	108
Figure 8.7	Sample tracks with $^{90}\text{Sr}$ . . . . .	109
Figure 8.8	$ToA$ values for different gas mixtures with laser and photo diode . . . . .	110
Figure 8.9	Simulated drift velocities for different gas mixtures . .	111
Figure 8.10	Sample measurement of cosmic muons with the Virtex 6 readout . . . . .	113
Figure 8.11	Application of timewalk compensation on a cluster . .	117
Figure 8.12	Output of a sample event from the TimePixClusterFinderProcessor . . . . .	118
Figure 8.13	Output of the sample event for the cluster separation .	119
Figure 8.14	Working principle of the track finding with the Hough transformation . . . . .	120
Figure 8.15	Sketch of a track showing the LCIO track parameters .	122
Figure 8.16	Simulated diffusion constants for different gas mixtures	123
Figure 8.17	Calculation method to find the residuals $\sigma_N$ of a line fit	124
Figure 8.18	Example for the z-binning to calculate the spatial resolution . . . . .	125
Figure 8.19	Plot with for calculating the transversal diffusion coefficient . . . . .	125
Figure 8.20	Plot with for calculating the longitudinal diffusion coefficient . . . . .	125
Figure 8.21	Geometric distributions for different geometrical directions	126
Figure 8.22	Distributions for the track parameters calculated by Marlin	127
Figure 8.23	Number of clusters per drift length against drift distance	128
Figure C.1	Complete calibration histograms for test chamber . . .	140

## List of Figures

Figure C.2	Measurement of $ToT$ pixel distributions for different pulse heights . . . . .	141
Figure C.3	Measurements of $ToA$ pixel distributions for different pulse heights . . . . .	142
Figure D.1	Test chamber at the University of Siegen . . . . .	143
Figure D.2	TPC prototype at the University of Siegen . . . . .	144
Figure D.3	PCB with the pads for the test chamber. One can see the conductor path between the pads and the connectors for the amplifier. . . . .	145
Figure D.4	Connection scheme of the Timepix chip and the Virtex 6 card . . . . .	146
Figure E.1	Sample tracks with cosmic muons . . . . .	147
Figure F.1	Correlation between gas gain and temperature resp. pressure for carbon coated SICAN GEMs . . . . .	149
Figure F.2	Correlation between Gas Gain and Temperature resp. Pressure for uncoated GEMs . . . . .	150
Figure F.3	Comparison of GEMs with coated and uncoated surfaces	151
Figure F.4	Datasheet of SICON [Fra14] . . . . .	152
Figure F.5	Measurements to prove the carbon coating inside the GEM holes . . . . .	153

## LIST OF TABLES

---

Table 2.1	Three generations of fermions . . . . .	4
Table 2.2	Properties of particles in the standard model . . . . .	5
Table 2.3	Interactions between particles in the Standard Model .	6
Table 2.4	Design parameters of the ILC . . . . .	11
Table 3.1	Measured ion mobility of noble gas ions in their parent gas . . . . .	25
Table 3.2	Gas properties for different gases calculated with Magboltz	29
Table 4.1	Ionisation gas parameters frequently used chamber gases	33
Table 4.2	Resolution goals and design parameters for a TPC in the ILD . . . . .	48
Table 5.1	List of materials for the Time Projection Chamber (TPC) prototype . . . . .	58
Table 5.2	Connection pins of the USB device . . . . .	65
Table 5.3	Energies for different elements inside the variable x-ray- source . . . . .	69
Table 6.1	Setting of the Timepix DACs during calibration and data taking . . . . .	74
Table 6.2	Settings of pixel values in TOS . . . . .	75
Table 7.1	Experimental setup for testing one carbon coated GEM	87
Table 7.2	Experimental setup for testing a stack of two carbon coated GEMs . . . . .	88
Table 8.1	Parameters of the test measurement with USB device .	104
Table 8.2	Drift velocities for different gas mixtures . . . . .	111
Table 8.3	Parameters of the test measurement with the Virtex 6 Readout . . . . .	112



## LIST OF ACRONYMS

---

<b>ATLAS</b>	A Toroidal LHC Apparatus
<b>CMS</b>	Compact Muon Solenoid
<b>CSA</b>	Charge Sensitive Amplifier
<b>ILC</b>	International Linear Collider
<b>ILD</b>	International Large Detector
<b>ECAL</b>	Electromagnetic Calorimeter
<b>EWT</b>	Electroweak Theory
<b>FPGA</b>	Field Programmable Gate Array
<b>FTD</b>	Forward Tracking Detector
<b>GEM</b>	Gas Electron Multiplier
<b>GUT</b>	Grand Unified Theory
<b>HCAL</b>	Hadronic Calorimeter
<b>LCIO</b>	Linear Collider Input/Output
<b>LEP</b>	Large Electron-Positron Collider
<b>LHC</b>	Large Hadron Collider
<b>Linac</b>	Linear Collider
<b>LSP</b>	Lightest Supersymmetric Particle
<b>Marlin</b>	Modular Analysis & Reconstruction for the LINear Colider
<b>MCA</b>	multi-channel-analyser
<b>MSSM</b>	Minimal Supersymmetric Standard Model
<b>NLSP</b>	Next to Lightest Supersymmetric Particle
<b>PCB</b>	Printed Circuit Board

**QCD** Quantum Chromodynamics  
**QED** Quantum Electrodynamics  
**SIT** Silicon Strip Detector  
**SLAC** Stanford Linear Accelerator Center  
**SM** Standard Model of Particle Physics  
**SUSY** supersymmetry  
**TOS** Timepix Operating Software  
**TPC** Time Projection Chamber  
**TSL** Timepix Synchronization Logic  
**VTX** Vertex Detector

## INTRODUCTION

---

One of the most successful theories in physics is the Standard Model of particle physics. It is tested successfully by many experiments such as particle detectors for accelerators or cosmic showers. One example is the Large Hadron Collider (LHC) at CERN in Switzerland, which is a circular accelerator for protons. However at very high energies this accelerator concept is not practicable for lighter particles like electrons or positrons because of their energy loss due to cyclotron radiation. Therefore a new accelerator called International Linear Collider (ILC) is planned to be built in Japan, with which it will be possible to collide electrons and positrons with center-of-mass energies between 250 GeV and 1 TeV.

The details of the particles inside the Standard Model and their interactions are presented in chapter 2. There it will be shown, where the limits of the actual models are and what cannot be described successfully until now. This chapter will also give a short summary of the ILC. Furthermore the different detector concepts for the ILC will be shown and the reason will be explained, why a Time Projection Chamber (TPC), as it is built in a small scale at the University of Siegen, is a useful part of the new detector concept.

In order to understand the concept of a TPC, the basic interactions between matter and charged particles resp. photons will be presented in chapter 3. An important part of this chapter is the drift of electrons and ions inside gas volumes. Therefore it is necessary to go into details regarding the diffusion of particles in case of applied electrical and magnetic fields. The following chapter 4 then deals with the working principle of a TPC in general and gives a short overview over the different gas amplification methods (such as Gas Electron Multipliers (GEMs) and MicroMegas) and readout methods (e.g. pad planes and pixel chips), which have been developed during the last decades.

Chapter 5 gives a summary of the technical parameters of the two TPCs, which are currently used at the University of Siegen, including the description of the peripherals like high voltage supplies and different electronic devices. The Timepix chip that is used as a pixelised readout for the TPC prototype at the University of Siegen, will be also explained very detailed, which leads to the description of the calibration of this chip in chapter 6 including all necessary steps for taking measurements. This calibration is necessary, because of the non-linear correlation between the charge resp. time informations of the Timepix chip and the actual physical units.

## INTRODUCTION

The most important part of this thesis is the investigation of **GEMs**, which have been coated with a thin layer of diamond like carbon. The thickness of this layer is  $0.1\ \mu\text{m}$ , which leads to a conduction between the two **GEM** sides with a high resistance. The reason for this coating is the creation of **GEMs**, which are highly resistant against electrical discharges, while the other advantages of the used **GEMs** should not be changed.

With this coating it is also planned to get a higher gain stability, since the charging up effect of the plastic (Kapton) foil inside the **GEMs** could be avoided. The analysis of this coating and the measurements, which have been done with some sample **GEMs** inside a small test chamber at the University of Siegen, are presented in chapter 7. Even though the conducting layer leads to a lower gain, this disadvantage can be completely compensated by the possibility of creating higher electric fields inside the **GEM** holes to achieve effectively a higher gain.

After inserting these **GEMs** into the TPC prototype a long time data taking with cosmic muons has been performed. The results of these measurements and the analysis, which has been done inside the framework of MarlinTPC, are shown in chapter 8. The analysis showed similar results to normal **GEMs** especially in the case of diffusion and hits per measured track. This gives a motivation to do further studies on **GEMs** with coatings like carbon or other less conducting materials.

The thesis ends with a summary of the performance analysis of the TPC, which gives an outlook on the plans for future measurements and changes inside the existing system. These changes include the usage of more than one Timepix chip for the readout system and other types of **GEMs** like ceramic based materials.



## PARTICLE PHYSICS

---

### 2.1 THE STANDARD MODEL OF PARTICLE PHYSICS

The physics of elementary particles, which is known until now, can be described by the Standard Model of Particle Physics (SM). Within the last decades, particle physics has been developed to a consistent theory to describe the constituents of matter and the forces acting between them up to energies of the order of 100 GeV. The SM consists of 12 elementary particles (so called fermions with half integer spin) and 4 vector bosons (with integer spin), which are responsible for the couplings of these particles. More comprehensive introductions to particle physics and quantum field theories can be found in [Weio4]. The SM was tested by many accelerator- and non-accelerator-experiments and is the most successful theory in particle physics. This chapter gives an overview of the current understanding of interactions between elementary particles inside the SM.

#### 2.1.1 *Particles in the Standard Model*

According to the SM the fundamental particles, which are all fermions, can be divided into two groups: 6 leptons, having an electric charge of  $-1$  times the elementary charge  $e = -1.602 \cdot 10^{-19}$  C or 0, and 6 quarks, having an electric charge of either  $-1/3e$  or  $2/3e$ . The difference between quarks and leptons is, that a quark carries colour charge, while leptons are colour neutral. The leptons consist of the electron  $e$ , the muon  $\mu$ , the tau  $\tau$  and the corresponding electron-neutrino  $\nu_e$ , muon-neutrino  $\nu_\mu$  and  $\tau$ -neutrino  $\nu_\tau$ . The quarks include the up-quark  $u$ , the down-quark  $d$ , the strange-quark  $s$ , the charm-quark  $c$ , the top-quark  $t$  and the bottom-quark  $b$ . All of them are fermions with different masses. They are further divided into 3 generations as summarised in Table 2.1.

Each generation contains two quarks, one charged and one neutral lepton. The first generation contains the lightest particles, while the heaviest ones can be found in the third generation. For each of these elementary particles a partner with the opposite charge exists, which is called antiparticle and has the same mass (e.g. the positron  $e^+$  is the anti-particle of the electron  $e^-$ ). Quarks never appear independently, but always in combination of two or three

## 2. PARTICLE PHYSICS

Generation	1st	2nd	3rd
<b>Leptons</b>	$e, \nu_e$	$\mu, \nu_\mu$	$\tau, \nu_\tau$
<b>Quarks</b>	$u, d$	$s, c$	$t, b$

Table 2.1.: Three generations of Fermions in the SM.

together in the form of a hadron. A combination of two quarks (one quark and one anti-quark) is called meson and a combination of three quarks is called baryon. An example of a meson is the pion (also called  $\pi$ -meson), which exists in three different quark combinations:

$$\pi\text{-meson} = \begin{cases} |\pi^+\rangle & = |u\bar{d}\rangle \\ |\pi^0\rangle & = \frac{1}{\sqrt{2}}(|u\bar{u}\rangle + |d\bar{d}\rangle) \\ |\pi^-\rangle & = |d\bar{u}\rangle \end{cases}$$

The  $\pi$ -mesons are important for astroparticle physics, because they are produced in the atmosphere of the earth and decay into muons, which can be measured with particle detectors. The most famous hadron is the proton, which consists of two up-quark and one down-quark. Another hadron is the neutron, which consists of two down-quark and one up-quark. While neutrons and protons can form a nucleus, electrons can orbit around them in order to create an atom. In principle all known matter is created by atoms. The different elementary particles with their properties are listed in Table 2.2.

### 2.1.2 Interactions of Particles

The SM does not only describe all well-known elementary particles, but also the interactions (excluding gravitation) between them. There are four fundamental interactions conventionally known as the strong interaction, the weak interaction, the electromagnetic interaction and the gravitation. The particles, which carry these forces, are called vector bosons. All of them have an integer spin, which can be either 1 or 2. The photon, the  $W^\pm$ ,  $Z$  boson and gluon mediate the interaction between fermions. The vector bosons of the weak interactions are called  $Z$  and  $W^\pm$ . The photon ( $\gamma$ ) is responsible for electromagnetic interaction. Gluons ( $g$ ) mediate the strong interaction and for gravitation the mediator vector boson is known as the graviton ( $G$ ) which is not included in the SM. A boson, which is mediating gravitation, has not been observed until now.

## 2.1. The Standard Model of Particle Physics

Particles	Mass	Charge	Spin
e	0.511 MeV	-1	1/2
$\mu$	105.7 MeV	-1	1/2
$\tau$	1.777 GeV	-1	1/2
$\nu_e$	<2.2 eV	0	1/2
$\nu_\mu$	<0.17 MeV	0	1/2
$\nu_\tau$	<15.5 MeV	0	1/2
u	2.4 MeV	2/3	1/2
d	4.8 MeV	-1/3	1/2
c	1.27 GeV	2/3	1/2
s	104 MeV	-1/3	1/2
t	171.2 GeV	2/3	1/2
b	4.2 GeV	-1/3	1/2

Table 2.2.: Properties of the particles of the SM. The charge is given as multiples of the elementary charge  $e$  [Ber13].

A short overview of different interactions, including properties of the vector bosons, are given in Table 2.3. The range of gravitational and electromagnetic interactions are infinite. They decrease as a function of the distance from the particle. The range of the weak and strong interaction is limited nearly to the size of an atomic nucleus. The gravitation and weak interaction effect all existing particles, while the electromagnetic interaction is only valid for electrically charged particles.

The current SM allows to combine the electromagnetic and the weak interaction to one force, which is called Electroweak Theory (EWT). This theory, in which this combination is embedded, is called Quantum Electrodynamics (QED). Combining the EWT with the strong interaction leads to the Grand Unified Theory (GUT). Another important theory, which describes the strong interaction, is the Quantum Chromodynamics (QCD). It adds a new quantum number to the quarks, that is called colour. This was necessary, in order to describe particles with special quark combinations, which are otherwise forbidden by the Pauli Exclusion Principle.

Although the SM predicts only massless bosons a mass was observed for the W and Z bosons. Theoretically a mass can be introduced by symmetry breaking which is described by the Higgs mechanism [Hig64][Hig66]. This

## 2. PARTICLE PHYSICS

Interaction	Mediators	Spin	Mass	Charge	Range
Gravitation	G (gravitons)	2	0	0	Infinite
Electromagnetic	$\gamma$ (photons)	1	0	0	Infinite
Weak	$Z^0$ (bosons)	1	91.1876 GeV	0	Short $10^{-18}$
	$W^+$	1	80.385 GeV	+e	
	$W^-$	1	80.385 GeV	-e	
Strong	g (gluons)	1	0	0	Short $10^{-15}$

Table 2.3.: Interactions between particles in the SM. The graviton is still a hypothetical particle since it was not experimentally measured until now [Ber13].

introduces a Higgs field and the interaction of the fermions with the field generating their masses. The Higgs mechanism predicts an additional boson, called Higgs boson. The Higgs boson was discovered recently at the Large Hadron Collider (LHC) at CERN. Evidence for this was also found at the Tevatron [CDF12] at Fermilab. The measured masses of the Higgs boson at the ATLAS experiment is 126.0 GeV [ATL12] and at CMS 125.3 GeV [CMS12].

### 2.1.3 Unanswered Questions of the Standard Model

Almost all theoretical predictions of the SM have been proved experimentally, which is very important to establish the SM inside the physics community. However, there are some problems, which cannot be explained by this model:

- With the help of the GUT it was already possible to combine the weak, strong and electromagnetic interaction to one force, but the gravitation is too different from the other ones. Because of this problem aspects regarding gravitation cannot be explained inside this model. A quantum theory describing gravity based on the gauge principle is not yet available. All ideas, which have been developed until now, did not lead to a sufficient success.
- According to the Big Bang Model of our universe the amount of matter and antimatter was equal in the beginning of the universe. Most of the produced matter and antimatter annihilated, but a small amount of matter remained. The CP violation in the SM is not sufficient to explain the observed amount of matter. Another alternative mechanism of CP has to be introduced in the SM.

## 2.1. The Standard Model of Particle Physics

- According to some theories only a small fraction of the matter in the universe consists of SM particles. The rest consists of unknown constituents called *dark matter* [Sil05] and *dark energy* [Pla13]. This theory has been developed to explain unpredictable changes in the rotational speed of stars in the outer regions of the galaxy. Because of the fact, that almost all matter is combined in the center of a galaxy, the rotational speed should decrease for the outer stars. Since the measurements showed, that the speed is almost constant for every distance, a theory of unknown and invisible particles has been introduced. Because of the missing observation of this matter the name dark matter has been established.

### 2.1.4 Supersymmetrical Standard Model

In order to solve some of the problems, which are mentioned in section 2.1.3, the theory of supersymmetry (SUSY) has been developed [Zum74][Str74]. In the simplest supersymmetric theory, which is called Minimal Supersymmetric Standard Model (MSSM) every particle of the SM has a supersymmetric partner, i.e. every fermion has a new boson and every boson has a new fermion as a partner. For example the supersymmetric particle of the electron (which is a spin-half-fermion) is the spin-one-boson called selectron  $\tilde{s}$  (supersymmetric electron). Another example is the spin-one-boson gluon  $g$  with a gluino  $\tilde{g}$  as its supersymmetric partner. According to the rules of the MSSM this particle must be a fermion. Another prediction of supersymmetric theories is the existence of more than one Higgs boson.

Until now there is no experimental evidence for SUSY, since there is no experiment, which was able to measure supersymmetric particles. One explanation can be, that the masses of these supersymmetric particles are much higher than expected. In the theory of the SM the coupling constants are changing as a function of the energy. While in the SM there is no point, where all three coupling constants unite, there is such a point in the MSSM at around  $10^{14}$  TeV. This behaviour is illustrated in Figure 2.1. The MSSM is therefore an interesting theory, which may allow a deeper understanding of the fundamental interactions.

Another possible theory to describe the universe is the superstring theory. The disadvantage of this theory is, that it needs eleven dimensions and therefore includes a lot of free parameters. Until now it was also not possible to proof the predictions of this theory in any experiment and it is also not clear, whether this will ever happen in future.

## 2. PARTICLE PHYSICS

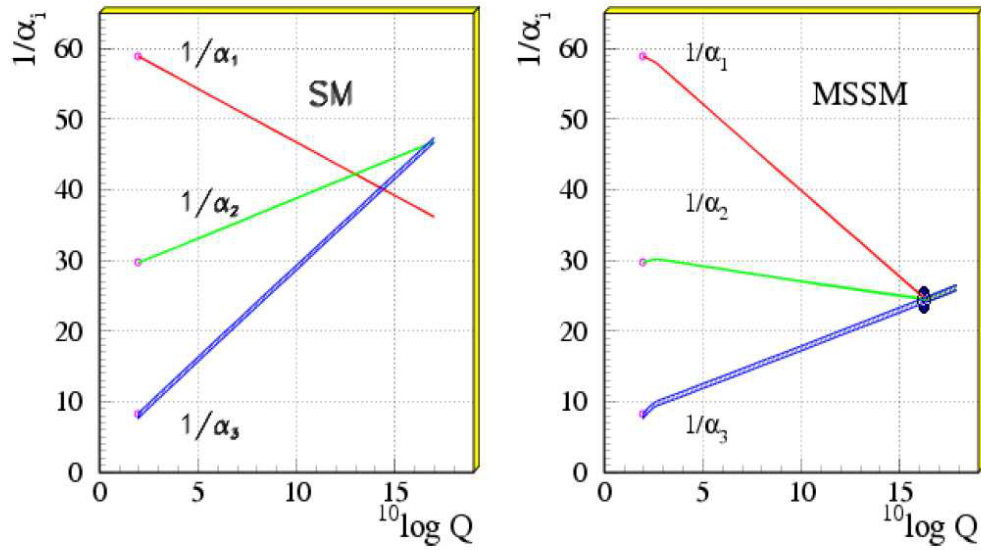


Figure 2.1.: The unification of all interactions in one point at a specific scale in a supersymmetric standard model [Yao06]. The graphs show the development of the coupling constants for the electromagnetic, weak and strong interaction for the SM (left) and the MSSM (right) as a function of the sliding scale  $Q$  in GeV. In the MSSM the three coupling constants have one intersection point, which does not exist in the SM.

## 2.2 THE INTERNATIONAL LINEAR COLLIDER

### 2.2.1 Motivation for a Linear Collider

Currently the **LHC**, which is a proton-proton-collider with a center-of-mass energy  $\sqrt{s}$  of up to 14 TeV is running at CERN in Switzerland. During the last years this accelerator produced some remarkable results. But the disadvantage of protons and hadrons in general is the fact, that these particles consist of quarks, so they are not elementary particles. This leads to much more complex and challenging data analysis, especially since **QCD** rules have to be taken into account. Also the initial state during the collision is much more uncertain compared to the usage of elementary particles.

In order to accelerate these protons until they reach a energy of 7 TeV, it is necessary to use the concept of a ring accelerator, where protons move continuously and gain more energy in every round. According to classical electrodynamics, every charged particle loses energy during acceleration,

which is called synchrotron radiation. The energy loss can be calculated according to the following equation

$$\Delta E = \frac{(Ze)^2 \beta^3 \gamma^4}{\epsilon_0 3 R} \propto \frac{E^4}{m_0^4 R} \quad (2.1)$$

where  $\gamma = E/(m_0 c^2)$  and  $\beta = v/c \approx 1$  describe the speed and energy of relativistic particles.  $\epsilon_0 = 8.8542 \cdot 10^{-12}$  is the permittivity of free space. The product  $Ze$  represents the total charge of the particle ( $Z = 1$  for electron and protons),  $e$  is the elementary charge,  $m_0$  is the rest mass of the particle and  $R$  is the radius of the storage ring. The amount of the energy loss of the particle per turn is inversely proportional to the fourth power of the rest mass of the used particles. From this formula one can see, that the method of circular acceleration to very high energies is not achievable for much lighter particles like electrons or positrons. In the former Large Electron-Positron Collider (LEP) at CERN it was possible to achieve a colliding energy of 210 GeV.

In order to analyse data taken from collisions with elementary leptons, one has to build a linear accelerator, which is already planned with the name ILC. In this case the electrons have to be accelerated up to their final energy in one step, because the acceleration stage is only passed once by the electrons. One of the greatest advantages of a collision between electrons and positrons as compared to protons is a very clean environment with a very small background. Furthermore the initial state is also well known.

### 2.2.2 Technical Parameters of the ILC

An important fact about the ILC is, that the collision energy will be much smaller compared to the LHC (200 - 500 GeV with a possibility to upgrade to 1 TeV). This characteristic is compensated by the fact, that any kind of strong interaction terms can be neglected. In order to achieve the maximum energy of  $\sqrt{s} = 1$  TeV, several extensions have been already planned for the ILC. The peak luminosity will be about  $2 \cdot 10^{34} \text{ cm}^{-2} \text{ s}^{-1}$ . An overview of the layout in Figure 2.2 explains the working principle of the ILC. The electrons are created by illuminating a photo cathode with a laser. After this they are accelerated to 5 GeV. After being emitted by the electron source, the electrons move forward into the damping rings, which have the task to focus and stabilise the electron beam. One advantage of this beam setup is, that the electrons and positrons can be polarised according to the desired measurement.

After transportation into the main Linear Collider (Linac), the electrons pass an undulator, in which they move in a helical track. Due to the bremsstrahlung the electrons emit photons with a high energy, which create electrons and

## 2. PARTICLE PHYSICS

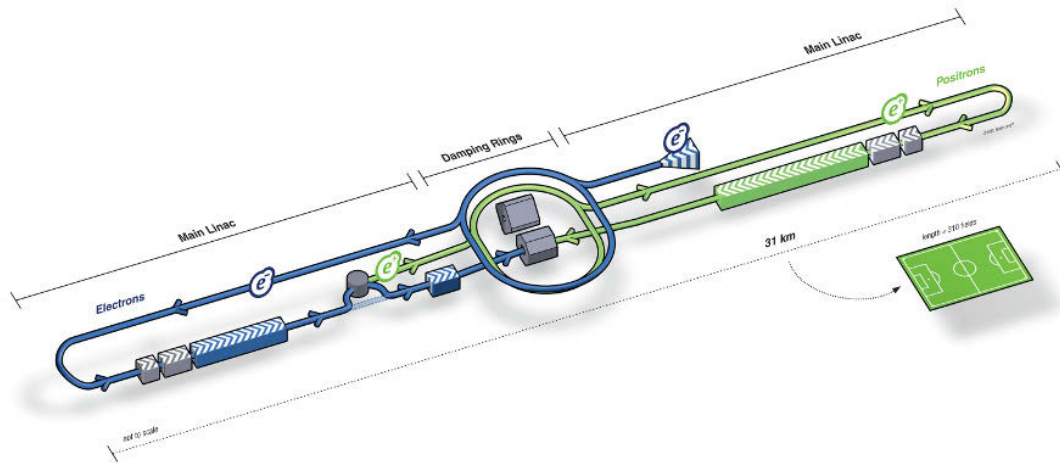


Figure 2.2.: Schematic picture of the International Linear Collider [ILC<sub>13</sub>]

positrons via pair production. After passing another damping ring the positrons will be transported into the main Linac. When both electrons and positrons are fully accelerated, it is planned to let them collide at a specific intersection point, which is surrounded by a detector. This detector has to detect and track the newly created particles from this collision. The mandatory conditions of such a detector will be discussed in section 2.2.3. Table 2.4 gives a short overview about the most important parameters of the ILC.

It will be a characteristic property of the ILC, that it can be run at any center-of-mass energy inside the given energy range and it can be upgraded to higher energies by extending the main Linacs to larger lengths. Depending on the processes, which need to be measured, the machine functionality can be also changed. The polarisation of the beams is preserved during the acceleration process in the ILC. For the electroweak processes at high energies, the polarisation is very important, because their coupling to the gauge bosons depend on it. In the ILC the event rates can be enhanced for certain processes by choosing the right polarisation of the beams. Due to the clean environment in the ILC, there are no pileup<sup>1</sup> events and zero underlying<sup>2</sup> events.

<sup>1</sup> In high-luminosity colliders it is very common, that one single bunch crossing creates a high amount of separate events, which are called pileup events.

<sup>2</sup> In a lepton collider the colliding particles annihilate completely, while in a hadron collider the remaining partons can also interact with each other and create additional events, which are called underlying events



Center Of Mass Energy	200 - 500 GeV
Luminosity	$2 \cdot 10^{34} \text{ cm}^{-2}\text{s}^{-1}$
Average Electric Current per Pulse	9 mA
Pulse Rate	5 Hz
Pulse Length	$\approx 1 \text{ ms}$
Number of Bunches per Pulse	1000 - 5400
Charge per Bunch	1.6 - 3.2 nC
Acceleration Gradient	31.5 MV/m
Beam Power	10.8 MW
Beam Diameter	640 nm
Total Power	230 MW
RF pulse length	1.6 ms MW

Table 2.4.: Design parameters of the ILC [Bar07]

### 2.2.3 International Large Detector

Different concepts of detectors for the ILC have been discussed during the last years. One of these detector concepts, which is under investigation for the ILC, is the International Large Detector (ILD) [ILC13]. At the ILC precision measurements to investigate the Higgs mechanism in detail and to study new physics like SUSY will be performed. The ILD with a TPC (see chapter 4) as a central tracking detector will be a promising candidate for this purpose. An overview of the complete detector concept can be seen in Figure 2.3.

The ILD is a shell-like detector comparable to the ATLAS or CMS at CERN. Its tracking system comprises several detectors. The innermost detector is a silicon pixel detector, which consists of a Vertex Detector (VTX) and a Silicon Strip Detector (SIT). VTX with a very good spatial resolution of better than  $3 \mu\text{m}$  is the nearest one to the beam. This high resolution is used to detect the secondary vertices, which is necessary to reconstruct final states including heavy flavour particles. The SIT is a silicon strip detector around the VTX. It is followed by a Forward Tracking Detector (FTD) in the end cap region, which provides coverage up to the beam pipe.

Around the pixel detector the largest of the tracking detectors is a TPC with the order of 200 measurement points. With the help of the TPC the particle tracks can be reconstructed and the momentum can be measured. Since it is a gaseous detector, the material budget for it is very low. The next detectors

## 2. PARTICLE PHYSICS

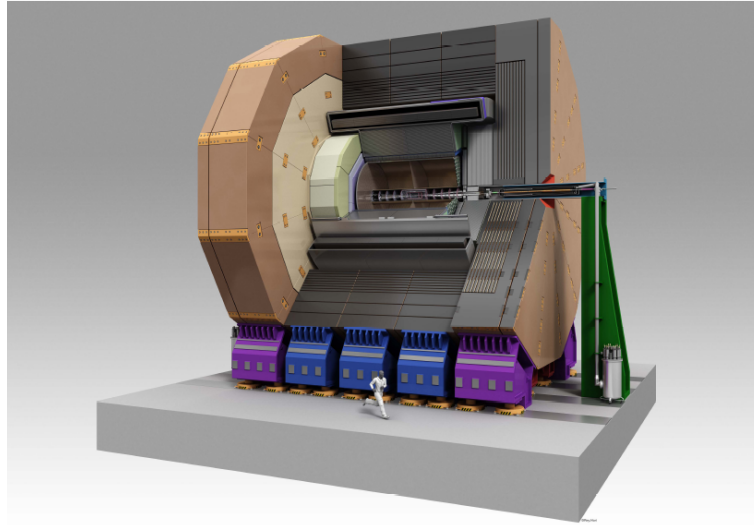


Figure 2.3.: A concept view of the International Large Detector [ILC13]

are the so called Electromagnetic Calorimeter (*ECAL*) and highly segmented Hadronic Calorimeter (*HCAL*). Inside these calorimeters the energy of the created hadrons and electrons can be measured by absorbing them completely.

The main material for the *ECAL* will be tungsten and silicon, while for the *HCAL* iron and active materials will be used. The whole detector will be placed in a superconducting magnet with a magnetic field of 3.5 T, which is essential for momentum measurements. An iron yoke returns the field lines and is additionally used as a muon detector with resistive plate chambers and as tail catcher for *HCAL* (see Figure 2.4).

Since the interaction between muons and matter is very weak, the muon detector system must be positioned in the outer regions of the *ILD*. The height of the *ILD* detector over all will be fifteen meter on a platform, that can be moved as whole in and out of the beam line. Summarising all the advantages of the *ILD*, it can be described as a multiple-purpose detector having a particle flow concept, i.e. every measurement in the detector is assigned to one particle. Such a capability of a detector will make particle identification very effectively.

### 2.3 PHYSICS AT THE ILC

Compared to the *LHC*, the center-of-mass energy of the *ILC* can be changed relatively easily and therefore a large variety of physics processes can be investigated. This makes it possible to study the cross-sections of the processes depending on the center-of-mass energy. The cross-sections of some of these

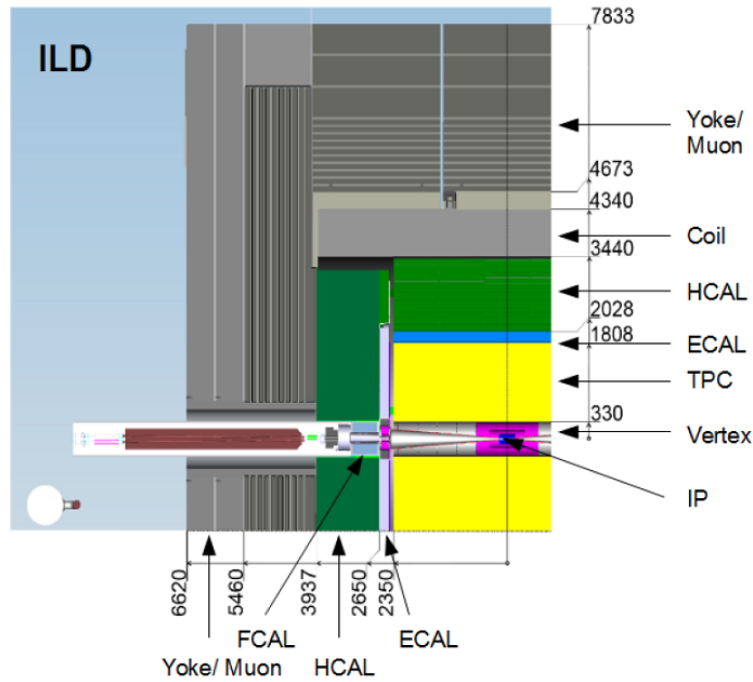


Figure 2.4.: Quadrant side view of the ILC model with its sub detectors. The dimensions are in mm [ILC13].

processes are shown in Figure 2.5. Unlike the LHC, which is designed for making discoveries at new energy scales, the ILC is planned to be a machine for precision measurements at lower energy. One possibility can be the study of the cross section of the Higgs-strahlung process at center-of-mass energies around 250 GeV (see section 2.3.1).

The processes including SUSY are expected at energy levels, which are higher than 500 GeV. By choosing different polarisations at the ILC, either the signal processes can be enhanced or the background can be suppressed, which leads to a better signal-to-noise ratio. This important feature makes the ILC more effective for the search of new physics, where certain SM processes can be reduced by selecting the correct polarisation [ILC132]. Therefore the ILC will serve not only as an extension to the physics searches of the LHC, but has the ability to do measurements beyond the known physics.

### 2.3.1 Higgs Mechanism at ILC

One of the most important processes, which is expected to be studied at the ILC, is the Higgs-strahlung process, where the mass of the Higgs boson can be

## 2. PARTICLE PHYSICS

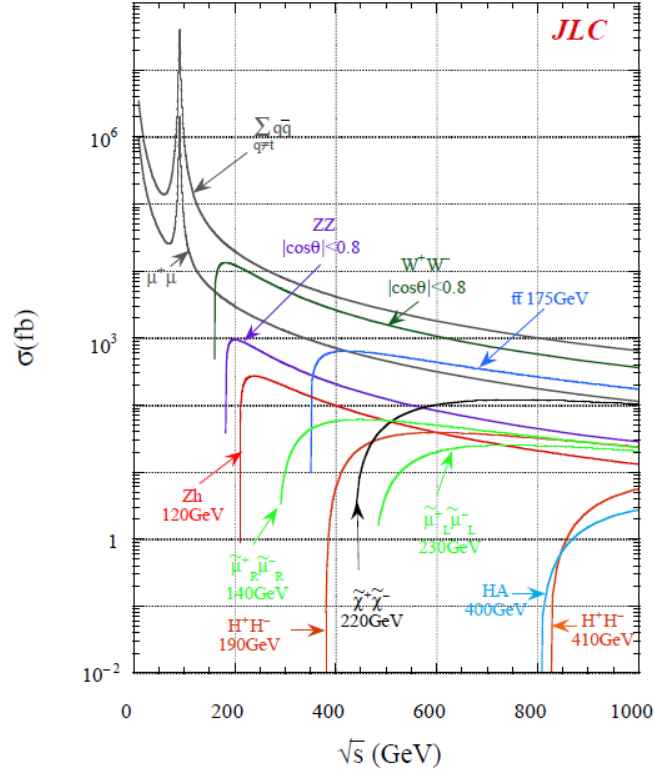


Figure 2.5.: Cross sections of different physics processes available at the ILC as a function of the center-of-mass energy [ACF13]

calculated by using the mass recoiling against the Z boson. The Higgs boson mass is given by

$$M_H^2 = s + M_Z^2 - 2E_Z\sqrt{s} \quad (2.2)$$

where  $\sqrt{s}$  is the center of mass energy,  $M_Z$  is the mass of the Z boson and  $E_Z$  its energy [HL10].

The mass of the Z boson is well known. Thus for a good mass resolution for the Higgs boson a high momentum resolution is necessary. The tracking system of the detector is responsible for the measurement of the particle momenta. In the ILC, a TPC will provide many measurement points and a long lever arm, which is also essential for a good momentum resolution. The advantage of using the recoil mass is, that the Higgs mass can be calculated without using the decay products of the Higgs boson. This method is therefore model independent and also invisible decay modes are taken into account. The Feynman diagram for the Higgs-strahlung is shown in Figure 2.6. The importance of the high momentum resolution is shown in Figure 2.7. The reconstructed recoil mass is plotted for two different momentum resolutions. It is observed at the LHC, that the Higgs particle also couples to the vector

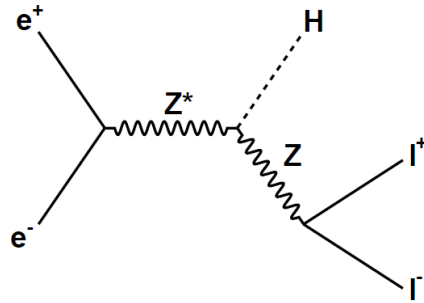


Figure 2.6.: Feynman diagram of Higgs-strahlung process

bosons. According to this the production processes will be available at the ILC [ATL12][CMS12].

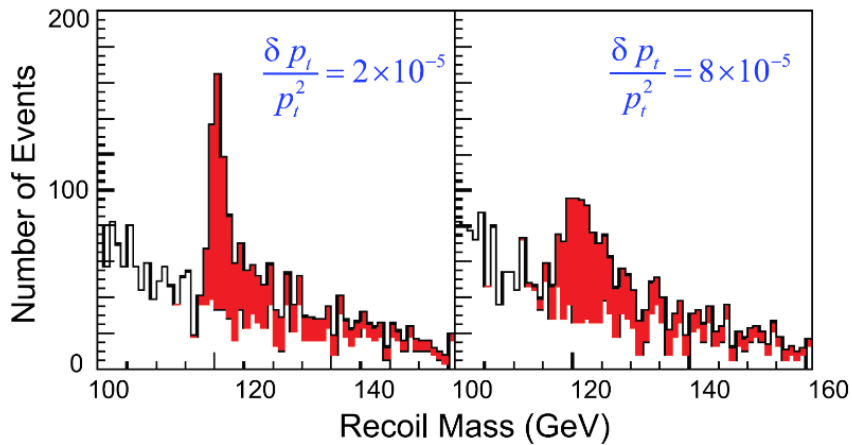


Figure 2.7.: Simulation of mass recoiling from Z boson decaying into two muons with a center-of-mass energy of 500 GeV with two different momentum resolutions. For the simulation a Higgs mass of 120 GeV has been assumed [Aar07].

### 2.3.2 SUSY at ILC

Current results from the LHC exclude large regions of the parameter space of SUSY. But still there are some models, that could be found in nature [Bae12][Hua12]. Most of the models involve charge differences between the two lightest supersymmetric particles (the Lightest Supersymmetric Particle (LSP) and the Next to Lightest Supersymmetric Particle (NLSP)) and include light charginos and neutralinos (masses below 200 GeV). These particles could be also produced at the ILC. SUSY as the most popular extension of the SM, is

## 2. PARTICLE PHYSICS

certainly one of the major interests at the *ILC*. The possible small mass splitting between LSP and NLSP (only a few GeV) is very challenging. The NLSP decays into LSP and a *SM* particle. As the mass splitting between LSP and NLSP could be very small, the *SM* particles have low momenta, which have to be measured precisely. This requires an efficient tracking and a good momentum resolution of the main tracking device, especially for tracks with a large curvature. The *ILC* will also be able to test, whether the lightest supersymmetric particle is maybe a sought-after candidate for dark matter.

## INTERACTION OF PARTICLES WITH MATTER

---

The detection of particles in high energy physics experiments is accomplished indirectly by analysing their interactions with the matter contained in the detector. In tracking detectors this is usually a thin layer of semiconducting material or gas. If a particle is passing through matter it loses energy. The amount and the way of the energy loss depends on the charge, type and total energy of the particle before the interaction and also on the type of matter, through which the particle travels. The energy loss  $dE$  per unit length  $dx$  can be quantified by the differential operator  $dE/dx$ . For gas the energy loss is normally smaller than for semiconducting material because of the matter density.

However for a TPC only the energy loss in combination with gas atoms has to be taken into account. A good description of how particles interact with matter can be seen in [PoPo07]. In the SM only the electromagnetic force is relevant for gas detectors, because of its large range, which makes electromagnetic interactions much more likely than strong or weak interactions. Therefore only photons or electrically charged particles can be used for ionisation inside gaseous detectors. Detectors for other particles like neutrons or neutrinos are much more complicated to build.

### 3.1 INTERACTION OF PHOTONS WITH GAS ATOMS

If a photon, which has no charge and no rest mass, is passing through a gas volume, there can be three types of interactions: photo effect (complete absorption by an electron of the atomic shell), Compton scattering (elastic scattering by quasi free atomic electrons) and pair production (creation of an electron-positron pair in the strong electric field near the atomic nucleus). The probability for each type of interaction to take place depends on the initial energy of the photon.

The graph in Figure 3.1 shows the schematic energy loss of photons while passing through a body of lead in dependence of the initial photon energy. Below 1 eV the energy is too low to ionise the atoms and the electrons inside the atoms can only move into excitation states. Above 1 eV ionisation of atoms can take place. Up to the energy of around 100 keV the probability for the photo effect of the photon dominates. In this case the photon vanishes completely by

### 3. INTERACTION OF PARTICLES WITH MATTER

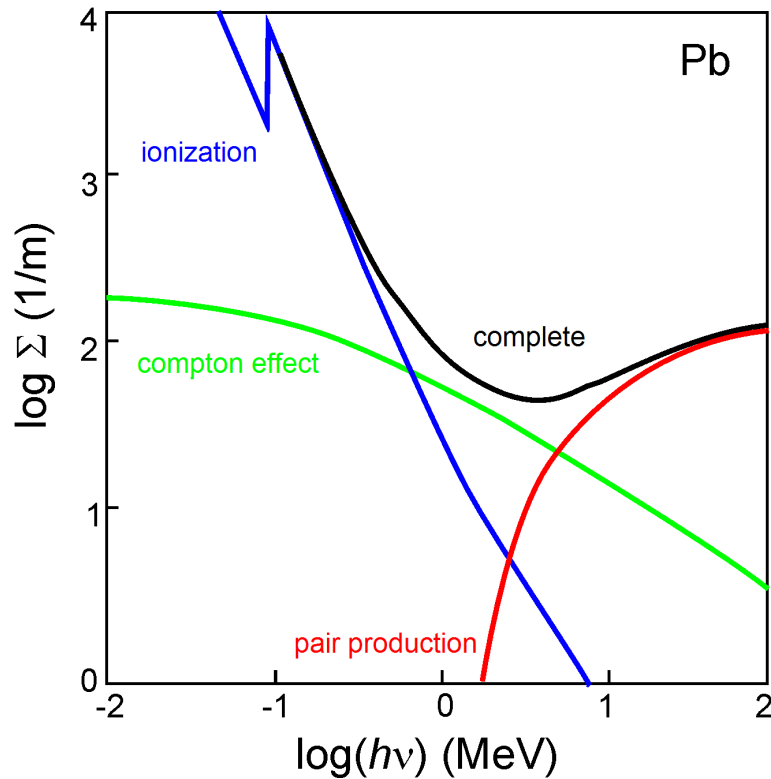


Figure 3.1.: The interaction of photons with matter [Ulr11]. For low energies the process of ionization due to the photoelectrical effect has the highest probability. For higher energies above 10 MeV the probability for pair production prevails.

transferring its energy to an electron, which is then able to leave the atomic shell.

The photon can also lose its energy via Compton scattering, i.e. the photon undergoes an elastic scattering with an electron inside the atomic shell and loses a specific amount of its energy. After this the photon still exists and is therefore able to make further scatterings.

For very high energies it is also possible for the photon to lose energy via pair production by creating a pair of one electron and one positron. It is obvious, that in this case the energy of the photon must be higher than the rest mass of the electron and positron together, i.e. at least 1.022 MeV. One can see, that above around 7 MeV the pair production becomes the most important interaction.



*Ionisation and Escape Peak*

If the energy  $E$  of a photon is high enough to ionise a gas atom by removing the electron from the inner shell ( $K$ -shell) with the binding energy  $E_K$ , this escape electron carries the energy  $E - E_K$  and ionises further gas atoms. The electrons from the outer shells fill that gap in the  $K$  shell and emit photons with that specific energy. If these photons pass through the detector without further interactions with the gas molecules, the other free electrons, which have been created by the escape electron, are the only ones, that can be detected by the detector readout system. The energy of the escape electron is always smaller than the one of an outer shell and characteristic for a specific gas in combination with a fixed photon energy.

3.1.1 *Double Photon Absorption*

Sometimes the energy of one single photon is not high enough to ionise atoms directly. The ionisation energy for Argon can be assumed as 15.7 eV. If a photon has less energy, it cannot ionise the atom directly but pushes it into an excited state. The time, in which the atom remains in this state before decaying back to the ground state can be defined as  $\tau$ . The probability for the atom to absorb the photon is  $\sigma_1$ , while  $\sigma_2$  is the probability to absorb a second photon. If  $F$  describes the flux of photons through the gas, then the complete cross section  $\sigma$  can be calculated as [Sad80]:

$$\sigma = \sigma_1 \sigma_2 \tau F \quad (3.1)$$

Typical values for the cross sections  $\sigma$  and time period  $\tau$  are  $\sigma_1 \approx \sigma_2 \approx 10^{-17} \text{ cm}^2$  and  $\tau \approx 0.1 \text{ fs}$ . The flux  $F$  can be calculated with the number  $n_\gamma$  of photons, the active beam area  $A$  and the pulse length  $T$  according to:

$$F = \frac{n_\gamma}{AT} \quad (3.2)$$

The number of created electrons in one pulse width is

$$n_e = q_i \sigma n_\gamma \quad (3.3)$$

with the area density  $q_i$  of the possible targets. By defining  $q_i = q p_i / p$  this leads the following equation:

$$n_e = q \frac{p_i}{p} \sigma n_\gamma \quad (3.4)$$

### 3. INTERACTION OF PARTICLES WITH MATTER

where  $p_i$  is the partial pressure and  $\rho$  the area density of the gas atoms. The number of photons  $n_\gamma$  is calculated with the energy  $E_\gamma$  of one photon and the energy  $E$  of one laser pulse by:

$$n_\gamma = \frac{E}{E_\gamma} \quad (3.5)$$

By inserting (3.1), (3.5) and (3.2) into equation (3.4) this leads to the following formula for the number of electrons:

$$n_e = \frac{E^2 \rho}{E_\gamma^2 A T} \sigma_1 \sigma_2 \tau p_i \quad (3.6)$$

If  $N$  is the number of necessary absorptions for one atom, the complete cross section is calculated as follows:

$$\sigma = \sigma_N \prod_{i=1}^{N-1} \sigma_i \tau_i F \sim F^{N-1} \sim E^{N-1} \quad (3.7)$$

The created signal height  $S$  is proportional to the amount of created electrons, which leads to the equation

$$S = \alpha n_e = \alpha \rho_i \sigma \frac{E}{E_\gamma} = \beta E^N \quad (3.8)$$

with the proportional constants  $\alpha$  and  $\beta$ .

### 3.2 INTERACTION OF CHARGED PARTICLES WITH GAS ATOMS

In the case of charged particles like electrons or muons, the effects of losing energy are totally different compared to photons. If a charged particle is passing through a gas volume, the atoms near its track can either be excited or even ionised due to the electromagnetic force. For gaseous detectors only these interactions, which lead to an ionisation of the gas atoms, are important. In this case a pair of one electron and one positively charged ion is created.

#### 3.2.1 Interaction of Heavy Charged Particles with Gas Atoms

In case of heavy particles (at least the rest mass of a muon) the energy loss of this particle inside matter can be described with the Bethe-Bloch formula [Grp08], which can be written as

$$-\frac{dE}{dx} = 4\pi N_A r_e^2 m_e c^2 z^2 \frac{Z}{A} \frac{1}{\beta^2} \left[ \ln \left( \frac{2m_e c^2 \gamma^2 \beta^2}{I} \right) - \beta^2 - \frac{\delta}{2} \right] \quad (3.9)$$

### 3.2. Interaction of Charged Particles with Gas Atoms

The variables can be defined as follows:

$Z$	Atom number of the gas atoms
$A$	Atom weight
$z$	Charge of the passing particle
$I$	Ionisation constant of the gas atoms
$v$	Speed of the particle
$r_e$	Electron radius (according to classical physics)
$m_e$	Mass of the electron
$N_A$	Avogadro constant
$\delta$	A parameter, which regards to the density effect
$\gamma$	The Lorentz factor of the theory of relativity

In the derivation of this formula it is assumed that heavy particles are not distracted by the electrons inside the absorber material. A plot of  $-dE/dx$  against the momentum of the particle shows a minimal energy loss for a specific momentum, which is different for each particle as one can see in Figure 3.2. The data has been taken with PEP4/9 at Stanford Linear Accelerator Center (SLAC).

#### 3.2.2 Interaction of Light Charged Particles with Gas Atoms

If the particle is not heavy enough, the derivation of the Bethe-Bloch formula has to be changed due to the interaction of the particle with the electrons inside the gas. In the case of electron-electron scattering the quantum mechanical indistinguishability also has to be taken into account since these are two identical particles. Therefore the derivation of the ionisation due to fast electrons inside a gas leads to the following equation [Grp08]:

$$-\left(\frac{dE}{dx}\right)_{\text{ionisation}} = 4\pi N_A r_e^2 m_e c^2 \frac{Z}{A} \frac{1}{\beta} \left[ \ln \left( \frac{2m_e v^2 \gamma^2}{I} \right) - 1 \right] \quad (3.10)$$

Another way of losing energy for light charged particles is due to bremsstrahlung, which is happening while the electron is scattered inside the electric fields of the atomic nuclei. The energy loss in the case of bremsstrahlung is directly proportional to the energy of the particle and can be calculated according to the following equation:

$$-\left(\frac{dE}{dx}\right)_{\text{bremsstrahlung}} = 4\alpha N_A \frac{Z^2}{A} r_e^2 E \ln \left( \frac{183}{Z^{1/3}} \right) \quad (3.11)$$

### 3. INTERACTION OF PARTICLES WITH MATTER

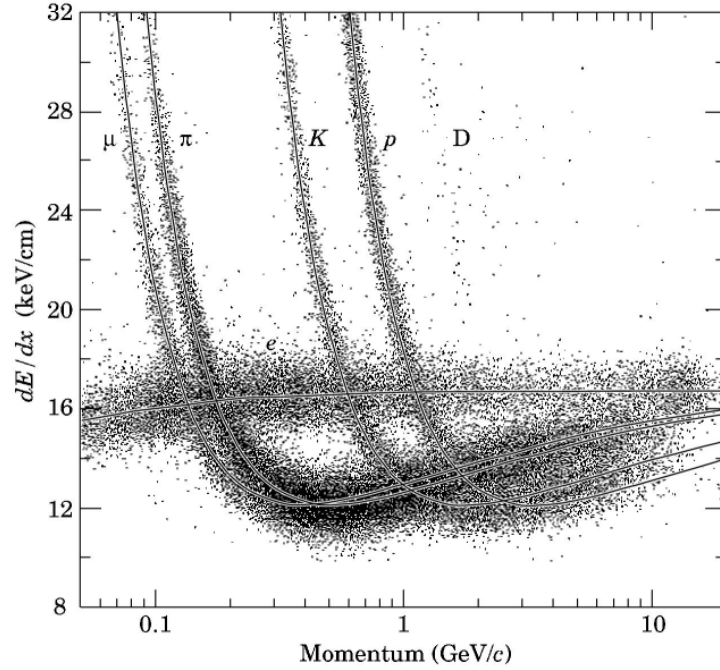


Figure 3.2.: Specific energy loss  $dE/dx$  of heavy particles inside a TPC with a gas mixture of ArCO<sub>2</sub> 80:20 [Yao06]

#### 3.2.3 Number of Created Electron-Ion Pairs

On the way through the gas in a gaseous detector the photon or charged particle is mainly losing energy due to the creation of electron-ion pairs. The electrons, which are created directly by the particle, are counted to the part of primary ionisation. If a photon is creating an electron due to the photo effect, the primary ionisation consists only of one single electron. Normally the energy of these created electrons is high enough to ionise more atoms, which is called secondary ionisation.

This process is taking place until the energy of the primary particle is divided and transferred completely into the energy of the secondary ionisation or until the particle leaves the gas volume. Therefore the number of electron-ion pairs depends on the energy of the particle, the length of the track and also on the average energy, which is necessary, to create an electron-ion pair.

This energy, which is called interaction energy  $E_i$ , is for one atom in general higher than the ionisation energy of the same atom, because it also includes the interaction with electrons in other shells. According to  $E_i$  the number of

### 3.3. Motion of Charge Carriers in Gases

electron-ion pairs, which is created by an electron with an energy loss of  $\Delta E$ , can be calculated as

$$n_p = \frac{\Delta E}{E_i} \quad (3.12)$$

Only 15% to 50% of all electron-ion pairs are created during the primary ionisation [Gru99]. The rest of them are created due to the secondary ionisation.

### 3.3 MOTION OF CHARGE CARRIERS IN GASES

#### 3.3.1 Drift Velocity of Electrons

If there is a homogeneous electric field with the absolute value  $E$  inside the gas volume, the electrons drift into the direction against the electric field lines and the positive charged ions into the opposite direction. The electrons are accelerated by the electric field until their impact with a gas atom resp. molecule. Inside pure vacuum the speed of the non relativistic electrons would increase with the acceleration  $a = F/m = eE/m$ . But if the electrons are moving inside a gas volume, they scatter in different directions due to collisions with the gas particles. The theory of electron drifting is described e.g. in [Halo3].

In every scattering process the electrons also loose energy. Because of the energy gain of the electrons between every collision an average velocity is reached. This velocity depends on the charge carrier mobility  $\mu^-$ , the electric field  $E$  and the pressure  $p$ , which is normalised with the standard pressure  $p_0$ . A detailed look leads to the equation

$$v_{\text{drift}}^- = \mu^-(E)E \frac{p_0}{p} \quad (3.13)$$

where  $\mu^-$  is different for every gas. Generally the drift velocity is in the range of  $\text{cm}/\mu\text{s}$ . The charge mobility  $\mu^-$  depends on the cross section  $\sigma$  for the collision of the electrons with the gas atoms and therefore on the mean free path length  $\lambda \sim 1/\sigma$ , which is directly correlated to the cross section.

In the case of electrons the Ramsauer effect plays an important role, which describes the behaviour of the electrons for energies at which the wavelength is approximately the same as the mean free path. At this energy, which is around 0.3 eV, the cross section is decreased, which leads to fact, that the drift velocity reaches a local maximum. This behaviour is shown in Figure 3.3 for different gases. The drift velocity of the particle and its maximum depend on its energy and the used gas [Gru99]. Usually a TPC is being operated at the maximum drift velocity, because here the first derivative is zero and the drift velocity does not change for small variations of the electric field [Kilo6].

### 3. INTERACTION OF PARTICLES WITH MATTER

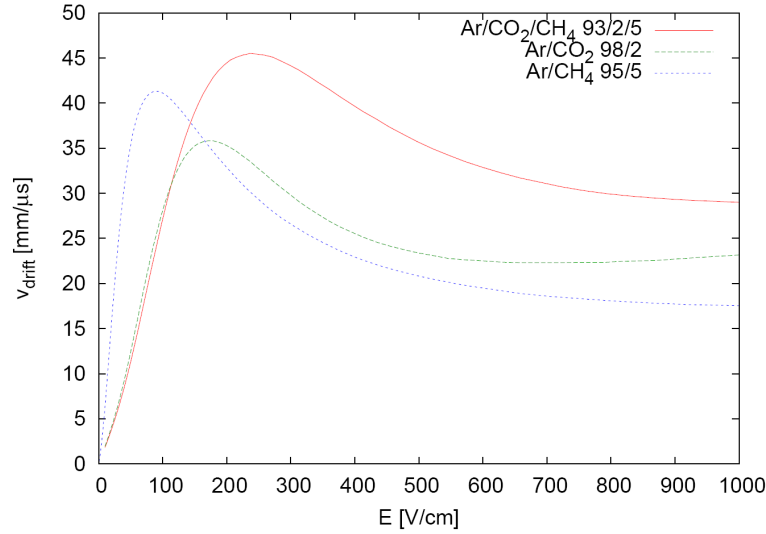


Figure 3.3.: The drift velocity of electrons as a function of the electron energy in different gas mixtures [Bia11]. One can see a clear maximum for each gas mixture.

#### 3.3.2 Drift of Ions

The behaviour of ions differs completely from the one of electrons, because their masses are up to a factor  $10^4$  higher than that of electrons. The charge mobility  $\mu^+$  of ions is almost constant for every value of the applied electric field, while for electrons the mobility is in general a function of their energy and therefore of the electric field. This leads to the fact, that the drift velocity of ions increases nearly linear to  $E$ :

$$v_{\text{drift}}^+ = \mu^+ E \quad (3.14)$$

Table 3.1 shows the measured mobility of noble gas ions in their parent gases [Blu93]. An ion can transfer the ionisation energy to another molecule by exchanging electrons with neutral atoms. This changes the mobility of ions. In a given gas mixture the mobility only depends on the gas mixture, not on the electric field.

### 3.4 DIFFUSION

The drifting electrons collide with gas molecules and scatter isotropically, because they are light compared to their impact partners. Thus after a few collisions, the momenta of the electrons have components in all directions

Gas	Ion	Mobility [cm <sup>2</sup> V <sup>-1</sup> s <sup>-1</sup> ]
He	He <sup>+</sup>	10.40 ± 0.10
Ne	Ne <sup>+</sup>	4.14 ± 0.2
Ar	Ar <sup>+</sup>	1.535 ± 0.007
Kr	Kr <sup>+</sup>	0.96 ± 0.09
Xe	Xe <sup>+</sup>	0.57 ± 0.05

Table 3.1.: Measured ion mobility of noble gas ions in their parent gas.

and lead to the concept of diffusion of an electron cloud [Blu94]. The density distribution of the electrons  $\rho_{el}$  satisfies the continuity equation for a conserved electron current  $\vec{\Gamma}$

$$\vec{\Gamma} = \rho_{el} \vec{v}_{drift} - D \nabla \rho_{el} = \text{const.} \quad (3.15)$$

The Gaussian density distribution with a time dependent width provides the following solution for equation (3.15)

$$\rho_{el} = \left( \frac{1}{\sqrt{4\pi Dt}} \right)^3 \exp \left( \frac{-r^2}{4Dt} \right) \quad (3.16)$$

where  $D$  is the gas specific diffusion coefficient of the gas. The coefficient of diffusion can be determined from the kinetic energy of the gas theory. It depends on the average thermal speed for gas molecules and the mean free path. If one assumes the charge cloud starts at the origin and drifts along the  $z$ -direction with  $r^2 = x^2 + y^2 + (z - v_{drift}t)^2$  as the squared distance to the center of the charge cloud, the width of this distribution in any direction is

$$\sigma = \sqrt{2Dt} \quad (3.17)$$

Together with the particle mobility  $\mu$  the diffusion coefficient can be calculated as follows:

$$D = \frac{kT}{e} \mu \quad (3.18)$$

In this case the thermal energy of the gas is calculated according to  $E = 3/2kT$  with the Boltzman constant  $k$  and the gas temperature  $T$ .

### 3. INTERACTION OF PARTICLES WITH MATTER

#### 3.4.1 Diffusion in Electric Fields

Inside an electric field the electrons and ions are forced to travel in one direction. For the described particle the distance  $r$  can be expressed as a function of the drift velocity and time:

$$r = \sqrt{x^2 + y^2 + (z - v_{\text{drift}}t)^2} \quad (3.19)$$

The average width of the charge cloud  $\sigma_x$  in one direction can also be rewritten to

$$\sigma_x = \sqrt{2Dt} = \sqrt{\frac{2DL}{\mu E}} \quad (3.20)$$

if  $L$  is the drift length and  $E$  the absolute value of the electric field.

#### *Longitudinal and Transversal Diffusion*

Due to quantum mechanical effects the diffusion is not totally isotropic in reality. One has to distinguish between transversal and longitudinal diffusion, which are assumed to be independent from each other. The longitudinal diffusion is caused by the fact, that the electrons in the center of a cluster have a higher energy and therefore move faster through the drift field.

The transversal diffusion works as described above and is therefore nearly isotropic. If  $D_l$  defines the longitudinal diffusion coefficient and  $D_t$  the transversal diffusion coefficient, then the variance  $\sigma$  of both diffusions can be written analogue to equation (3.20) as follows:

$$\sigma_l(z) = \sqrt{\frac{2D_l z}{\mu E}} = D_L \sqrt{z} \quad (3.21)$$

$$\sigma_t(z) = \sqrt{\frac{2D_t z}{\mu E}} = D_T \sqrt{z} \quad (3.22)$$

Here  $D_L$  and  $D_T$  are the variable names, which are identical to the ones used in most of the literature.

#### 3.4.2 Diffusion in Magnetic Fields

The application of a magnetic field parallel to the direction of the electric field influences the drift velocity and the diffusion of a charged particle inside the gas volume. The impact of these effects is described by the dimensionless



parameter  $\omega\tau$ , where  $\omega$  is the cyclotron frequency and  $\tau$  is the mean time between two collision.  $\omega$  can be calculated according to the following formula

$$\omega = \frac{eB}{m} \quad (3.23)$$

with the absolute value  $B$  of the magnetic field. Assuming that  $\tau$  is independent of  $E$ , the drift in the presence of electric and magnetic fields can be described according to the Langevin equation:

$$m \frac{d\vec{v}_{\text{drift}}}{dt} = e\vec{E} + [\vec{v}_{\text{drift}} \times \vec{B}] - \frac{m}{\tau} \vec{v}_{\text{drift}} \quad (3.24)$$

$m/\tau$  is related to a fractional force proportional to the drift velocity,  $e$  and  $m$  are charge and mass of the drifting particle. Solving the equation for steady state and for times longer than  $\tau$  gives the following result:

$$\vec{v}_{\text{drift}} = \frac{e}{m} \tau |\vec{E}| \frac{1}{1 + \omega^2 \tau^2} \left[ \hat{E} + \omega\tau (\hat{E} \times \hat{B}) + \omega^2 \tau^2 (\hat{E} \cdot \hat{B}) \hat{B} \right] \quad (3.25)$$

In this equation  $\hat{E}$  and  $\hat{B}$  represent the normalised and dimensionless vectors in the direction of the electric and magnetic field. The product  $\omega\tau$  is very small for ions ( $\mathcal{O}(10^{-4})$ ), but quite large for electrons ( $\mathcal{O}(1)$ ). Equation (3.25) gives the motion of electrons due to an electric field and the curvature of the trajectory caused by the magnetic field.

If  $\sigma_0$  describes the diffusion  $\sigma_x$  for the absence of any magnetic field, i.e.  $B = 0$  T, the suppressed diffusion inside the magnetic field  $B$  can be computed by the following formula:

$$\sigma(B) = \frac{\sigma_0}{\sqrt{1 + \omega^2 \tau^2}} \quad (3.26)$$

One can see from this equation, that the higher the value of the magnetic field  $B$  the better the diffusion can be suppressed. In equation (3.25) the last term dominates for electrons, which leads to the fact, that electrons drift along the magnetic field lines instead of the electric field ones, if  $E$  and  $B$  are not parallel.

If there is a small angle  $\varphi$  between the vectors  $\hat{E}$  and  $\hat{B}$  the charged particle does not drift any longer into the direction of the electric field. Under this condition it has to be calculated with the following formula:

$$v_{\text{drift}} = \frac{qE}{m} \tau \sqrt{\frac{1 + \omega^2 \tau^2 \cos^2 \varphi}{1 + \omega^2 \tau^2}} \quad (3.27)$$

### 3. INTERACTION OF PARTICLES WITH MATTER

#### 3.5 PROPERTIES OF DIFFERENT GAS MIXTURES

As mentioned above the filling of a TPC consists mainly of a noble gas. In addition to this another type of gas is important, which is called quencher. The quencher can consist of gas molecules with organic atom combinations like  $\text{CH}_4$  or  $\text{CO}_2$  and is added to the gas mixture up to a percentage of normally between 1% and 30%. A quencher is used to prevent the noble gas atoms from being excited, which can happen due to scattering of electrons from the primary or secondary ionisation. This excitation should be avoided, because the noble gas atoms can emit photons during the process of de-excitation, which can ionise other atoms. The molecules of the quencher gas can save the energy of the electrons in different rotational or swinging states. A good description with tables and figures of different gas mixtures can be found in [Gru99], which is dealing with gas studies for the linear collider TESLA.

##### 3.5.1 *Conditions for the Nobel Gas*

There are some conditions, which have to be fulfilled by the gas mixture in order to get good results with a TPC. From these parameters one can try to find the best mixture, which is suitable to test the setup. Some mixtures have the advantage of less diffusion, while others have the effect of a high drift velocity. By combining different gases it can be possible to get the maximum output from the TPC. While most of these parameters shall be explained now on the example of Argon, a list of different gases can be found in Table 3.2

An important factor is the number  $N_t$  of created electron-ion pairs for minimum ionising particles. The value of  $N_t$  should be relatively large in order to show a good energy resolution, which is approx. proportional to  $\sqrt{1/N_t}$ . For Argon this value is around 100/cm. Another important parameter is the radiation length  $X_0$ , which is for Argon around 120 m. If the momentum of a particle is quite small, the momentum resolution  $p_{rs}$  depends highly on multiple scattering. A small  $X_0$  like for Argon (compared to other gases like Helium or Neon) would lead to a higher contribution of multiple scattering and therefore to a larger momentum resolution.

It is also important to know the drift velocity of the used noble gas, which is high for mixtures with Argon or Helium. One of the big disadvantages of using Helium is, that most of the parameters of the gas mixtures are highly influenced by very small changes of the percentage of the noble gas. Compared to the noble gas Neon the transversal diffusion is much lower for Argon based mixtures, while for Neon the longitudinal diffusion has a smaller value. In the planning phase of the project, one has to decide, whether a small transversal or

### 3.5. Properties of Different Gas Mixtures

Gas	$X_0$ [m]	$N_t$ [1/cm]	$\sigma_n$ [barn]
He	5299	8	1.34
Ar	110	94	0.683
Ne	345	43	2.628
CF <sub>4</sub>	92.4	100	—
DME	222	160	—
CO <sub>2</sub>	183	91	14.015
CH <sub>4</sub>	646	53	333.631
C <sub>2</sub> H <sub>6</sub>	340	111	503.222
iC <sub>4</sub> H <sub>10</sub>	169	195	842.404

Table 3.2.: Gas properties for different gases calculated with Magboltz, where  $X_0$  is the radiation length,  $N_t$  is the total number of electrons released per cm for minimum ionising particles and  $\sigma_n$  is the total neutron bound scattering cross section [Gru99]

a small longitudinal diffusion will lead to better results. In the case of the TPC at the University of Siegen, the decision was made to use Argon and methane resp. carbon dioxide as a quencher.

#### 3.5.2 Conditions for the Quencher

The quencher must also fulfil some conditions in order not to influence the measurement. One of these conditions is, that it should have as less H-molecules as possible, if it is necessary to have a high cross section for neutron scattering. In the case of diffusion there are some quencher gases like CO<sub>2</sub>, which have a good suppression of the longitudinal diffusion and some gases, which are useful, if one wants to suppress the transversal diffusion. For this purpose normally CH<sub>4</sub> is used.

A disadvantage of CH<sub>4</sub> is, that this is one of the gases, which is still under high investigation. Some effects, like the penning effect<sup>1</sup>, are not fully understood until now, which makes simulations quite difficult and measurements sometimes not reproducible.

<sup>1</sup> If the excitation energy of one gas inside a mixture is higher than the ionisation energy for the second one, the atoms of the first gas can transfer their energy to the atoms of the second gas and ionise them.



## TIME PROJECTION CHAMBER

---

### 4.1 WORKING PRINCIPLE OF A TIME PROJECTION CHAMBER

The Time Projection Chamber (TPC) is a well known and approved concept of a gaseous detector in high energy physics. A TPC [Nyg74] consists of a volume, which is filled with a noble gas (e.g. Helium or Argon). Nobel gas is used because of its physical and chemical properties. Atoms of a noble gas are not doing any kind of chemical reaction with other atoms or molecules (see section 3.5.1). If a photon or charged particle is moving through this gas volume, the gas atoms are going to be ionised. According to the theory described in chapter 3, a cloud of electron-ion pairs is created, where the number of these pairs per unit length depends mainly on the energy of the incident particle and the ionisation potential of the gas. If there is an electric field between two electrodes of the gas volume, the electrons drift to the positively charged anode and ions to the negatively charged cathode.

Because of the limited size of the electrodes, the field lines are in general not absolutely parallel. The field lines bend at the edges of the electrodes and lead to a non-homogeneous electric field, which has to be compensated. For this purpose electrical field strips are placed around the gas volume in equal distances. These strips are placed in a series connection via resistors, which create a constant electric field between each two strips. A sketch of a TPC can be seen in Figure 4.1, showing a charged particle (e.g. a muon or electron) creating a track of electron-ion pairs, which are drifting inside the applied electric field. The electrons, reaching to the anode plate, create a small electric signal, which can be amplified and read out by a two dimensional readout structure. By dividing the anode plate in several parts (so called pads), which are electrically insulated from each other, it is possible to get information about the position of the electron. If such division is small enough, it can be possible to reconstruct the whole track of the charged particle by collecting the charge and arrival time information.

For the measurement of particle momenta and the charge of the traversing particle a magnetic field is used. Typically its orientation is parallel or anti-parallel to the electric field. In a homogeneous magnetic field a particle will move in the form of a helix instead of a straight line. The projection of this helix into a two dimensional space is a part of a circle with a specific bending

#### 4. TIME PROJECTION CHAMBER

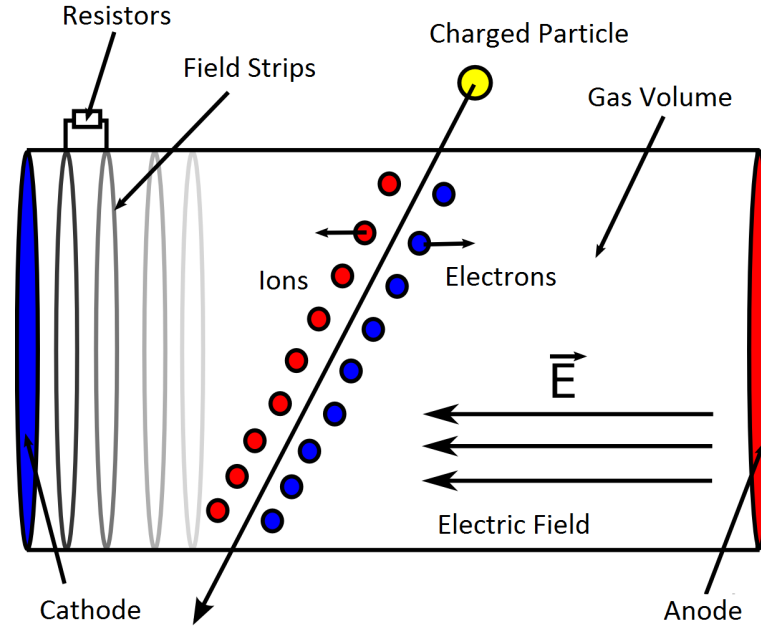


Figure 4.1.: Sketch of a TPC, showing ionisation of the gas due to a charged particle [Sch11]

radius  $r$ . By measuring  $r$ , the momentum of the particle can be determined. However this only works for a charged particle, where the magnetic force is always orthogonal to the momentum of the particle. In this case the condition  $F_m = F_z$  holds, where  $F_m$  is magnetic force and  $F_z$  is the centripetal force. Therefore it follows:

$$evB = \frac{mv^2}{r} \quad (4.1)$$

From this the momentum of a particle can be calculated according to the following formula:

$$p = mv = eBr \quad (4.2)$$

Besides tracking capabilities, a TPC also offers the possibility of particle identification due to the specific energy loss in a gas volume of a TPC. Such measurements were performed with the ALEPH TPC [Bow95] and the ALICE TPC [Deloo]. Due to the high homogeneity of the gas volume, the energy loss per unit length  $dE/dx$  (see section 3.2.2) in the gas can be measured precisely. The energy loss measured along the particle trajectory and the momenta determined via the magnetic field allows an efficient particle identification. Since the whole volume of a TPC is filled with gas, the material budget of a TPC is low. This makes it a very important detector type for tracking systems,

as the energy loss of the particles have to be kept as low as possible in the tracking detectors.

#### 4.2 PRIMARY IONISATION IN THE TPC

Ejection of one or more electrons from an atom by collision with a fast particle is known as primary ionisation. The ionisation energy of an atom is typically in the range of eV and depends on its properties.

If the energy, which is transferred to the released electron, is significantly larger than the ionisation energy  $W$  of the gas, secondary electrons are set free due to inelastic collisions of the primary electrons with gas molecules. These secondary electrons form clusters, that are spatially correlated to the primary ones. The production of primary electrons  $n_P$  in a specific gas is roughly proportional to the atomic number of the gas molecules. The total number of electrons  $n_T$  per unit length is given by the ratio of the energy deposit  $\Delta E$  per unit length and the ionisation energy  $W$  [Loh92]:

$$n_T = \frac{\Delta E}{W} \quad (4.3)$$

Taking the example of Argon together with secondary electrons, in total 94 electrons per centimeter are emitted for standard pressure and temperature [Sha98]. A description of ionisation parameters of different gases can be seen

Gas	$I_0$ [eV]	$W$ [eV]	$\frac{dE}{dx}$ [ $\frac{keV}{cm}$ ]	$n_P$ [ $\frac{1}{cm}$ ]	$n_T$ [ $\frac{1}{cm}$ ]
He	24.5	41	0.32	4.2	8
Ar	15.7	26	2.44	23	94
Xe	12.1	22	6.76	44	307
CO <sub>2</sub>	13.7	33	3.01	35.5	91
CH <sub>4</sub>	15.2	28	1.48	25	53
CF <sub>4</sub>	15.9	54	7	51	100
DME	10.0	2.9	3.9	55	160

Table 4.1.: The ionisation gas parameters for frequently used chamber gases. There  $I_0$  is the effective ionisation potential,  $W$  is the average energy needed to create an electron-ion pair,  $dE/dx$  is the specific energy loss,  $n_P$  is the number of primary produced electrons and  $n_T$  is the total number of created electron-ion pairs per unit length at standard conditions [Sha98]

## 4. TIME PROJECTION CHAMBER

in Table 4.1. Along a track most of the clusters consist of up to ten electrons, but occasionally the initial particle transfers a very large amount of energy to one single electron [Lea10]. These electrons are able to travel in arbitrary direction up to several centimeters, ionising the gas molecules on their way and are known as delta electrons ( $\delta$ -electrons).

### 4.3 METHODS OF GAS AMPLIFICATION

Normally the signal, which reaches the anode plate, is too small to be measured directly. In order to increase the signal, there are two different possibilities: electronical and physical amplification. By applying electronical amplification the noise is also amplified, which makes this method less effective for a general purpose. Physical amplification leads to a higher output signal without increasing the noise. For this method a lot of different techniques have been established during the last decades. The most effective ones for gaseous detectors will be listed and explained inside the following section:

- Multi -Wires
- MicroMegas
- Gas Electron Multipliers (GEMs)

For the TPC project at University of Siegen GEMs were used because of their easy usage and good results.

#### 4.3.1 *Multi-Wires*

One way to reconstruct the track of a particle is to create a plane of parallel wires near the anode plate as described in [Sli77]. The wires are set to a high positive potential between 1 kV and 2 kV, which creates a strong electric field around the wires in Figure 4.2. Each wire has its own amplifier with transistorised electronics, to establish a particle detector with position sensing.

In general the electric field of a charged conductive wire can be written according to [Grfo7] as follows:

$$\vec{E} = C(\lambda) \cdot \frac{\vec{e}_r}{r} \quad (4.4)$$

where  $C(\lambda)$  is a constant, which is proportional to the linear charge density  $\lambda$  with  $[\lambda] = \text{coulomb/meter}$ .  $\vec{e}_r$  is the unit vector in radial direction to the wire. If a drift electron reaches this wire plane it is accelerated inside the electric



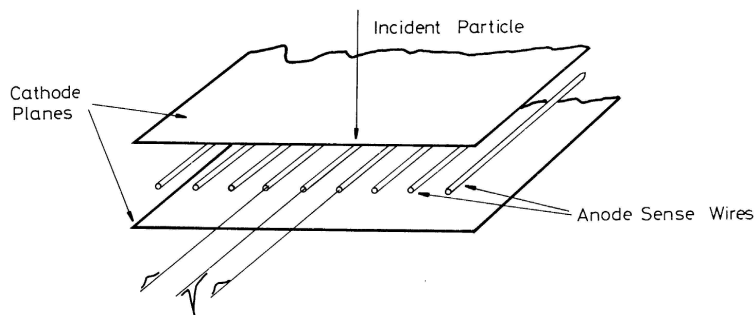


Figure 4.2.: Schematic of a multi-wire chamber [Lah07]

field until its energy is high enough to ionise further gas atoms. Since this process happens several times after each other, an avalanche of electrons is created.

The total number of the created electrons can be up to a factor  $10^4$  times larger than the amount of the initial electrons. While the electrons are collected at a wire, the ions move forward to the cathode plates, where they create a positive signal in the read out system. In order to isolate the anode from the high electric field of the wire plane and to achieve a homogeneous electric field usually a plane with cathode wires is placed between the positive wire plane and the anode plate.

The concept of multi-wire proportional counters cannot be used for the ILD TPC, because the  $\vec{E} \times \vec{B}$  effects are large and the required resolution can not be achieved. Another disadvantage is the distance between the wires, which cannot be small enough due to mechanical reasons and the material budget for wires is high.

#### 4.3.2 *MicroMegas*

The Micro-MESH Gaseous Structure (MicroMegas) are a further development of the multi-wire principle. A complete description can be found in [Gio96]. It mainly consists of a metallic mesh spanned with pillars over a readout plane, which can measure the ionisation signal. The distance between the metallic mesh and the strips usually varies between  $25 \mu\text{m}$  and  $150 \mu\text{m}$ . The mesh for the gas amplification consists of a bunch of wires, which are spanned in a way, that they create an even plane. In opposite to multi-wires the amplification takes place inside the amplification gap between the micromesh and the readout plane.

If an electron from the primary or secondary ionisation reaches the mesh, it is accelerated inside a high electric field of the amplification gaps and gains

#### 4. TIME PROJECTION CHAMBER

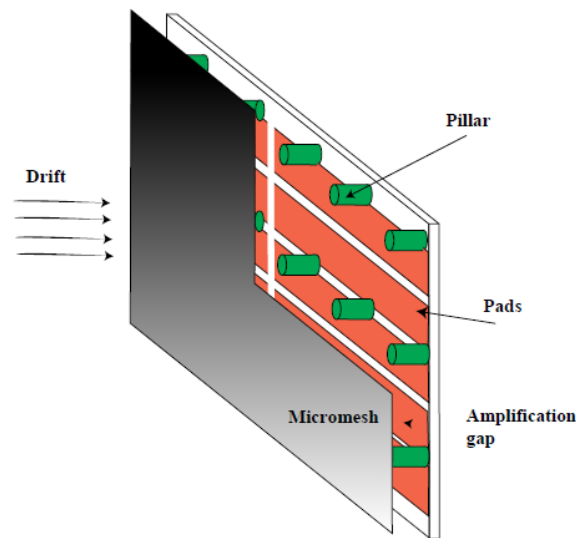


Figure 4.3.: Schematic layout of a MicroMegas [TES01]

a high kinetic energy in the same way as for the multi-wires. Due to this an avalanche of electrons is created from each electron. When the avalanche reaches the readout strips, it creates an electric signal, which can be amplified and analysed by readout electronics. Another advantage of the MicroMegas is, that most of the ions produced during the gas amplification cannot move back into the drift volume above the micromesh, because they are captured on its top, if the ratio between the drift field and field inside the amplification gap is tuned properly.

##### 4.3.3 Gas Electron Multipliers

In 1996 F. Sauli developed the first GEM as an alternative for multi-wires. A GEM consists of a thin plastic foil with a layer of copper on the upper and lower side. Inside the GEM there is a huge amount of double conic holes, which can let the electrons pass through the GEM as one can see in Figure 4.4. Figure 4.5 shows the typical dimensions of a standard CERN GEM.

If one applies a potential difference of several 100 volts between both GEM sides, the electric field inside each hole can reach a value up to nearly 100 kV/mm. In a gas volume, this high electric field creates avalanches of electrons from every single initial electron, which then reach the anode plate and can be registered. The electric field lines between the two GEM sides can be seen in Figure 4.6. This figure shows the output of a simulation, which has been produced with Ansys [Ans14] and Garfield [Gar14].

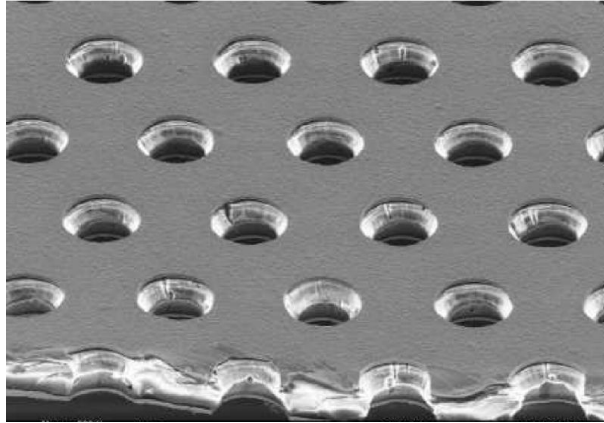


Figure 4.4.: Picture of GEM under the microscope [FLC11]

The advantage of GEMs is the easiness of installation and the possibility to increase the amplification by creating stacks of GEMs. In this case two or more GEMs are placed behind each other in series. The total amplification is then the product of the amplification of each GEM (see section 4.3.4).

One disadvantage of GEMs is the possibility of spark production between the two copper layers of one GEM or between the copper layers of two different GEMs, if the applied voltage is too high for the chosen gas mixture. In worst case these sparks can destroy the GEMs or the readout system (see section 4.3.5). The detailed physical description of the GEMs can be found in [Loto6]. The electric field inside a GEM hole is calculated with the formula

$$E_{\text{hole}} = a\Delta U_{\text{GEM}} + b(E_{\text{up}} + E_{\text{down}}) \quad (4.5)$$

where  $a$  and  $b$  are GEM geometry constants and  $E_{\text{top}}$  and  $E_{\text{bottom}}$  are the fields above and below a GEM, respectively. The gain depends on the geometrical properties  $a$  resp.  $b$  and the electric field between its two sides. In this case  $\Delta U_{\text{GEM}}$  is the voltage difference between the GEM upper and lower side.

When ionising particles traverse the drift region, electron-ion pairs are created. In the presence of the electric field the electrons drift towards the anode. In a TPC at the anode side GEMs are used for the amplification by increasing the number of electrons, before they reach to the read out system. Near the GEM surface (the surface which is near to drift region), most of the field lines collect into the GEM holes and emerge on the other side between the lower surface of the GEM and the readout plane, while the others may be terminated on the GEM surface (see Figure 4.6). The focusing effect of the field lines are responsible to collect the electrons into the holes. Inside the holes they gain energy due to the high electric field and create further electron-ion

#### 4. TIME PROJECTION CHAMBER

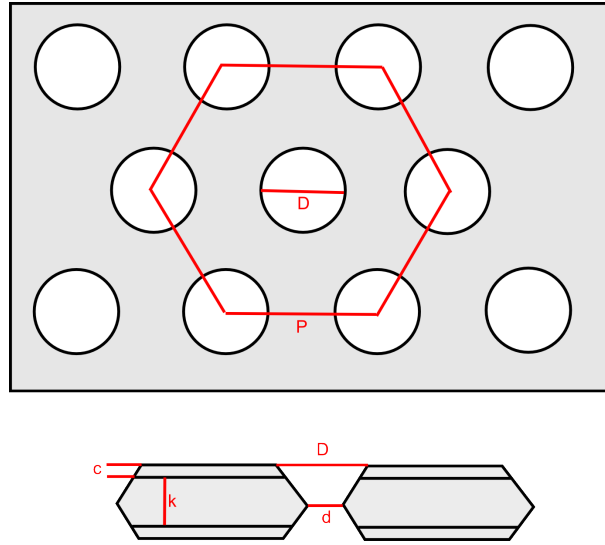


Figure 4.5.: Sketch of a standard CERN GEM with all necessary parameters where  $D$  is the outer diameter of the hole  $70\mu\text{m}$ ,  $d$  is the inner diameter of the hole  $50\mu\text{m}$ ,  $c$  is the thickness of the copper layer  $5\mu\text{m}$ ,  $k$  is the thickness of kapton  $50\mu\text{m}$  and  $P$  is distance between the center of the two holes  $140\mu\text{m}$ .

pairs by subsequent collision with the gas molecules (which are present in the hole). The created ions move back into the drift area and reach the cathode after some time, where they are neutralised.

Charge transfer coefficients quantitatively describe the inefficiencies for the transport of positive ions and electrons through the GEM foil. The collection and extraction inefficiencies are valid for both electrons and positive ions, while in case of gas amplification (gain) only electrons are active.

#### Collection Efficiency

The collection efficiency defines the ratio of the arriving charge carriers and those, which are transferred into the GEM holes:

$$C^{\pm} = \frac{N_{e^-, I^+} \text{ collected inside GEM hole}}{N_{e^-, I^+} \text{ in front of the GEM hole}} \quad (4.6)$$

where  $N_{e^-}$  is the number of electrons and  $N_{I^+}$  the number of ions.  $C^{\pm}$  depends on the ratio  $E_{\text{up}}/E_{\text{down}}$  of the electric field  $E_{\text{up}}$  on the upper side and the one  $E_{\text{down}}$  on the lower side of the GEM according to:

$$C^- = \begin{cases} 1 & \text{if } \frac{E_{\text{up}}}{E_{\text{down}}} \leq r^{\frac{1}{s}} \\ r \left( \frac{E_{\text{up}}}{E_{\text{down}}} \right)^{-s} & \text{if } \frac{E_{\text{up}}}{E_{\text{down}}} > r^{\frac{1}{s}} \end{cases} \quad (4.7)$$

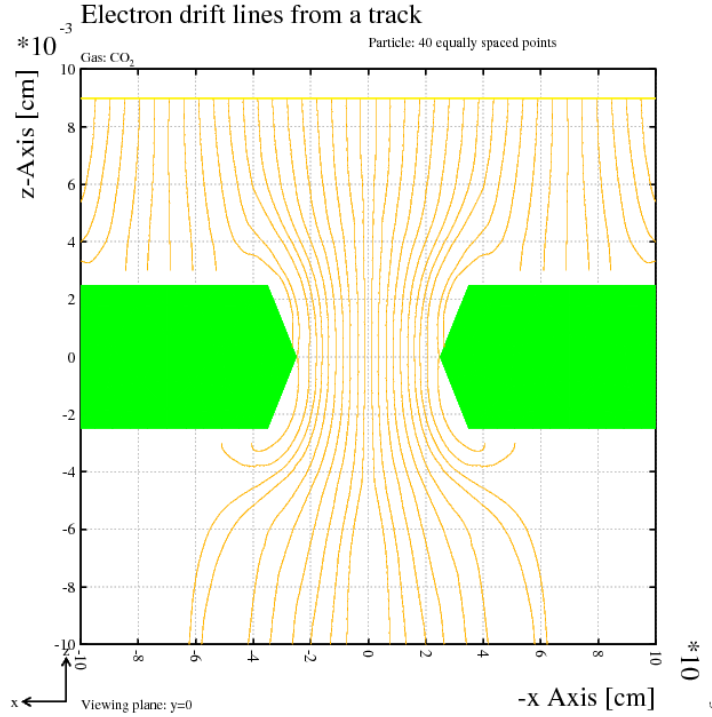


Figure 4.6.: Electric field lines between two GEM sides. The simulation has been done with the help of Garfield and Ansys. The GEM is located inside an external electric field between a cathode (up) and an anode (down).

where  $r$  and  $s$  free parameters depending on the geometry of the GEM.

#### Extraction Efficiency

The extraction efficiency describes the fraction of electrons in the GEM hole which are extracted and drift towards the anode:

$$X^{\pm} = \frac{N_{e^{-},I^{+}} \text{ extracted out of GEM hole}}{N_{e^{-},I^{+}} \text{ created inside GEM hole}} \quad (4.8)$$

These coefficients can be also calculated with the help of some parameters. For electrons they have the form:

$$X^{-} = \begin{cases} \frac{1}{T_{\text{opt}}} \left( \frac{E_{\text{down}}}{E_{\text{up}}} - y \right) + g & \text{if } \frac{E_{\text{up}}}{E_{\text{down}}} \leq r^{\frac{1}{s}} \\ \frac{1}{T_{\text{opt}}} \left( \frac{E_{\text{down}}}{E_{\text{up}}} - y \right)^{1-s} + g & \text{if } \frac{E_{\text{up}}}{E_{\text{down}}} > r^{\frac{1}{s}} \end{cases} \quad (4.9)$$

The constants  $r$ ,  $s$ ,  $g$  and  $y$  are free parameters. They can be found in literature or determined with the help of experiments. It is important to know, that  $r$  and

#### 4. TIME PROJECTION CHAMBER

$s$  are generally not the same for  $C^-$  and  $X^-$  [Sobo2][Loto6]. The parameter  $T_{\text{opt}}$  describes the optical transparency of the GEM according to the following formula:

$$T_{\text{opt}} = \frac{\text{Total area of all holes}}{\text{Total Area of the GEM foil}} = \frac{\pi}{2\sqrt{3}} \left( \frac{d}{P} \right)^2 \quad (4.10)$$

##### *Gain of GEMs*

The gain describes the number of electrons created in a GEM hole:

$$G = \frac{N_{e^-} \text{ collected inside GEM hole}}{N_{e^-} \text{ created inside GEM hole}} \quad (4.11)$$

The gain increases exponentially with the potential difference across the GEM,  $\Delta U_{\text{GEM}}$ . Hence it can be calculated:

$$G_{\text{GEM}} = \alpha e^{\beta \Delta U_{\text{GEM}}} \quad (4.12)$$

where  $\alpha$  and  $\beta$  are free parameters.

##### *Effective Gain of GEMs*

In general the measured gain is always less than the one calculated with equation (4.12). Due to this reason another equation for the effective gain  $G_{\text{eff}}$  has been introduced, which is written as follows:

$$G_{\text{eff}} = C^- X^- G \quad (4.13)$$

The effective gain  $G_{\text{eff}}$  of a GEM foil is equal to the number of electrons after passing the GEM divided by their original number in front of the GEM. It is defined by the product of the collection, gain and extraction.

#### 4.3.4 GEM Stack

Using GEM foils in stacks instead of single ones has advantages in many ways. Usually the effective gain of a single GEM is in the order of  $10^2$  to  $10^4$ . Combining two or more GEMs in a GEM stack results in a higher gain. In a GEM stack the effective gain is calculated by the product of the individual effective gains of the single GEM (see Figure 4.7). Another characteristic of the GEM stack is the intrinsic ion gating which can be achieved by setting an appropriate voltage to the different GEMs.

In such a stack many ions are neutralised on the lower surface of the upper GEM. This prevents them from reaching back into the drift volume. In a

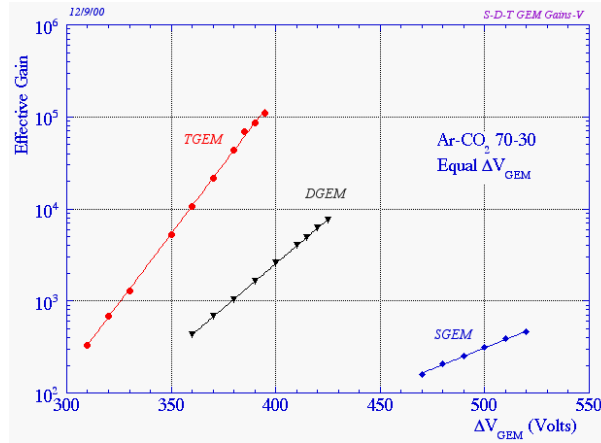


Figure 4.7.: The gas gain of single (SGEM), double (DGEM) and triple (TGEM) GEM stacks as a function of the voltage difference for a mixture of Ar and CO<sub>2</sub> with a percentage of 70:30, respectively [Sau03].

stack all GEMs work almost independently from each other. Compared to MicroMegas ion drift times are shorter in GEMs. In this thesis a GEM stack of three GEMs will be used. The GEM nearest to the readout plan will be referred as GEM<sub>1</sub>, while GEM<sub>2</sub> is the middle one and the GEM near to the drift region and therefore topmost is referred as GEM<sub>3</sub>, as it will be explained later in chapter 5.

#### 4.3.5 Discharge Possibility

The primary and secondary electrons drift into the direction of the GEM, where they create electron avalanches. This effect starts at electric fields around 10 kV/cm. The number of developed electrons  $N$  can be calculated as:

$$N(x) = N_0 \cdot e^{\alpha x} \quad (4.14)$$

where  $\alpha$  is the Townsend coefficient and  $x$  is the distance. When the exponent  $\alpha x$  is  $\approx 20$  or the gain becomes larger than  $10^8$  then the discharges inside the gas are initiated. This limit is known as Raether Criterion [Le094]. At this limit a so called streamer breakdown takes place, which is characterised by a narrow plasma formed by an electron avalanche [Lea10]. Due its small resistance it causes a flow of current. The discharge effect depends on many different factors including temperature, humidity and the flow of gas. The discharge probability for a given effective gain depends on the amount of charge carriers, their spatial resolution and density.

#### 4. TIME PROJECTION CHAMBER

In case of a gaseous detector using GEMs for amplification, discharges occur usually between both copper surfaces of a single foil. The presence of these discharges can damage the foil and also have a possibility to propagate through the structure and hit the anode plate. A direct discharge hit on the readout can cause damages to the readout electronics, which should be avoided. The energy of the primary discharge is proportional to the energy stored in the GEM. Additionally the propagation probability of the discharge through the whole structure is influenced by the first discharge and the strength of the electric field between the GEM and the readout plane (induction field).

##### 4.3.6 Carbon Coated GEMs

The motivation for carbon coated GEMs is based on the ideas presented in [Beig8], which have been developed at the University of Siegen in 1998. Because of the encouraging results regarding the optimisation of a TPC, it seemed to be beneficial to continue research in this subject.

The main limitation of gas amplification with GEMs is the possibility of discharges between the GEM surfaces, which may lead to non-uniformity of the electric field (e.g. due to sharp edges or a changing resistance over the surface of the GEMs). Both effects can be reduced by coating the complete GEM surface with a thin layer of carbon, so that both both GEM sides are connected electrically with each other. At whole the resistance between the GEM surfaces is reduced by this method, which reduces also the effective gain at a given GEM voltage. A positive side effect is, that the charging up of the plastic between the copper layers can be reduced almost completely.

This leads to a higher gain stability in time and space. It is shown, that the gain is not changing over the surface of the whole GEM after coating with carbon. A low quality GEM with non constant hole sizes on the surface may show big variations and the energy resolution is quite poor due to undefined electric field strengths inside the holes. This effect can be also minimised by coating the GEMs, which finally leads to an increase of the energy resolution.

All advantages together have given the motivation to insert carbon coated GEMs into the test chamber in Siegen in order to check the results by reproducing the measurements. In case of good results it has been decided to use these GEMs inside the prototype TPC, in order to achieve higher gas gains and create better measurement results.



## 4.4 ION BACK DRIFT IN TPCS

The discharge probability is not the only factor for a GEM, which needs optimisation. Another important factor is the reduction of the ion back drift. Every ionisation of gas atoms inside the TPC produces electrons and ions. While the electrons move forward to reach the readout system, the ions drift back to the cathode. The disadvantage of the ion back drift is the distortion of the electric field inside the drift volume of the chamber. And even a small inhomogeneity of the electric field can lead to a worse resolution in the track reconstruction of the ionising particle.

Most of the ions are not produced during the primary and secondary ionisation, but inside the gas amplification system, where the electron avalanches are created. The drift velocity of ions is always very small compared to the one of electrons. This is the reason, why ions usually remain much longer inside the active volume of the TPC than the electrons and have a large influence on the electric field. The ion back drift  $I_{BD}$  is defined by the ratio of the number of electrons reaching the anode plate and the ions, which drift back to the cathode:

$$I_{BD} = \frac{N_{\text{Electrons reaching anode}}}{N_{\text{Ions reaching cathode}}}$$

One possibility to reduce the ion back drift is the usage of so called ion grids [Kilo6]. In principle, this grid consists of a plane of wires between the cathode and anode plate in front of the gas amplification. In the opened mode all wires are on the same potential as it would be on their position without wires. In this case the drift of the electrons is not disturbed.

In the closed mode every second wire is on a slightly higher potential and the others are on slightly lower potentials, i.e. the field lines start from every second wire with the higher potential and end on its two neighbours, which have a lower potential. The working principle is like this, that shortly before a collision of the accelerator beam takes place, the ion grid is set to the opened mode in order to let the primary and secondary electrons pass. After the measurement or if no trigger signal is detected, the grid is set again to the closed mode. The ion drift velocity is so slow, that it usually needs more than one closing until the ions reach the wires with the lower potential for being neutralised.

According to studies, which have been made with GEM based TPCs, it is also possible to reduce the ion back drift by using three GEMs with special field and voltage configurations [Loto6]. The optimum in suppressing the ion back drift can be reached, if the induction field and the second transfer field is set to high values, while the first transfer field should have smaller values. It is

#### 4. TIME PROJECTION CHAMBER

also important, that the voltage of the GEM closest to the readout should have the highest amplification, which is achievable. The voltages of the other two GEMs can be set according to the desired gain, since they have less influence on the ion back drift. With this method it is possible to reduce the ion back drift to  $I_{BD} \leq 1\%$

#### 4.5 POSSIBLE READOUT SYSTEMS FOR TPC

##### 4.5.1 *Readout with Pads*

As explained in the beginning of this chapter one can divide the anode plate in several areas, called pads, with different or equal sizes. A photo of a sample pad plane, which has been used for the prototype TPC, is shown in Figure 4.8. Each of these pads has to be connected to an amplifier with which the amount of charge can be converted into an electrical signal. This signal can be recorded using an ADC or MCA.

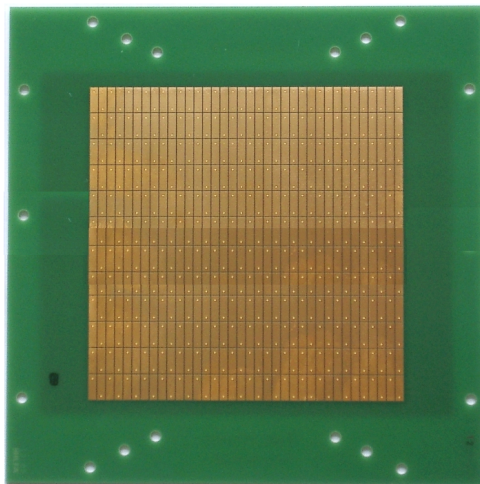


Figure 4.8.: Pad readout used for TPC at University of Siegen.

The advantage of this readout method is the easy handling due to the large scale of the pad plane. Pads are also very resistant against high voltage discharges and mechanical damages, which makes it easy to install or change them. A big disadvantage of the readout with pads is the fact, that the minimum size of each pad is limited. Usually it is in the order several  $\text{mm}^2$ . This decreases the spatial resolution and makes cluster counting impossible. The readout electronics like amplifiers and discriminators for a pad plane has to be installed externally, which enlarges the size of the whole system. These

advantages and disadvantages are in principle interchanged for a readout system with a pixel chip.

#### 4.5.2 Readout with Pixel chip

Another possibility for a readout system is the usage of a silicon chip as a detector, which is working in principle like a CCD chip of a camera. Each pixel can be seen as a very small pad in the range of a few  $\mu\text{m}$  height and width. With this method it is possible to create detectors with the size of a cent coin, which still has a resolution of for example  $100 \times 100$  pixels.

In general the analogue and digital electronics (such as amplifiers, discriminators and counting logic) for each pixel is a part of the chip by itself, which reduces the size of the electrical components. In order to read out the signals, which are produced by the pixels, external electronics and additional software is necessary. The chip can be easily connected to an interface of a PC to collect the data.

Compared to copper pads a pixel chip is quite expensive and more difficult to produce. A disadvantage is its sensitivity to electric discharges. A few sparks inside the TPC can destroy some pixel rows or even the whole chip completely. Further details will be presented in chapter 5.

## 4.6 ADVANTAGES OF A TPC

The TPC is mainly filled with gas, which leads to a low material budget. Because of this reason the energy of the ionising particle is only slightly changed while passing through the chamber and the track can be easily reconstructed. As compared to a solid state detector it provides a good  $dE/dx$  measurement.

Another advantage of a GEM based TPC with an applied magnetic field is a good spatial resolution  $\sigma_S$  of less than  $350 \mu\text{m}$  over a drift length of 2.5 m with a magnetic field of  $\approx 4 \text{ T}$  for the gas mixture TDR <sup>1</sup> as one can see in Figure 4.9. The created particles move on a helix inside the magnetic field. From this the momentum resolution can be derived, which leads to the following equation [Fer86]:

$$\frac{\sigma_{p_T}}{p_T} = \frac{\sigma_S}{L^2 B} \quad (4.15)$$

Here  $p_T$  is the transversal momentum and  $L$  the track length. From this formula one can see, that  $\sigma_{p_T}$  is decreasing for longer track lengths. It is also

<sup>1</sup> Ar:CH<sub>4</sub>:CO<sub>2</sub> 93:5:2 as used for the Tesla detector at DESY

#### 4. TIME PROJECTION CHAMBER

important to have a good spatial resolution, in order to achieve the wanted momentum resolution for the ILC.

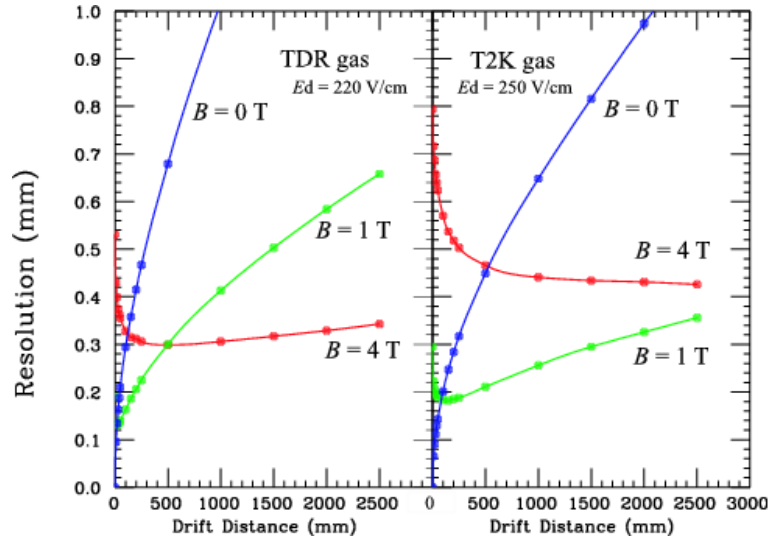


Figure 4.9.: Spatial resolution of a GEM based TPC inside a magnetic field for the gas mixtures TDR (Ar:CH<sub>4</sub>:CO<sub>2</sub> 93:5:2) (left) and T2K (Ar:CF<sub>4</sub>:iC<sub>4</sub>H<sub>10</sub> 95:3:2) (right) [Ack09]. The value  $E_d$  represents the applied drift field.

#### 4.7 TPC FOR THE INTERNATIONAL LARGE DETECTOR

In the Linear Collider community for the **ILD** a TPC is a choice for the central tracking detector [ILC13]. It has a cylindrical shape and is divided into two half chambers. To ensure a homogeneous electric field over the full length of the TPC the walls of the cylinder contain a field cage. In the center of the TPC the cathode will be placed while there will be two anodes, one at each ends of the TPC (see Figure 4.10). The readout modules will be assembled in concentric rings held by end plates around the beam pipe. The anode plates will have a material budget smaller than 0.25 radiation length. Gas amplification, a readout plane to collect electrons, and the readout electronics will be included in each module. Micro pattern gas detectors will be used to amplify the signal. The amplification technology (MicroMegas or GEMs) is not decided until now.

The point resolution of about  $60 \mu\text{m}$  in the  $r\phi$  plane and about 0.4 mm in the  $rz$  plane is required. A summary of all parameters describing design and resolution goals are given in Table 4.2. For momentum measurements

#### 4.7. TPC for the International Large Detector

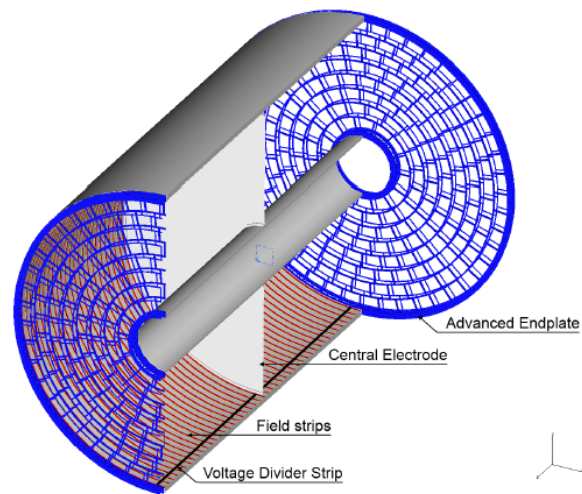


Figure 4.10.: Drawing showing the main parts of the TPC for a future LC [ILC13]

the whole TPC will be located in a magnetic field of 3.5 T. The field must be homogeneous to achieve the good tracking performance of the detector.

#### 4. TIME PROJECTION CHAMBER

Length	4700 mm
Outer radius	1808 mm
Inner radius	329 mm
Material Budget (outer field cage)	$\simeq 0.05X_0$
Material Budget (readout endcaps)	$< 0.25X_0$
Solid Angle Coverage	Up to the $\cos\theta \simeq 0.98$
Number of Pads	$\simeq 1\text{-}2 \times 10^6$ per endcap
Pad Size	$\simeq 1\text{-}6$ mm (about 220 rows)
Point Resolution in $r\phi$	$\simeq 60 \mu\text{m}$ for zero drift
Point resolution in $rz$	$< 100\mu\text{m}$ over full drift length
$dE/dx$ resolution	$\simeq 5\%$
2-hit resolution in $r\phi$	$\simeq 2$ mm
2-hit resolution in $rz$	$\simeq 6$ mm

Table 4.2.: Resolution goals and design parameters for a TPC in the ILD [ILC13]

## EXPERIMENTAL SETUP IN SIEGEN

---

At the University of Siegen there exists two TPCs. A common gas system can provide different mixtures to both chambers. Both TPCs use GEMs for the electron amplification. Each TPC has its own high voltage supply.

### 5.1 HIGH VOLTAGE AND GAS SYSTEM

The high voltage system and the gas system have been developed at the University of Siegen in cooperation with the electrical and mechanical workshops. Photos of both systems are shown in Figure 5.1. The high voltage system and the gas system play an important role in the successful operation of the TPC prototype. The high voltage system has to provide the exact voltages to the cathode and GEMs in order to create all fields accurately inside the TPC.

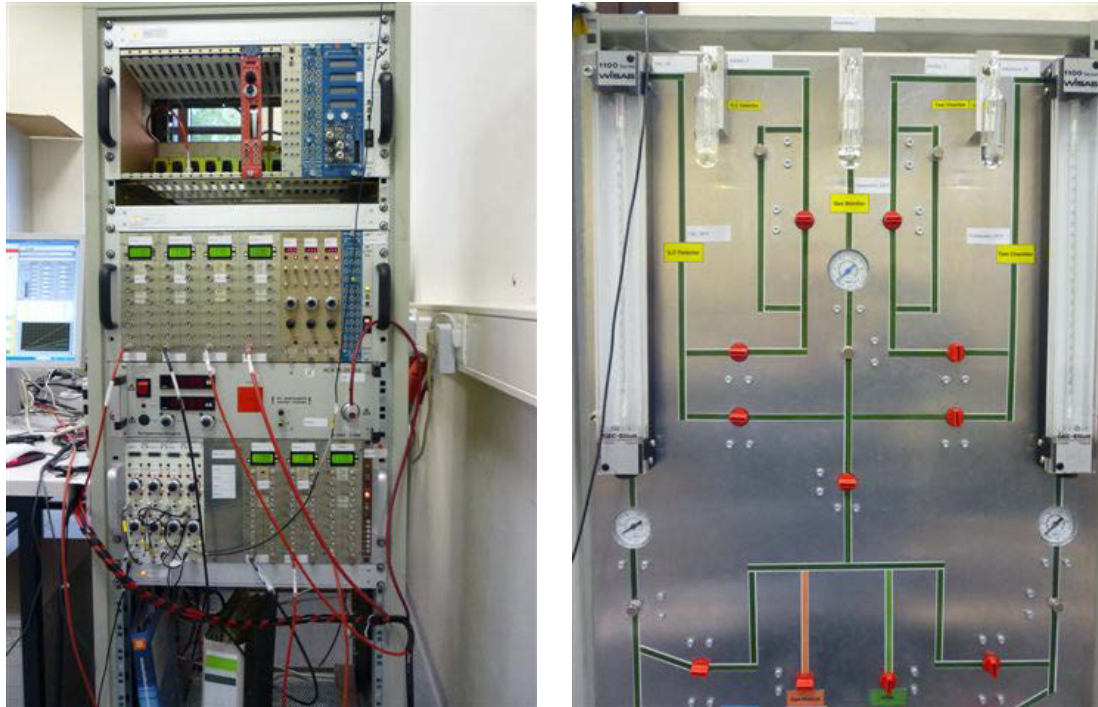
A careful selection and monitoring of the gas quality is essential for a stable operation of the TPC. The gas amplification changes with temperature, pressure and gas impurities. The presence of impurities like oxygen or moisture can affect the drift of the electrons and consequently the overall performance of the detector. Considering the importance of the gas quality and applied voltages it is necessary to design these systems in a precise way.

#### 5.1.1 *High Voltage System*

In principle there are two different possibilities to apply high voltage to the upper and lower side of a GEM. Using only one power supply and a voltage divider is one possibility. The voltage divider consists mainly of a series connection of many resistors. The disadvantage of such a setup is, that one can only set a specific voltage for every GEM before starting the system. If one wants to change the electric fields for GEMs or between them, one has to shut down the whole system, unsolder the old ones and solder new resistors into the voltage divider.

The second option is the usage of separate power supplies for each connection (upper and lower side of a GEM). In the case of three GEMs at whole, seven supplies are necessary: six supplies to cover both sides of each GEM and one supply for the cathode. In order to check the currents inside the system continuously, it is also recommended to connect one current meter

## 5. EXPERIMENTAL SETUP IN SIEGEN



(a) High voltage system including high voltage supply and current meters

(b) Gas system showing gas flow in and out from chamber

Figure 5.1.: High voltage and gas system for the TPC Prototype in University of Siegen

for every connection into the circuit, in order to let the system shut down itself immediately in case of a current, which is higher than the current limit given inside the current meters. Short circuits inside the TPC or sudden sparks between two GEM surfaces can cause such currents.

It is highly recommended to increase the voltage of the GEMs in discrete steps in order to train them. Therefore it is preferable to control the power supplies with a computer and to use a software algorithm to increase or decrease the voltages. For the prototype in Siegen a LabView<sup>1</sup> routine is used for ramping up each power supply separately. Figure 5.2 shows some screen shots of the LabView routine for the used power supplies.

---

<sup>1</sup> LabView (Laboratory Virtual Instrumentation Engineering Workbench) is a graphical programming language, which supports the controlling and readout of electronic devices such as voltage supplies and current meters.



## 5.1. High Voltage and Gas System

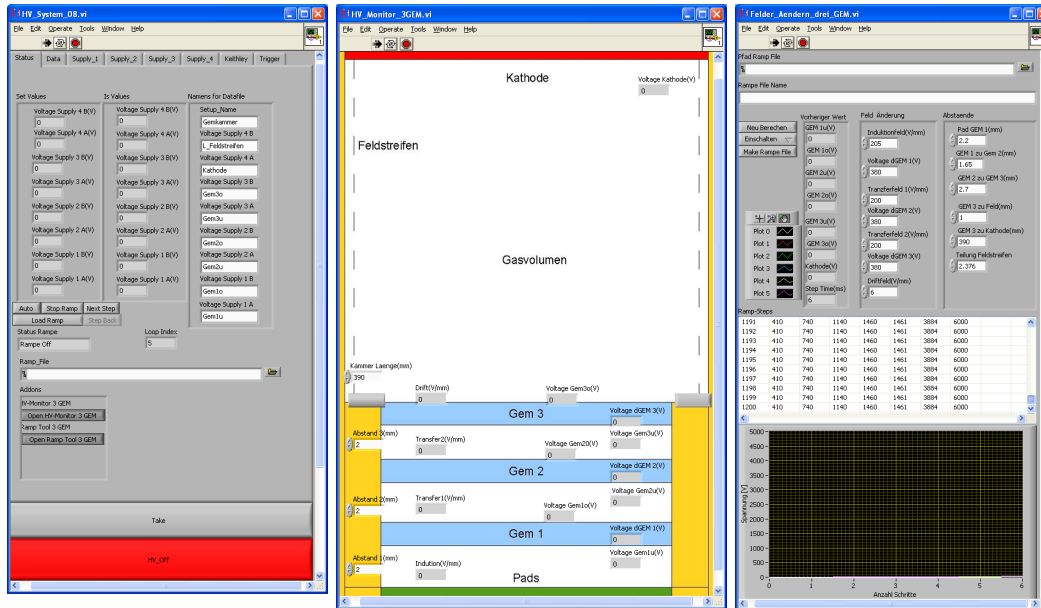


Figure 5.2.: Screen shot of the LabView Software, which is used for ramping up the TPC prototype. Inside the right window one can define the electric fields and create a specific ramp file. The created file is loaded into the left window, which also controls the power supplies. The window in the middle gives an overview over the voltages at each GEM and the electric fields during the ramp phase.

### 5.1.2 Gas System

The gas system contains two parts: Gas monitoring and gas mixing. With the used gas system it is possible to use either premixed gas bottles or to mix different gases in different quantities like ArCO<sub>2</sub> with the ratios 70:30, 80:20 or 90:10, which have been used for the later measurements.

The gas monitor has the task to check the gas quality in order to guarantee good results during the whole measurement. A schematic is shown in Figure 5.3. In principle this gas monitor consists of a box including a small tube, which works like a proportional counter. In the middle of this tube there is a small wire, which creates high electric fields around it, after applying a high voltage between this wire and the outside metal tube.

The gas system can be arranged like this, that the gas flows through this tube before flushing into the TPC. Next to the tube there is a radioactive <sup>55</sup>Fe source, which sends photons into the direction of the tube. While passing through the flowing gas mixture the photons ionise some of the gas atoms and

## 5. EXPERIMENTAL SETUP IN SIEGEN

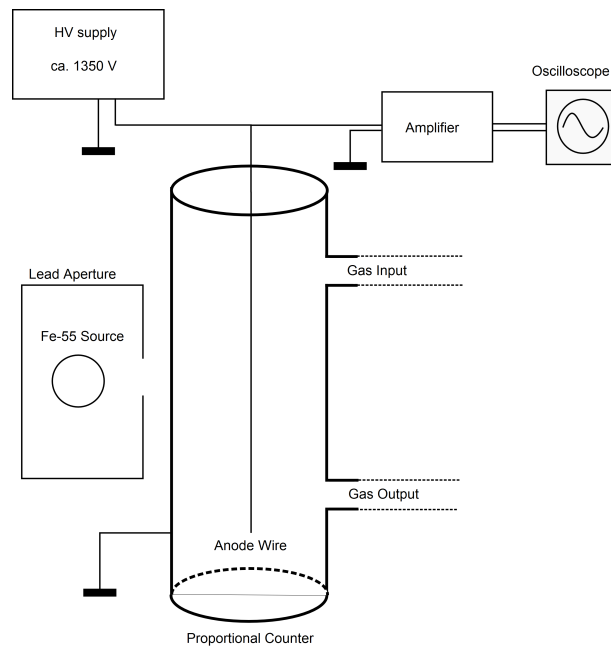


Figure 5.3.: Schematic of the gasmonitor. The photons from the  $^{55}\text{Fe}$  source ionise the gas inside the proportional counter. Due to an electric field between the outer surface of the counter tube and the middle wire, a signal is created, which can be measured via an amplifier by an oscilloscope or a MCA.

create electron avalanches near the anode wire of the small counter. This leads to an electrical signal, which can be measured either by an oscilloscope or a multi-channel-analyser (MCA).

By using a MCA a complete spectrum of the signals can be measured. A sample spectrum, that has been measured with a MCA, can be seen in Figure 5.4. The larger the channel number the higher the signal peak, i.e. also a higher ionisation energy. A detailed description can be found in [Sch11]. As explained in section 3.1 the spectrum shows two peaks. Their positions depend on the used gases and the energy of the photons. One peak is the characteristic peak of the  $^{55}\text{Fe}$  source and one is the escape peak, which has always a smaller energy.

### 5.2 THE TEST CHAMBER

In the laboratory of the University of Siegen there are two TPCs, one large prototype which is described in section 5.3 and a small test chamber. During the last years it has been changed and renewed several times until it reached to the actual setup (see Appendix D.1). The test chamber is a drift detector

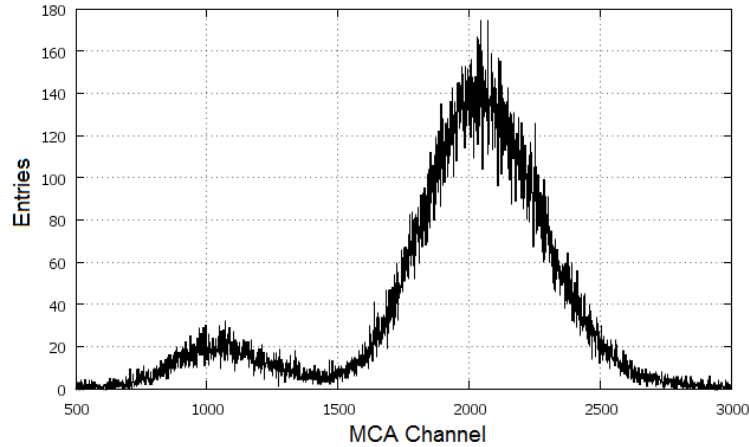


Figure 5.4.: Spectrum of the gas monitor for ArCH<sub>4</sub> measured with a MCA

having the capability to use 2 GEMs for gas amplification. To read out the data a segmented pad plane is used. The main intention of building this test chamber was to test the behaviour of GEMs. For this thesis it was used to test especially the carbon coated GEMs before inserting them into the large TPC prototype. The advantage of this test chamber is the small distance between the cathode and the upper GEM. This gives the possibility to create a very high drift field with low voltages, which is necessary to measure e.g. the ion back drift [Sch11].

### 5.2.1 Mechanical Overview

A sketch of the test chamber is drawn in Figure 5.5. In addition to the standard configuration, it is also possible to use a two or three GEM stack. The drift length between cathode and GEM can be varied from 3 mm to 5.4 mm and the distance between the lower side of the first GEM and the pad plane is 2.4 mm.

The chamber itself consists of a cathode, which has been made out of a copper foil, that is glued on a FR-4 (flame retardant-4) frame. One can choose between frames with two different thicknesses: either 0.4 mm or 1 mm. The cathode is a polyester foil with a thin copper coating of a few nanometers. The small thickness of the cathode allows  $\gamma$  particles to penetrate into the drift volume.

A Printed Circuit Board (PCB) is designed in such a way that all parts of chamber are mounted on it (see Appendix D.3). The PCB has holes for the plastic screws, which hold the cathode and the GEM stack above the pads. There are soldering points on the PCB to establish the electrical connections

## 5. EXPERIMENTAL SETUP IN SIEGEN

between the GEMs resp. the cathode and the high voltage supplies.  $20\text{ M}\Omega$  resistors are connected in series to the surfaces of the GEMs and the cathode in order to reduce the current and protect the system. In Figure 5.6 a three dimensional drawing of the test chamber is shown.

The GEMs, which can be used with this chamber, have a size of  $50 \times 50\text{ mm}^2$ . The PCB is placed on a massive aluminium base plate, which is covered by a thick polystyrol layer to get a good insulation between the aluminium and the PCB. The gas connections for inlet and outlet of the gas are placed inside this base plate. The gas can further circulate inside the complete TPC. The GEMs and cathode are covered by an aluminium frame, which is coated from inside by PVC (polyvinyl chloride) in order avoid high voltage discharges between the frame and the inner setup. Due to this reason there is also a reasonable distance between the frame and GEMs resp. cathode. To make the chamber gas tight, a rubber is placed between the frame and the PCB. The entry window, which consists of transparent polyester, has a thickness of  $50\text{ }\mu\text{m}$ .

The GEM foil is also glued on similar FR-4 frames like the pad PCB. A  $^{55}\text{Fe}$  gamma source is used for gas ionisation. This source has to be put on top of the chamber above the entry window as one can see in the photo of Appendix D.1. The photons can pass this window and the cathode foil very easy and ionise the gas atoms. If the ionisation happens between the cathode and the GEMs, the electrons are multiplied by the GEMs and the signal can be measured on the pads.

### 5.2.2 Pad Plane for Signal Readout

The pads are used to collect the electron signal as a readout in the test chamber. They are accessible on the bottom side of the chamber. Every pad is connected to a separate Charge Sensitive Amplifier (CSA). From the CSA the signals are forwarded to a Gaussian shaping amplifier and measured with the help of a MCA. Both the chamber and amplifier have been placed inside an aluminium box in order to avoid couplings and disturbance from outer signals. The connections for the high voltage supplies and amplifiers are made through this box.

A sketch of the pads geometry, that are used for this chamber can be seen in Figure 5.7. In total there are 32 pads for the test chamber. The pads in the center have a size of  $1.1 \times 6.8\text{ mm}^2$ . They are surrounded by pads with about four times their size. The reason of the different pad sizes is the fact, that the source is normally placed in the center of the entry window, which covers the whole pad area. Therefore one expects the highest amount of electrons in the

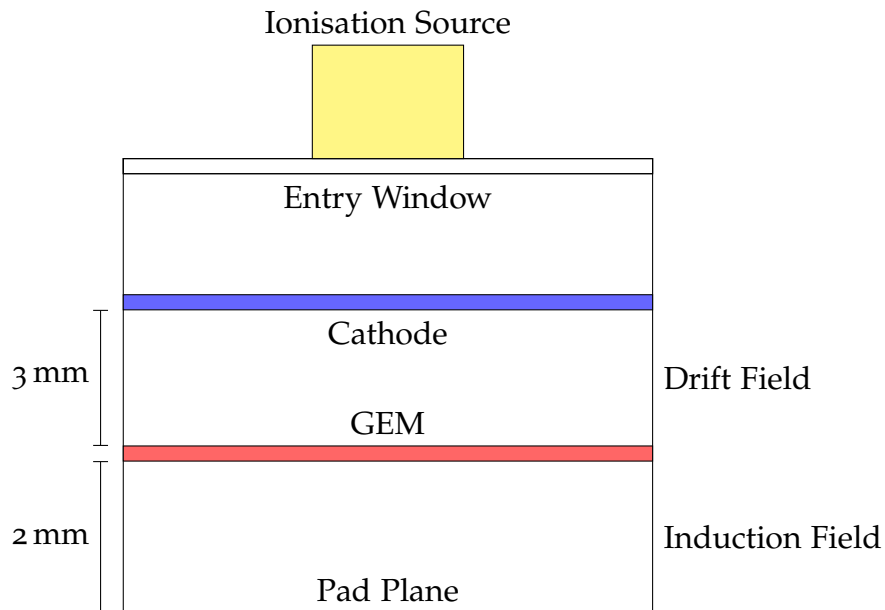


Figure 5.5.: Sketch of the test chamber, which has been developed at University of Siegen. Over the cathode foil of the chamber there is a radioactive source placed on top of an entry window. The ionisation takes place between the cathode and the GEMs, while the signals can be readout with the pads on the bottom side.

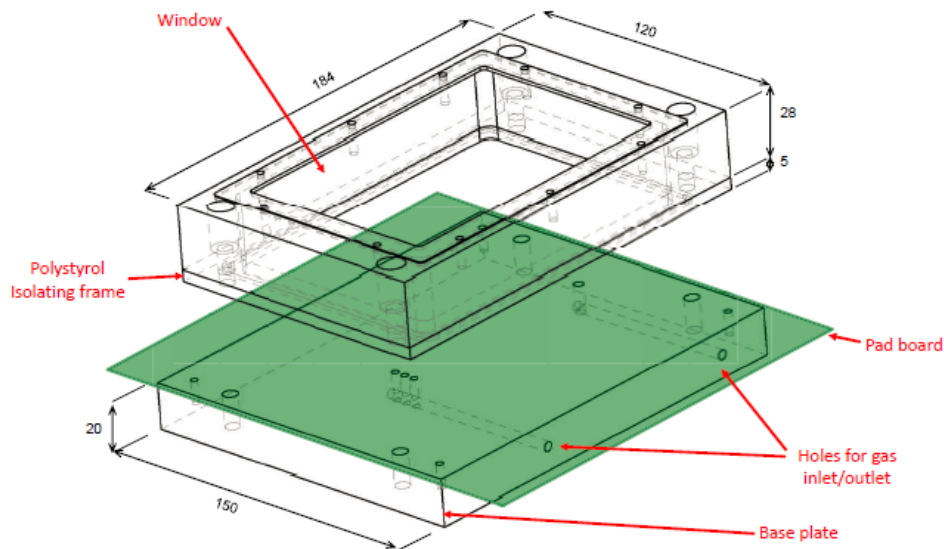


Figure 5.6.: Drawing of the test chamber at the University of Siegen. It shows the covering frame of the chamber and the base plate. The base plate contains two adapters for the gas inlet and outlet.[Gau08]

## 5. EXPERIMENTAL SETUP IN SIEGEN

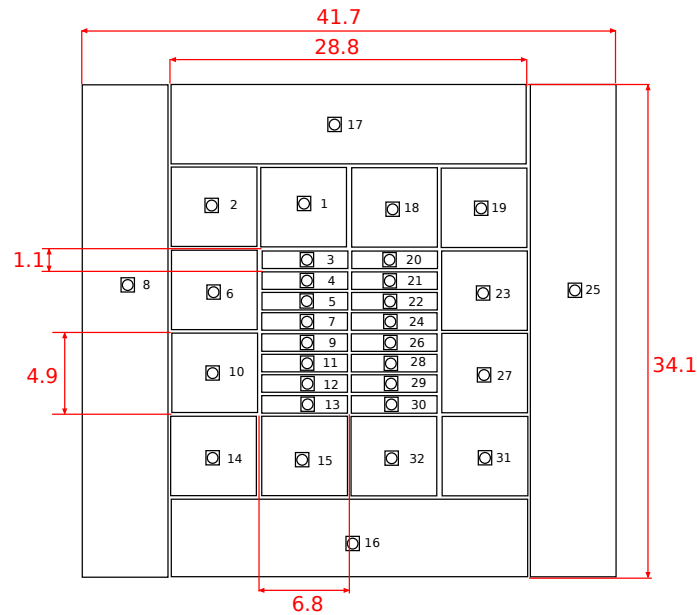


Figure 5.7.: Layout sketch of the pads, which are used inside the test chamber at University of Siegen. The unit of the length numbers is mm.

middle. Due to this reason the inner pads consist of a smaller area, while the outer pads have a much bigger size.

### 5.3 THE TPC PROTOTYPE

The TPC prototype in Siegen is a cylindrical chamber with a diameter of 240 mm and a total length of 400 mm. A sketch is presented in Figure 5.8. The chamber is designed for inserting between one and three GEMs into the TPC. The cathode and anode plate are connected with field strips in order to create a homogeneous electrical field. These strips are made by a flexible printed circuit foil with a parallel connection of resistors.

The outer surface consists of an electrical conducting material, which is kept on ground potential. A list of the used materials can be found in Table 5.1. All materials are chosen to be light weighted under the condition, that the chamber is mechanically robust and allows the application of high electric potential differences without creating short circuits.

The end plates consist of two flat rings, which are fixed at angular brackets. They are attached on the TPC with screws, which make the system gas tight. In addition to this, one tightening ring is used on each end plate. The whole TPC is mounted on aluminium holders, which are designed in the way, that one can move the complete chamber inside the x-y-plane, which is parallel to

## 5.4. Properties of the GEMs used at Siegen

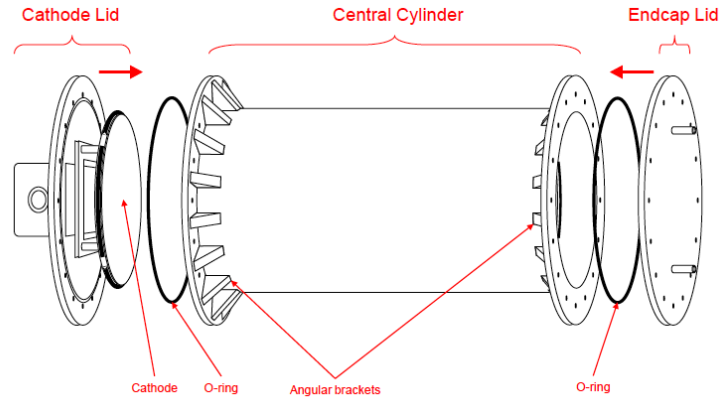


Figure 5.8.: Sketch of the TPC prototype at University of Siegen [Gau08]

the ground surface. The outer look, connections and the aluminium holders can be seen in Appendix D.2.

The end plate, which holds the cathode, has an attached box for a high voltage connector. The voltage limit for the cathode is 8 kV, because of the limitation of the used power supply. Each end plate has two connectors for the gas inlet on the anode side and gas outlet on the cathode side in order to make sure, that the gas flow inside the chamber is homogeneous. The complete description of the parameters (electric fields, distances between GEMs, etc.) for the operation of the TPC will be defined in chapter 8 in detail, since all measurements require different parameter values.

### 5.4 PROPERTIES OF THE GEMS USED AT SIEGEN

After defining the mechanical parameters of a GEM in section 4.3.3, their values have to be calculated according to the GEMs, which are used in the setup of the University of Siegen. The numerical values for the standard GEMs from CERN can be taken from [Sob02] or [Loto6] and will be presented in the following part.

#### 5.4.1 Properties of Standard GEMs

The GEMs have a size of  $100 \times 100$  mm. According to section 4.3.3 the holes are ordered in a hexagonal way and have a double conical structure. The outer radius of the holes is  $D = 70 \pm 5 \mu\text{m}$ , the inner radius  $D = 50 \pm 5 \mu\text{m}$  and the pitch  $P = 140 \mu\text{m}$ . The kapton layer has a thickness of  $k = 50 \mu\text{m}$  while

## 5. EXPERIMENTAL SETUP IN SIEGEN

Material	Company	Thickness [ $\mu\text{m}$ ]	Dielectric Strength [kV/cm]	Dielectric Constant	Density [g/m <sup>2</sup> ]
Flexible Printed Circuit	Korsten & Goossens GmbH	50 (Kapton E) 35 (Copper) 90 (Total)	2755 2755	3.1 (1 kHz)	-
Triflexil 2.5 NKN	Pucaro Elektro Isolierstoffe GmbH	80 (Nomex) 25 (Kapton) 80 (Nomex) 200 (Total)	400	—	190
Glass Filament Fabric (E-glass)	Swiss Composite	100	—	81	—
ECA Honeycomb	Swiss Composite	5	30 (air)	1.1 (9 GHz)	725
Aramid Paper	DuPont	100	206	64	—
Aluminium Foil	—	40	—	108	—
NSC400H	Electro- laube	—	—	—	—
RG 100	Gaugler & Lutz oHG	10000	—	950	—
Fabric- Over- Foam Gasket	Laird Techn. GmbH	—	—	—	—

Table 5.1.: List of materials, which have been used for the construction of the TPC prototype



#### 5.4. Properties of the GEMs used at Siegen

the thickness of each copper layer is  $c = 5 \mu\text{m}$ . The values of the geometrical parameters are as follows:

$$a = 142.781/\text{cm} \quad (5.1)$$

$$b = 0.0623 \quad (5.2)$$

With these parameters and the following values

$$g = 0.01127 \quad (5.3)$$

$$y = 0.0110 \quad (5.4)$$

$$r_{\text{col}} = 0.1090 \quad (5.5)$$

$$s_{\text{col}} = 0.5970 \quad (5.6)$$

$$r_{\text{ext}} = 0.3350 \quad (5.7)$$

$$s_{\text{ext}} = 0.1308 \quad (5.8)$$

one can calculate the effective gain according to the equations (4.7), (4.9) and (4.13). The index "col" stands for the collection and "ext" for the extraction coefficient. For the optical transparency one can find the following value:

$$T_{\text{opt}} = 0.1403 \quad (5.9)$$

For more details and explanations of these parameters one may have a look at [GDG10].

##### 5.4.2 Properties of Carbon Coated GEMs

In section 4.3.5 it is described, that standard GEMs have a limitation in gas gain due to sparks and electrical discharges. In this thesis it shall be shown, that it is possible to avoid these problems by using a conductive coating over the GEM surface. In this case the whole surface of the GEM is covered with a thin layer of diamond like carbon (DLC), which has been done at the *Fraunhofer Institut für Oberflächentechnik*. The measurements of the physical properties are described at the end of the thesis (see Appendix F.3). According to the data sheet surface thicknesses of  $0.5 - 5 \mu\text{m}$  are possible. For the carbon coated GEMs a thickness of approx.  $0.1 \mu\text{m}$  was required. Although it was possible to achieve this value in average, the thickness is not constant throughout the whole GEM surface.

The investigation has been made on GEMs with two different types of carbon coating. One coating is called *SICAN* and defined as  $a\text{-C:H:Si}$ . The other one is called *SICON*. The difference between them is the existence of oxygen in the case of *SICON*, so it looks like  $a\text{-C:H:Si:O}$ .

## 5. EXPERIMENTAL SETUP IN SIEGEN

The electrical resistance of a physical volume like a box or cylinder consisting of one material with constant properties can be calculated by the following formula

$$R = \rho \frac{d}{A} \quad (5.10)$$

where  $\rho$  is the resistivity of the material,  $A$  the area and  $d$  the thickness. In the case of SICON the resistivity is larger than  $10^{10} \Omega\text{cm}$  according the data sheet (see Appendix F.3).

The standard method to create these silicon doped carbon coatings is the *plasma-assisted chemical vapour deposition* (PACVD) (explained in section 7.1) by creating radicals and ions inside a substrate, which leads to a deposition of thin layers of the same material on the surface the probe. The complete description of this method can be found in [Ung91].

### 5.5 THE TIMEPIX-CHIP

The Timepix chip is based on the Medipix2 chip [Med14], which has been developed for the purpose of medical science by the Medipix collaboration. A sketch is presented in Figure 5.9 The Medipix2 chip is a CMOS chip, which can be used as a semiconducting detector. If a particle hits the detector, it creates signals, which can be measured by a pixel of the chip. Every pixel includes a full electrical circuit for amplification and data processing.

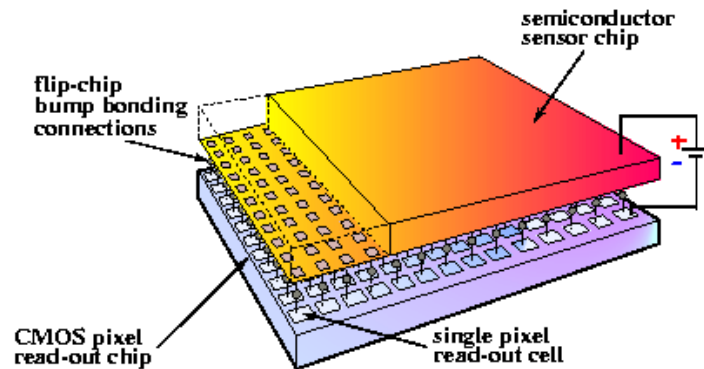


Figure 5.9.: Sketch of the Timepix chip illustrating its layers and geometric configuration [Med14]

Several studies showed, that the chip is working successfully for physics applications. So it had been decided to investigate its behaviour also at the University of Siegen. Since it can also measure the time information of signals, it is suitable for the measurements with a TPC. The Timepix chip itself is

divided into two main parts. The upper part is the charge sensitive layer. It consists of  $256 \times 256$  square pixels. Each pixel has an area of  $55 \mu\text{m} \times 55 \mu\text{m}$ , i.e. the whole active area of the chip is  $14 \text{ mm} \times 14 \text{ mm}$ . Each pixel has a dynamic range of 13-bit, i.e. they can show entries upto a value of 8192. The energy range covers values between 4 and 25 keV.

The lower part (under the charge sensitive layer) contains peripheral electronics like a 256-bit fast-shift-register and a reference voltage source. The chip by itself can be used with a frequency upto 100 MHz. At the lower part of the periphery there are 127 contact points, which can be connected via ultrasonic bonding with the chip PCB.

### 5.5.1 Internal Structure of the Timepix-Chip

Every pixel contains a full readout system. The electronics inside one pixel is divided into an analog and a digital part. Both parts are shown in Figure 5.10. The complete description of the chip can be found in [Llo06].

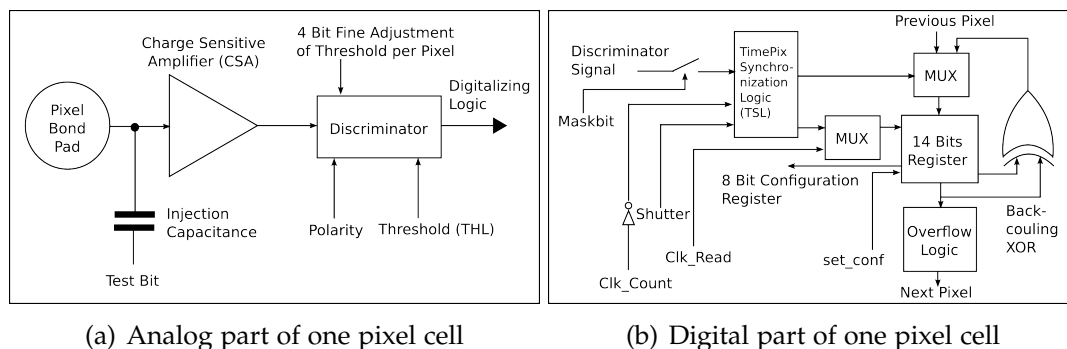


Figure 5.10.: Complete Electrical Circuit inside one pixel of the Timepix chip

#### Analog Part

The signal, which is created on the surface of the chip, is amplified by a CSA, which is included in each pixel. The voltage pulse is proportional to the amount of the deposited charge. The used CSA also shapes the signal, which makes an additional shaping amplifier unnecessary. The amplifier itself consists of an operational amplifier, which is used as an integrator. The back-coupling from the output to the non-inverting input is done with a  $C_f = 8 \text{ fF}$  capacitor. Possible offset voltages at the input can be lead away by a MOSFET<sup>2</sup>.

<sup>2</sup> A special kind of field effect transistor, which has to be controlled by a voltage instead of a current like for normal transistors

## 5. EXPERIMENTAL SETUP IN SIEGEN

The charge, that has been deposited on the chip, first reaches the input of the amplifier and is saved in the capacitor. The voltage difference can be measured at the output of the amplifier as a signal, which is equal to an asymmetrical triangle signal. The next step is the discriminator, which is placed behind the output of the amplifier. In this case a one-threshold discriminator was used.

The signal of the discriminator can be changed between two levels, which makes it possible to process the signal with a logic circuit, called Timepix Synchronization Logic (TSL). If the signal is higher than the set threshold level (THL), the discriminator goes into high level (low-voltage TTL<sup>3</sup> with 3.3 V), otherwise it remains in low level (ground potential).

### *Digital Part*

The digital part of each pixel cell behind the discriminator mainly consists of logic gates inside the TSL. The external shutter window gives the time period for how long signals are received from the discriminator. Depending on the mask of the pixel cell, the TSL either increments the 14 bit register only as long as the discriminator signal is in high level or for the whole length of the shutter window once the discriminator gives a high signal. Nevertheless also other combinations are possible.

### *Pixel Modes*

The four most important modes for each pixel of the Timepix chip are explained below:

- **MediPix Mode:**

Every time, when the signal height is higher than the threshold and the discriminator is in high level the counter of the MediPix register is increased by 1. Therefore this mode counts the number of pulses over the threshold during the time of the shutter signal.

- **Time-Over-Threshold-Mode (ToT):**

The *ToT* mode measures the time for which the discriminator is in high level, i.e. is equal to the time, in which the signal of the amplifier is higher than the threshold. Since this value is proportional to the deposited charge, the *ToT* value of one pixel measures the number of electrons, which reach to this pixel. Therefore this mode is used for collecting the charge informations.

---

<sup>3</sup> Transistor-transistor logic (TTL) is voltage standard for electronic signals with +5 V for standard TTL and +3.3 V for low-voltage TTL

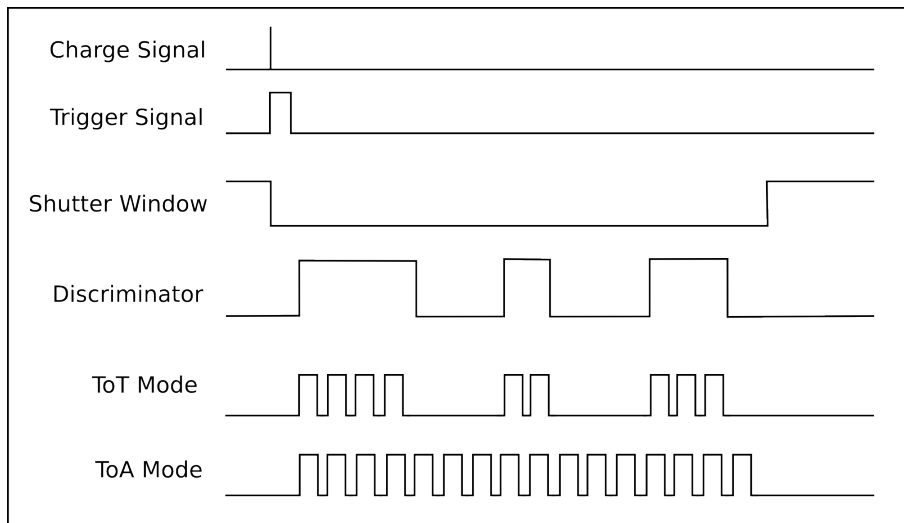


Figure 5.11.: The graphical scheme of the used *ToT* and *ToA* modes of the Timepix chip. The charge signal creates a trigger, which opens the shutter window for the set length. Every time, when the discriminator is in high level, the *ToT* value increases during that time. The *ToA* values increases from the start of the first charge, which arrives, until the end, when the shutter window closes.

- **Time-Over-Amplitude-Mode (ToA):**

In the *ToA* mode the time is measured, that is passing between the point, at which the discriminator is at high level for the first time until the end of the shutter window. Therefore from the *ToA* value the arrival time of the electrons can be calculated.

- **Timepix Mode:**

In Timepix mode the register is only increased by 1 for one time after changing the discriminator level to high until the end of the shutter. Although this is not useful for actual measurements, it can still be used as a counter check for other measurements.

A scheme of these modes is presented in Figure 5.11. All measurements with the TPC prototype are made in the *ToA* and *ToT* modes. For most of the captured frames a chess matrix is used, where the pixels are alternating in *ToA* and *ToT* modes. Further information about the internal structure of the Timepix chip can be found in [Ummo8].

## 5. EXPERIMENTAL SETUP IN SIEGEN

### *Control-DACs*

In order to create a stable operating point, it is possible to change the parameters of voltage and current sources inside the chip with the help of eight Digital-Analog-Converters (DACs). These DACs are defined as follows:

- **IKrum (8-bit):**  
This DAC controls the current source, which is discharging the charge collecting capacitor  $C_f$  in the pre-amplifier circuit, so it is possible to change the signal width, which is reaching the discriminator, between several hundred and several thousand nanoseconds.
- **IPreamp (8-bit):**  
This DAC controls the time constant of  $C_f$  and therefore the rising time of the signal, which can be chosen between 90 and 180 ns.
- **THL (10+4-bit):**  
This DAC controls the global threshold level of the discriminators, which can be changed in  $400 \mu V$  steps.
- **THS (8-bit):**  
This DAC controls the current  $I_{THS}$  with which one can change the threshold level for each discriminator separately inside small intervals. This parameter is therefore important for the threshold calibration of the chip, which is explained in section 6.2.
- **FBK (8-bit):**  
This DAC controls the height of the output signal of the amplifier and therefore the dynamic range of the following discriminator.
- **Hyst (8-bit):**  
This DAC controls the hysteresis of the discriminator in order to make sure, that it always goes back to low level. This parameter is important, if the input signal of the discriminator is overlapped by noise.
- **VCas (8-bit):**  
This DAC controls the voltage of the cascade circuit, which is needed to stabilize the input capacitance of the pre-amplifier.
- **Disc (8-bit):**  
This DAC controls the supply voltage of the discriminators.

## 5.5.2 USB Readout System

The USB readout system is one possible device to establish a connection between the Timepix chip and the PC. The software, which can read and show the data from this device, is called Pixelman software [Pix13]. A picture of the front side of the USB device is shown in Figure 5.12. The most important connection possibilities can be seen from Table 5.2. The range of the ADC input and DAC output voltage range is from 0 to 2.5 V with 12-bit precision. For the trigger input 5 V TTL signals have to be used.

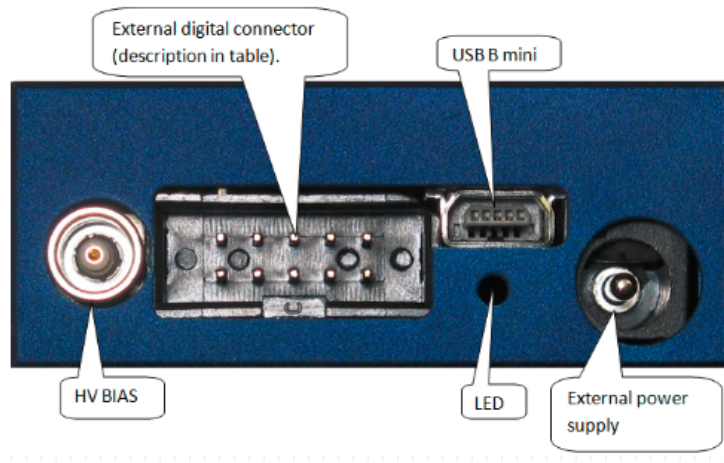


Figure 5.12.: Picture of the USB device for the Timepix chip. The upper right connector is defined as pin 1 and lower left as pin 10. [Vy14]

Pin No.	Description
1	Ground
7	Test pulse input
10	Trigger input

Table 5.2.: Connection pins of the USB device

## 5. EXPERIMENTAL SETUP IN SIEGEN

### 5.5.3 Virtex-6 FPGA ML605

The newest readout system is the so called Virtex 6 readout. This is basically a special Field Programmable Gate Array (FPGA) card, which is connected to an intermediate board as a bridge connection to the Timepix chip. The Timepix chip by itself is placed with connectors on top of another board, which can be fit directly into the endplate of the TPC prototype. Figure 5.13(a) shows a picture of the FPGA card and 5.13(b) of the intermediate board with a description of all connections, that have been used during the measurement and the calibration of one Timepix chip.

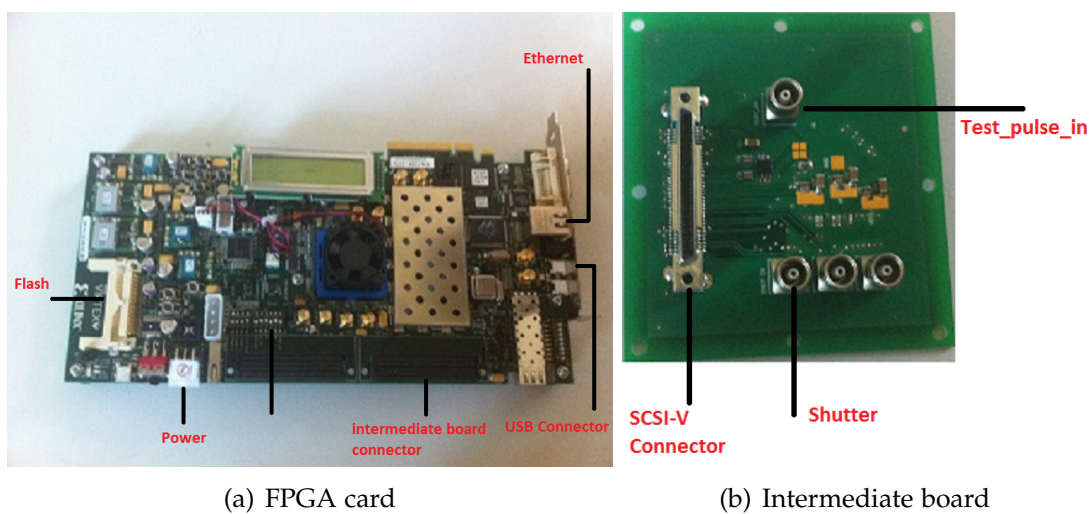


Figure 5.13.: Photos of the FPGA card and the intermediate board, which is used to connect the card with the Timepix chip

The Timepix board has two power connections (one analog with 2.2 V and one digital with 5 V), for which a low power supply is needed. The complete connection scheme is shown in Appendix D.4. The firmware is still under development, but can already be used for calibration and data taking. The readout software related to this card is named Timepix Operating Software (TOS).

The firmware for the FPGA card is mainly written in VHDL and module based. These modules are used to establish the connection between the PC and the Timepix chip via ethernet connection. With the help of zero suppression and parallel data management it is possible to achieve the maximum frequency upto 100 MHz for the readout of one single chip. A more detailed description of the card and the firmware can be seen [Lup14]. A summarized scheme of the working principle of this firmware is shown in Figure 5.14



## 5.6. Scintillator Hodoscope for TPC Prototype

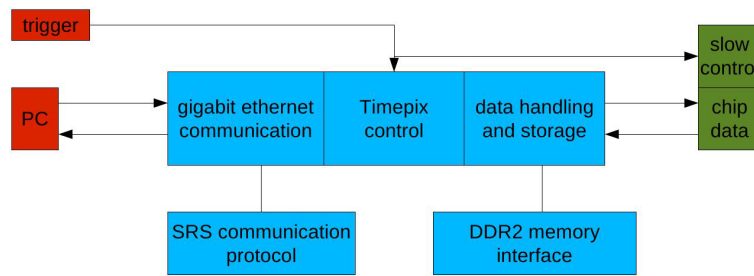


Figure 5.14.: Scheme of the working principle of the FPGA firmware [Lup14]

### 5.5.4 Software for the Readout

#### *Pixelman Software*

The Pixelman software is the original software regarding the Timepix chip. It can be used with the USB readout system [Vyki14] and MUROS [Nik14]. Further information about this software is given in section 8.2.

#### *Timepix Operating Software*

The software, which is used with the Virtex 6 FPGA card is named TOS and has been mainly developed at the University of Mainz with minor changes from University of Bonn. This software is still under development. Despite that, all functions, which are necessary for measurements and calibrations, are already implemented and working sufficiently. The firmware of the FPGA card has to be uploaded before every measurement because of missing flash memory.

Until now the software is not including any GUI, i.e. that all commands have to be typed into the terminal of Linux after starting the software. For all commands there are either integers or abbreviations defined. The typing orders of the commands is very important. Otherwise data taking will either not work or give wrong results. The parameters of the Control-DACs have to be written in one text file, which has to be applied after starting the software. The important commands with the referring descriptions are presented in Appendix A.

## 5.6 SCINTILLATOR HODOSCOPE FOR TPC PROTOTYPE

In order to detect cosmic muons with the TPC Prototype a hodoscope of two scintillators is used, which are placed above and under the TPC. A description of the setup and the presentation of test results has been done in [Bieo8]. One can see in Figure 5.15, that each scintillator is connected to a separate

## 5. EXPERIMENTAL SETUP IN SIEGEN

high voltage power supply. The produced signals are amplified by an octal pre-amplifier and then used to create gates with two discriminators.

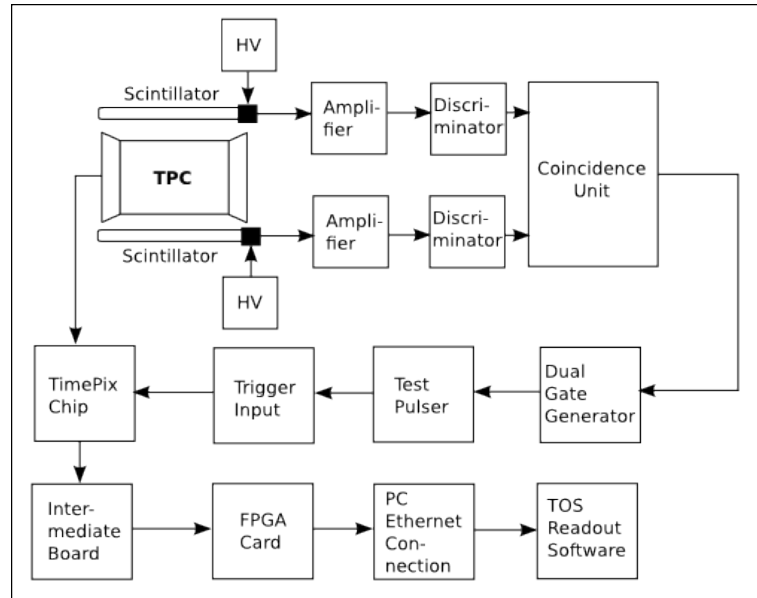


Figure 5.15.: Sketch of the hodoscope setup for the TPC prototype

Both discriminator signals are being overlapped in one coincidence unit. This makes sure, that there will be only a gate signal, if both scintillators measure a muon inside a specific time window, that can be fixed by adjusting the width of the gates. Because of the large geometry of the scintillators it can happen, that the track of the muon is not in the field of view of the Timepix chip. The dual gate generator is creating a 5 V TTL gate from this signal, which is then changed into a 3.3 V low voltage TTL gate with the help of the pulse generator. This procedure is necessary, because the used modules are not able to produce a gate signal with the correct output voltage 3.3 V.

The TTL gate is then used as a trigger signal for the Timepix chip. Every time, when both scintillators are measuring a signal in a short time window, the shutter of the Timepix chip opens for a defined time, which depends on the length of the scintillators and the assumed drift velocity for a specific gas mixture, temperature and pressure. From these parameters and the measured  $ToA$  values from the chip, it can be calculated, in which distance to the chip the muon passed the TPC.

## 5.7 IONISATION METHODS

5.7.1 *UV-Laser*

The UV-laser [Cry14], which is used to create tracks inside the TPC prototype, has a wave length of 266 nm and creates pulses with a length of 1 ns. Every pulse has an energy of 10  $\mu$ J. The area of the laser beam is 0.85 mm<sup>2</sup> and the pulse frequency can be set between 1 Hz and 2.5 kHz. Inside the TPC prototype there are three entry and exit windows for the laser. The windows consist of thin glass and are covered by a cylinder made from acetal. After fixing the chamber into the right position, the laser has to be adjusted in the way, that it goes exactly through both sides and is parallel to the Timepix chip surface. On the opposite side of the laser there is a possibility to fix a photo diode, which creates voltage signals every time, when it is hit by the beam. The signal is then being amplified and sent to a discriminator to create a gate, which can be used as an external trigger for the Timepix chip.

5.7.2 *X-Ray-Sources*

There are two different  $\gamma$  sources available. One is a <sup>55</sup>Fe source with a photon energy of 5,1 keV. It is equal to the one, which is used inside the gas monitor, but with a higher decay rate. The other available source is a variable x-ray-source. It mainly consists of Americum-241, which sends out alpha particles with an energy of 5.638 MeV. These alpha particles hit a target with a choosable material like molybden or rubidium from which they kick out the electrons in the inner shell of the atoms. The electrons from the outer shells, which have to fill that gap, send out x rays with energies, which are characteristic for the chosen target material. The photon energy is therefore equal to the  $K_{\alpha}$  line of that material. A list with the choosable materials and their energies can be found in Table 5.3.

Element	$K_{\alpha}$ Energy
Rubidium (Rb)	13.37 keV
Molybden (Mo)	17.44 keV
Silver (Ag)	22.10 keV
Barium (Ba)	32.06 keV

Table 5.3.: Energies for different elements inside the variable x-ray-source

## 5. EXPERIMENTAL SETUP IN SIEGEN

Both x-ray-sources have been mainly used for the gas ionization inside the test chamber because of their advantage to ionize the gas with the photo effect and therefore create a small point of charge inside the gas volume. Also some measurements with the TPC prototype in combination with the USB device have been performed.

### 5.7.3 Beta-Ray-Sources

For the  $\beta$ -ray-source, with which one can create complete particle tracks,  $^{90}\text{Sr}$  with an activity of 37 MBq is used. On the opposite side of source there is the possibility to install a PMT with a special scintillator material in order to create a signal, whenever an electron goes through the TPC and reaches the entry window of the PMT. In the same way as for the laser this signal can be used as an external trigger. For setting the shutter length and making analysis, one has to keep in mind, that the electrons of the source are not moving with the speed of light, i.e. the time difference between reaching the pixel chip and creating of the trigger signal has to be added to the total time.

For the electrons, that are emitted by  $^{90}\text{Sr}$  the following energy equation holds:

$$W = W_0 + W_{\text{kin}} \quad (5.11)$$

There  $W = mc^2 = \gamma m_0 c^2$  stands for the relativistic energy,  $W_0 = m_0 c^2$  for rest energy and  $W_{\text{kin}}$  for the kinetic energy of the emitted electron. By inserting these relations into the equation (5.11) together with the Lorentz factor  $\gamma = 1/\sqrt{1 - v^2/c^2}$  the following formula for the speed  $v$  of the electrons can be derived:

$$v = c \sqrt{1 - \frac{1}{1 + \left(\frac{W_{\text{kin}}}{m_0 c^2}\right)^2}} \quad (5.12)$$

The maximum energy of  $^{90}\text{Sr}$  is  $E_\gamma = 546 \text{ keV}$  [PTE14], which leads to a maximum electron speed of  $v = 0.73 c$ . But still the less energetic electrons can have a much smaller velocity.

### 5.7.4 Cosmic Muons

Primary cosmic radiation, which comes from the outer space, mainly consists of protons. If this proton has an energy, which is above around 10 GeV, the proton is able to create secondary cosmic rays by scattering on gas nuclei in the higher atmosphere. Due to the collision of the proton with air molecules a lot of new particles are created, which is called particle shower. Most of the particles are pions (with positive, negative and neutral charge), neutrons and

protons. While the neutral pions decay by emitting photons, the charged pions decay into positively and negatively charged muons. The decay reactions are shown below:

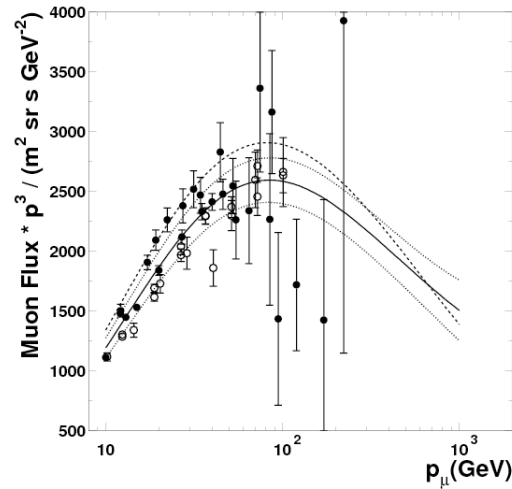


Figure 5.16.: The result on the muon flux. The dotted lines show the 1 sigma error band, whereas the dashed curve is the description by Bugaev. The points are the data used in the normalization procedure. The open points stand for experiments using a superconducting magnet, the black points indicate conventional magnets. [Hebo2]

These muons have a very high velocity and due to the time dilation of the special theory of relativity most of the muons can reach the surface of the earth before decaying into electrons. For measurements with cosmic muons it is important to know the amount of muons, which reach the area of both scintillators. For this it is helpful to define the differential particle flux density according to the following formula [Hebo2]:

$$\frac{d\phi(p, \theta)}{dp} = \frac{dn(p, \theta)}{d\Omega dp dA dt} \quad (5.16)$$

where  $\phi$  is the total particle flux,  $p$  the momentum of the particle,  $A$  the area,  $\Omega$  the solid angle and  $t$  the time. With the help of the measured momentum spectrum for muons, which is shown in Figure 5.16, and sphere integration

## 5. EXPERIMENTAL SETUP IN SIEGEN

over the differential flux one can calculate the number of muons per area per time  $f/A$  in sea level to

$$\frac{f}{A} = \mathcal{O} \left( \frac{1}{\text{min} \cdot \text{cm}^2} \right) \quad (5.17)$$

Therefore a detector has to run a long time in order to take a significant amount of muon tracks for a proper analysis or needs a large detection area. Because of the positive charge of protons, the amount of the produced  $\mu^+$  is higher compared to the amount of  $\mu^-$ , which can be interpreted as a direct effect of the charge conservation law.

Muons are minimum ionising particles (MIPs), i.e. their energy loss is the minimum loss, which a particle can have, when it passes through matter. In the case of Argon, which has the nucleus number  $Z = 18$ , the energy loss of MIPs is approx.  $1.5 \text{ MeV cm}^2/\text{g}$  as one can see from Figure 5.17. The density of Argon is  $1.784 \text{ kg/m}^3$  for  $0^\circ\text{C}$  and standard pressure. Converting this value into  $\text{g/cm}^3$  and multiplying the energy loss per track length gives the value

$$\frac{dE}{dx} = 2.6775 \frac{\text{keV}}{\text{cm}} \quad (5.18)$$

Under the assumption, that the electron passes the full diameter  $d = 24 \text{ cm}$  of the TPC, this leads to a total energy loss of

$$\Delta E = 64.26 \text{ keV} \quad (5.19)$$

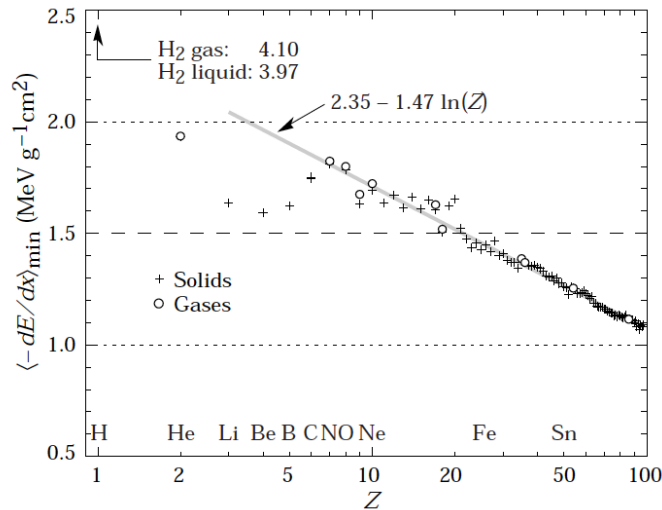


Figure 5.17.: Energy loss of MIPs in matter [BGK05]

## CALIBRATION OF TIMEPIX CHIP

---

The calibration of a Timepix chip is necessary for the measurement of the charge arriving at each pixel. It is performed by sending external test pulses to the pixels [Brz13] [Kro12]. For the presented calibration method a standard Timepix chip with the ID Ho4-W19<sup>1</sup> was used, with which later also the measurements with cosmic rays (see chapter 8) have been performed. Different steps are necessary to correct the time and charge measurements of each pixel. Pixels with time informations have to be corrected for effects like clock distribution delay and timewalk. Pixels with the charge information will need to be corrected for threshold offset and electron conversions [Ulm11]. In general the calibration of the TimePix includes the following five main steps:

1. Threshold (*THL*) equalization
2. Charge (*ToT*) calibration
3. Timewalk (*ToA*) compensation
4. Threshold offset (S-Curve) calibration
5. Time delay compensation

The details of each calibration step will be explained in the following sections. The calibration parameters for charge and arrival time are calculated from the calibration measurement data (see sections 6.3, 6.4) and will be used later for detailed analysis in chapter 8. The shutter time and the threshold level, which is used for the calibration, must be constant during the whole measurement. For the complete calibration chain the Timepix Operating Software ((TOS) is used (see section 5.5.4). The external test pulses, which were needed for the calibration, have been created by a pulse generator.

### 6.1 TIMEPIX OPERATING SOFTWARE

TOS provides all options to operate the pixels inside the Timepix chip in all different four modes (see section 5.5.1) . With the help of TOS the calibration and data taking has been performed in a successful way. The complete set of

---

<sup>1</sup> The ID of a Timepix chip is given by the order of the production and is unique for each chip.

## 6. CALIBRATION OF TIMEPIX CHIP

functions from the pixelman software for the USB readout system and MUROS can be achieved by TOS. It is possible to read a maximum of 32 Timepix chips at the same time, which is planned to be extended to 99 chips for the end of 2014.

- **DAC Scan**

Before starting any kind of calibration measurement, it is important to check all DAC values of the chip. For this purpose a DAC scan is recommended. All the DAC values are stored in a FSR file with the name `fsr.txt`, which one has to load every time before starting a new calibration or measurement. It contains all DAC values, which are necessary to operate the chip. The same file must be used for the complete set of data for the same chip after a successful calibration. The DAC values for the calibration and data taking are given in Table 6.1.

<b>IKrum</b>	<b>Disc</b>	<b>IPreamp</b>	<b>Hyst</b>	<b>THL</b>
5	127	255	0	400
<b>THLCorse</b>	<b>VCas</b>	<b>FBK</b>	<b>GND</b>	<b>THS</b>
7	130	128	80	76

Table 6.1.: Setting of the Timepix DACs during calibration and data taking

- **THS Optimisation**

The global threshold level for each pixel varies slightly because of the electronics inside the chip. Therefore the THS optimisation is the first step in the calibration chain. It changes the correction current  $I_{THS}$  continuously with the 8-bit register from 0 to 50 nA and calculates the value for  $I_{THS}$ , for which the deviation between the thresholds of the different pixels reaches a minimum. This number is then stored inside the FRS file and the standard deviation is calculated.

The threshold and mode of each pixel of the Timepix chip can be controlled individually by the software. It is also possible to implement mode maps (see Figure 6.1) on the whole chip, in order to set the pixels independently into different modes. This is an important feature of the Timepix chip in the data taking phase, since it is not possible for one pixel to measure charge and time information at the same time.

For this purpose normally a mixed mode map is applied to the chip, in which the pixels are set into different modes in the same way like a chess



board pattern. The name, which is given to this special mask, is therefore called ChessMatrix, in which one can set the first pixel in time (*ToA*) mode and the other in charge (*ToT*) mode or vice versa. This mode map gives the possibility to record the time and charge information of one track at the same time. The values for setting a mask for the chip is shown in Table 6.2. The list of all commands, which are used by TOS, is listed in Appendix A.

ToA	ToT	ToA	ToT	ToA	ToT	ToA	ToT
ToT	ToA	ToT	ToA	ToT	ToA	ToT	ToA
ToA	ToT	ToA	ToT	ToA	ToT	ToA	ToT
ToT	ToA	ToT	ToA	ToT	ToA	ToT	ToA
ToA	ToT	ToA	ToT	ToA	ToT	ToA	ToT
ToT	ToA	ToT	ToA	ToT	ToA	ToT	ToA

(a) The first pixel is set to *ToA* is creat a mask know as Mixed-mode Map 1 (MM1)

ToT	ToA	ToT	ToA	ToT	ToA	ToT	ToA
ToA	ToT	ToA	ToT	ToA	ToT	ToA	ToT
ToT	ToA	ToT	ToA	ToT	ToA	ToT	ToA
ToA	ToT	ToA	ToT	ToA	ToT	ToA	ToT
ToT	ToA	ToT	ToA	ToT	ToA	ToT	ToA
ToA	ToT	ToA	ToT	ToA	ToT	ToA	ToT

(b) The first pixel is set to *ToT* is creat a mask know as Mixed-mode Map 2 (MM2)

Figure 6.1.: Mask pattern for Timepix calibration and data acquisition

Pixel	Medipix	1 hit	ToT	ToA
P <sub>0</sub>	0	0	1	1
P <sub>1</sub>	0	1	0	1

Table 6.2.: Setting of pixel values in TOS according to the operating modes of the Timepix chip

## 6.2 THRESHOLD EQUALISATION

The next step in the calibration chain after the THS optimisation is the threshold equalisation. It sets the 4 bits  $I_{THS}$ ,  $I_{THS}/2$ ,  $I_{THS}/4$ ,  $I_{THS}/8$  first to 0000 and measures for each pixel the *THL* value at which it registers a signal. This distribution for all pixels can be seen in Figure 6.2 (red curve). The blue curve shows the distribution for all pixels after setting the 4 bits to 1111. All values in between are calculated by TOS via a linear interpolation. From these values a pixel mask is created and saved in the file *threshold.txt*, which contains the *THL* level for every pixel. After applying this correction mask to the Timepix

## 6. CALIBRATION OF TIMEPIX CHIP

chip the standard deviation can be minimised, as one can see from the black curve in Figure 6.2.

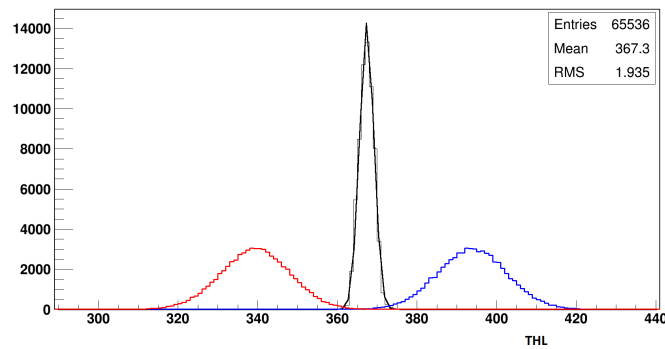


Figure 6.2.: The output of TOS for the threshold equalisation referring to a standard Timepix chip. First the correction current is set to the minimum value while scanning the signal of each pixel for different  $THL$  levels (left red curve) and then again while setting the correction current to the maximum level (right blue curve). The middle black curve then shows the standard deviation after optimising the threshold values.

After this the software tries to set the threshold of every pixel as close as possible to the mean threshold value calculated from the distribution. The performance of the chip can be seen in the rms value, which should not be higher than 1.9 for a good chip. The result of the equalisation improves the threshold variation of  $\sim 240e^-$  rms to the achieved noise-free-threshold variation of  $\sim 35 e^-$  rms after the equalisation. With the help of the threshold equalisation the amount of the minimum detectable charge can be reduced to  $\sim 650e^-$  for each pixel, which is 2.5 times smaller than the value before equalisation.

Later this file has to be loaded before starting the data taking. It is essential for the calibration, that the threshold level should be set to the same  $THL$  as it will be used in the later measurements. For a better  $THL$  equalisation it is recommended to choose a spacing of 2. It is also possible to use a spacing of 4, 8, 16, 32 and 64. A spacing of the integer value  $n$  means, that from a square of  $n \times n$  pixels the test pulse is given to only one pixel. In order to apply the test pulses to all pixels, it is therefore necessary to repeat the measurement  $n^2$  times, which is automatically done by TOS.

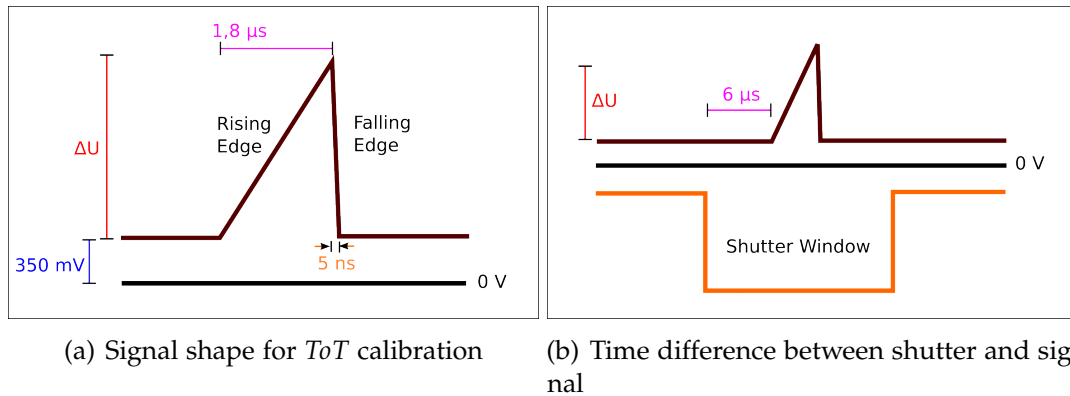


Figure 6.3.: Signal shape for the *ToT* calibration. The offset is constant with a value of 350 mV. The amplitude  $\Delta U$  has to be set to the chosen signal height. The number of test pulses has to be set to one and the time delay between shutter opening and rising edge must be 6  $\mu\text{s}$ .

### 6.3 CHARGE CALIBRATION

To convert the number of *ToT* clock cycles into charge, a charge calibration is required. For the charge calibration test pulses have to be given to the pixels of the Timepix chip by an external pulse generator. These pulses must consist of a slow rising edge (in this case  $t_1 = 1.5 \mu\text{s}$ ) and a directly following fast falling edge of  $t_2 = 5 \text{ ns}$ . The signal shape is displayed in Figure 6.3. The length of the shutter window, which is used for the following calibration, is 35  $\mu\text{s}$ . For all shutter window lengths, that are used for different measurements, these calibration steps have to be repeated.

The shutter window, which is set to a time value of 35  $\mu\text{s}$ , is used as a trigger for the pulse generator. A delay of 6  $\mu\text{s}$  between the starting point of the shutter window signal and starting point of the test pulse signal has been set. The software is able to read out the *ToT* values for each of the  $256 \times 256$  pixels. For the charge calibration the chip is set to *ToT* mode. For an optimum in measurement time and accuracy a spacing of 8 is used. This gives a homogeneous response over the complete pixel matrix. All pixels can be combined in one calibration, because a uniform gain, threshold and feedback current can be assumed.

All measurements are repeated for different pulse heights at whole four times and the average value is used. The distribution of the pulses over the chip is handled by the electronics of the Timepix chip and the control of the test pulse distribution is done with TOS. After the measurements are finished, these values can be plotted inside a histogram. Such a distribution

## 6. CALIBRATION OF TIMEPIX CHIP

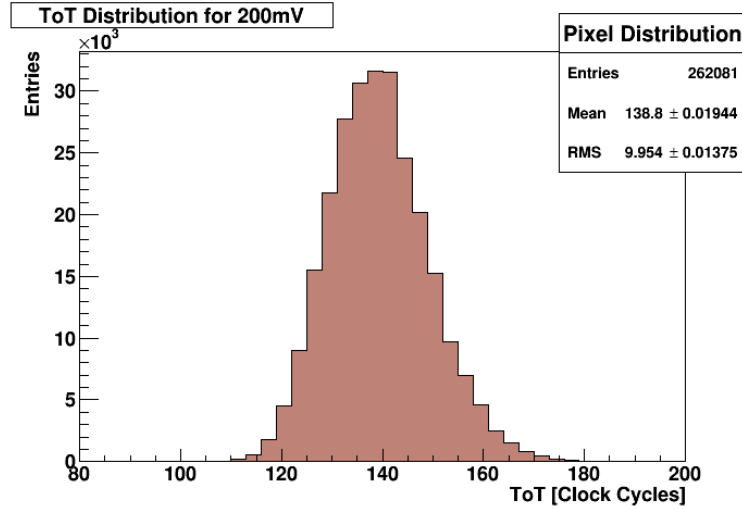


Figure 6.4.: Sample  $ToT$  distribution for a test pulse with 200 mV signal height. The number of entries is equal to  $4 \cdot 256 \cdot 256$ , because for each pulse height the measurement is performed 4 times.

for a voltage of 200 mV is shown in Figure 6.4. Since every measurement is repeated 4 times, the total amount of entries in this histogram is supposed to be  $4 \cdot 256 \cdot 256 = 262,144$ . A complete set of histograms for other voltages can be found inside the Appendix C.2.

From these values the software calculates a mean- $ToT$ -value for every pixel and stores it in a separate file, which leads to the plot shown in Figure 6.5. This plot shows the average  $ToT$  value over all pixels for each voltage. For small input charges the dependency is highly nonlinear. In the second  $x$ -axis on top of the graph, the number of electrons referring to each voltage is calculated. To perform this calculation a 8 fF capacitor  $C_{test}$ , connected in series with the switch to the CSA input, is located in each pixel. Injecting a voltage step  $\Delta U$  to this capacitor creates a well defined amount of charge  $Q_{in}$  inside the capacitor, which can be calculated by the equation 6.1.

$$Q_{in} = C_{test} \cdot \Delta U \quad (6.1)$$

The fit function for this data set is defined by:

$$ToT(\Delta U) = a\Delta U + b - \frac{c}{\Delta U - t} \quad (6.2)$$

where  $a$ ,  $b$ ,  $c$  and  $t$  are free parameters and have to be calculated from of the fit function. The parameters  $a$  and  $b$  describe the linear region of the curve, the parameter  $t$  is connected with the threshold level and the parameter  $c$

## 6.4. Timewalk Compensation

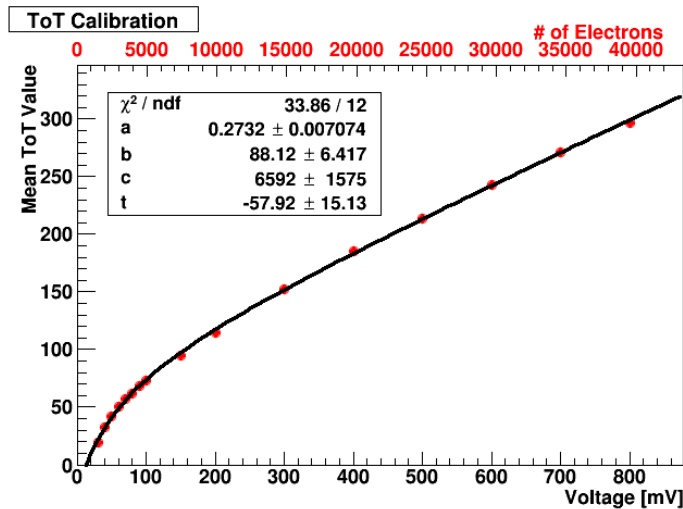


Figure 6.5.: Plot of the average  $ToT$  values from all pixels against the signal height in mV. The second  $x$ -axis is showing the signal height converted into the corresponding number of electrons.

affects the curvature. All parameters must be taken into account for the track reconstruction. Because of the relatively large uncertainty of the fit parameters, it is not recommended to give test pulses with an amplitude less than 30 mV. The values from this fit are used later to convert the measured  $ToT$  values into a charge.

### 6.4 TIMEWALK COMPENSATION

Another effect, that needs to be considered, when doing measurements with a threshold is the timewalk effect. The Figure 6.6 shows two signals, where the peaks are on the same position but have different amplitudes. The signal with the higher amplitude is crossing the threshold level at an earlier time  $T_1$  than the lower signal at  $T_2$ . This time difference leads to the so called timewalk effect, which will give different results in  $ToA$  measurements (e.g. drift time of clusters).

One can expect the time walk effect in all time measurements, when analog pulses with different pulse heights are measured. The time of a signal is constant and the amplitude of the CSA output is proportional to the input charge. Therefore the signal with a higher amplitude is crossing the threshold earlier than the signal with the lower amplitude. In order to compensate the timewalk effect one has to calculate the difference between the two times  $\Delta T = T_2 - T_1$  for each pixel as a function of the input charge.

## 6. CALIBRATION OF TIMEPIX CHIP

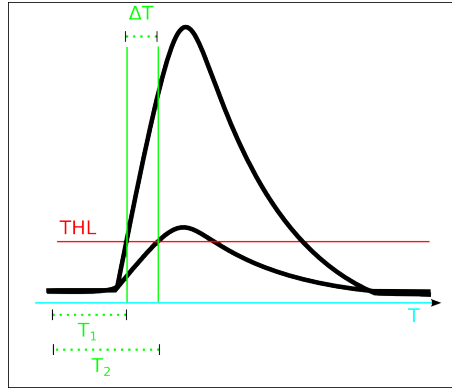
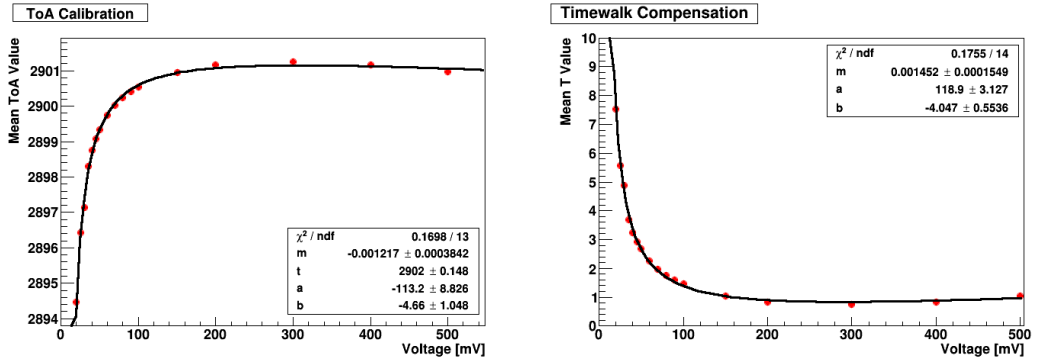


Figure 6.6.: Time difference  $\Delta T$  between two signals with different pulse heights

For the timewalk compensation measurement, the Timepix chip is set to  $ToA$  mode. Test pulses in the same form as for the  $ToT$  calibration are given to the test pulse input of the Timepix chip. The only change is to set all pixels into  $ToA$  instead of  $ToT$  mode. A set of distributions for the different pulse heights are shown in Appendix C.3. The plot with the measured  $ToA$  values against the pulse height can be seen in Figure 6.7(a). The  $ToA$  counts for different test pulse amplitudes are measured at whole four times for each test pulse amplitude.



(a) Measured  $ToA$  values plotted against the signal height in mV

(b) Measured  $ToA$  values with subtracted fit parameter  $t$

Figure 6.7.: Plots of the timewalk compensation.

The fit has been done according to the equation

$$ToA(\Delta U) = m\Delta U + t + \frac{a}{\Delta U + b} \quad (6.3)$$

where  $a$ ,  $b$  and  $c$  are free parameters. In order to calculate the timewalk compensated value  $TtT(\Delta U)$  (Time to threshold, which is equal to  $\Delta T$ ), the fitted value  $t$  has to be subtracted from each ToA value, which leads to the following formula:

$$TtT(\Delta U) = |ToA(\Delta U) - t| \quad (6.4)$$

The final result can be seen in Figure 6.7(b). In the beginning the slope of the graph is very steep until it becomes constant for values above 180 mV.

## 6.5 THRESHOLD OFFSET CALIBRATION

The Threshold offset calibration is needed, because the charge readout is only being done for charge, which is above the threshold level. The amount of charge, which is lower than this threshold, is taken into account as a constant offset. Due to electrical reasons, this amount is not equal for all  $THL$  levels and therefore needs to be measured, in order to define the point, after which the charge measurement takes place.

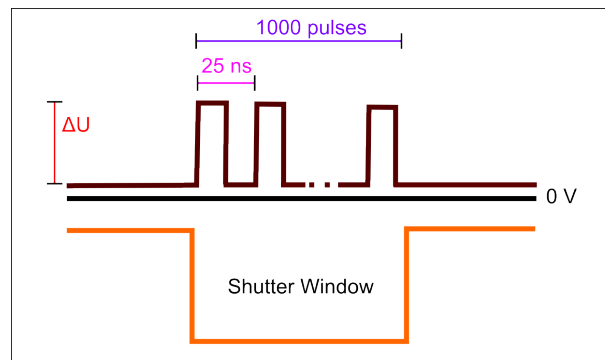


Figure 6.8.: Rectangular pulse shape for the S-Curve calibration. The pulse frequency is 40 MHz and the number of pulses is set to 1000. The signal height  $\Delta U$  is the variable, which has to be changed.

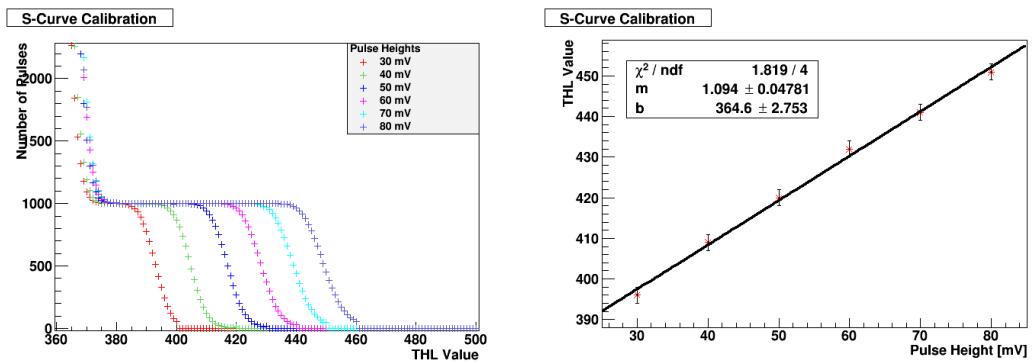
There are mainly two possible methods to determine the threshold offset: the Gaussian shape method and the S-shape method. Since the Gaussian shape method is not tested enough until now and the results are not predictable, the latter method has been chosen for this calibration. The name is derived from the shape of the output plot, which looks like the letter "S". This is the reason, why this threshold offset calibration is also called S-Curve calibration.

The test pulse generator is set to a series of test pulses, which is given to the TimePix chip as shown in Figure 6.8. The software is changing the  $THL$  level

## 6. CALIBRATION OF TIMEPIX CHIP

continuously in discrete steps for each signal height to record the number of measured pulses regarding each  $THL$  value.

The signal height has to be changed manually in the test pulse generator after every run. The pulse period is set to 25 ns in order to make sure, that 1000 pulses can be covered in one shutter window. The effective threshold level has to be calculated by taking the corresponding  $THL$  value at 50% between the plateau of the S-Curve and the  $x$ -axis. With these values one can create a plot with a straight line as the correlation between signal height and the  $THL$  values. This plot is shown in Figure 6.9(b). The fit parameters are therefore the slope  $m$  and the  $y$ -intercept  $b$  according to the equation  $y(x) = mx + b$ .



(a) Measured pulse numbers against the  $THL$  value for different pulse heights

(b) Measured  $THL$  value for the half height of each S-Curve against the pulse height

Figure 6.9.: Plots of the S-Curve calibration.

### 6.6 TIME DELAY COMPENSATION

Due to the fact, that the clock signal is not reaching every pixel at the same time because they are connected in a daisy chain, the result will be a different number of clock cycles for pixels in various areas in the chip. Since there is a time difference between each pixel line of  $\approx 200$  ps, this will result in  $ToA$  and  $ToT$  values, which are too low.

However this effect only has to be taken into account, if almost all pixels in one row are activated. In this case one can observe a gradient between the upper part of the chip and the lower one. The reason for this problem is not fully investigated until now, but it seems to be the result of voltage drop downs in the counting logic during simultaneous operations[Brz13]. It is also mentioned, that for most of the measurements this effect can be neglected.



## CARBON COATED GEMS

---

In the first part of this chapter the method used for creation of thin carbon layers will be described. Another important point is the investigation of the carbon coating by analysing the surface with an electron microscope and X-ray spectrometer in different departments at the University of Siegen. After this the experimental setup of the test chamber will be described and how the calibration of the charge amplifiers has been done. In the following analysis part several properties of the carbon coated GEMs will be investigated to show e.g. their gain stability and spark resistance.

### 7.1 CREATION OF CARBON LAYERS

The carbon layers on the GEMs have been produced by the Fraunhofer Institut für Schicht- und Oberflächentechnik<sup>1</sup>. The method they used is the following: Modified Diamond Like Carbon (DLC) coatings are created by a method, which is called Plasma-Assisted Chemical Vapour Deposition (PACVD). The setup is shown in Figure 7.1. A complete description can be found in [Bew11].

After placing the probe on which the layer should be created, inside a special chamber, an electric field between the probe and the surface of the chamber is created by an electrical power supply, which is connected on one side to the probe and on the other side to the grounded chamber. The voltage is pulsed with a frequency between 30 and 300 kHz while the substrate bias lies between -0.6 and -1 kV.

Due to the electric field free electrons are accelerated and interact with the gas particles and the positively charged particles are deposited on the surface of the probe. First Argon is led into the chamber in order to clean the probe. After this a hydrocarbon gas is used together with other components like e.g. silicon, which leads to a SICAN (see section 5.4.2) surface on the GEMs. It is also possible to combine different layers to a multilayer surface, which contains all properties of every single layer.

---

<sup>1</sup> Contact: Ingmar Bialuch, Bienroder Weg 54e, Braunschweig

## 7. CARBON COATED GEMS

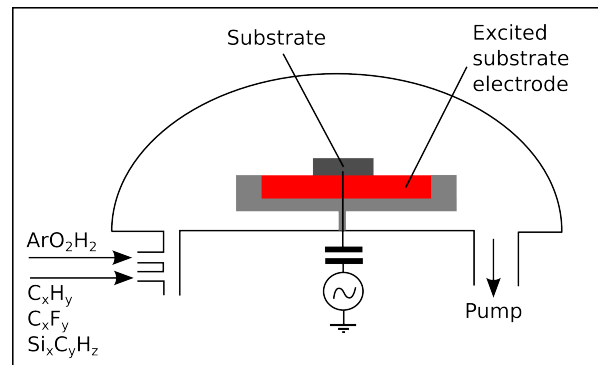


Figure 7.1.: Setup scheme of the chamber for PACVD coating

### 7.2 INVESTIGATION OF CARBON COATING

The carbon coating has been investigated with the help of an electron microscope and a X-ray spectrometer. For the measurement a small probe of the **GEM** was necessary. The comparison between a coated and uncoated **GEM** is presented in Figure 7.2. The investigation has been done in the research groups *Surface and Materials Technology* [Lot14] and *Institute for High Frequency and Quantum Electronics* [Hqe14] at the University of Siegen. The used microscope was a Transmission Electron Microscope (TEM) of the type HITACHI H-8100 in combination with a EDAX DX4 X-ray analyser. The maximum acceleration voltage is 200 kV with a highest reachable magnification of  $10^6$ .

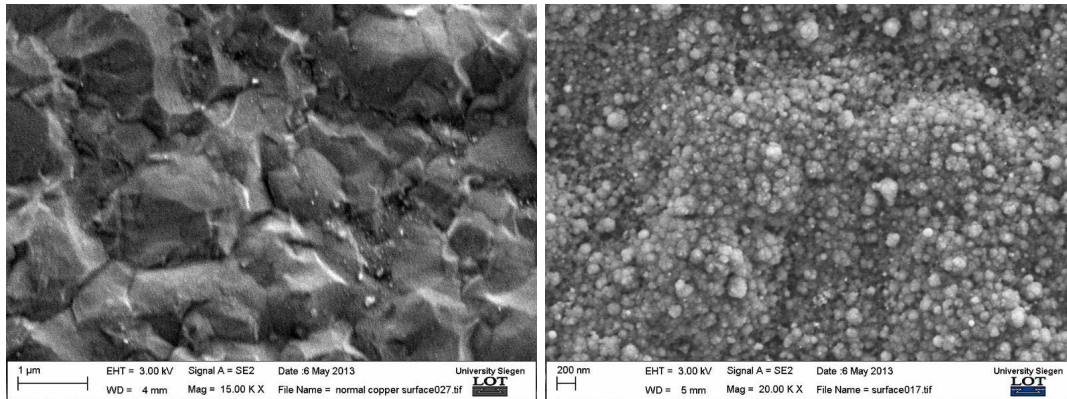
The Thermo NORAN NSS 302 is a spectrometer for measuring the chemical elements inside a probe with its characteristic  $K_\alpha$  line by sending high energetic X-rays to the surface probe. The energy resolution of this system is 130 eV and the detection limit lies between 1000 and 3000 ppm<sup>2</sup>. The element with the smallest element number, which can be measured with this device, is Beryllium.

The X-ray analysis was done for an uncoated and a carbon coated **GEM**, which one can see in Figure 7.2. In the Figures 7.2(a) and 7.2(b) one can see the comparisons between the SICON coated and the uncoated surface. The coating thickness was intended to be  $0.1 \mu\text{m}$ . In these pictures it is clear to see, that the thickness of the carbon layer is not constant and varies throughout the **GEM** surface. As expected, the uncoated **GEM** shows in Figure 7.2(c) only one peak for copper, since there is no other material involved in the case of the uncoated **GEMs**. For the coated **GEMs** Figure 7.2(d) shows additionally

---

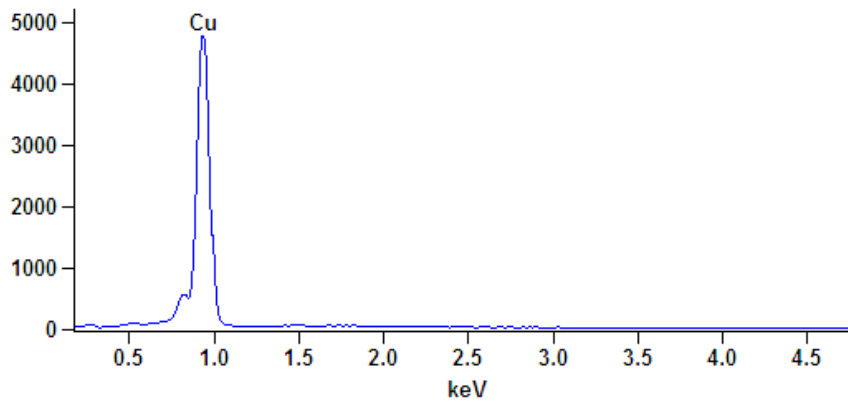
<sup>2</sup> Parts per Million (ppm)

## 7.2. Investigation of Carbon Coating

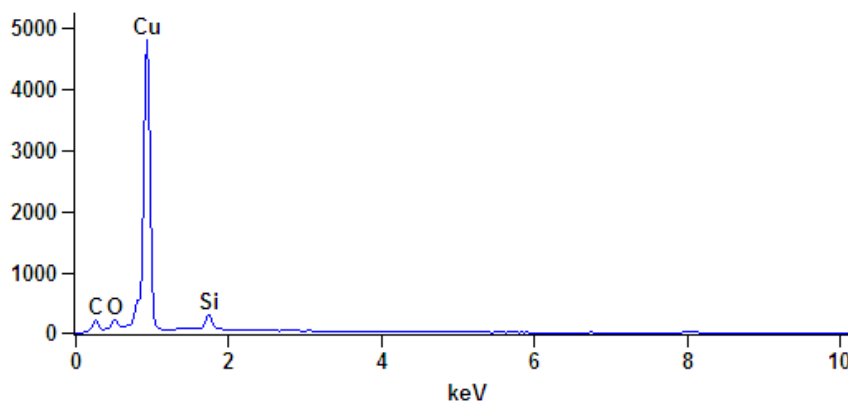


(a) Surface of a uncoated GEM

(b) Surface of a SICON coated GEM



(c) Mass spectrometer analysis of an GEM without coating



(d) Mass spectrometer analysis of an GEM with SICON coating

Figure 7.2.: The comparison of the surface of a coated and an uncoated GEM with an electron microscope and a mass spectrometer.

## 7. CARBON COATED GEMS

one peak for carbon, one for silicon and one for oxygen as expected from the structure of SICON.

An interesting question is, if the coating also penetrates the holes in the GEMs. In the same way the investigation of the carbon layer inside the GEM holes has been done. The referring Figures are shown in Appendix F.4. This is necessary to prove the conducting property of the carbon coating in order to avoid the charging up effect inside the GEM holes. In this case there is no peak for copper since the interior of the holes only consists of Kapton. Additionally there is one peak for nitrogen, which is a part of the Kapton structure as one can see in Figure 7.3.

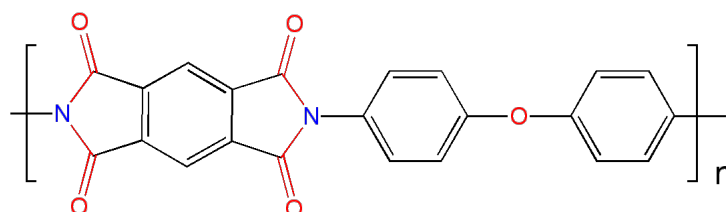


Figure 7.3.: Chemical structure of Kapton

It is also possible to observe an increase of the carbon and oxygen peak since these two elements are included with a high amount inside the Kapton structure. The prove for the carbon coating can be done with the help of the silicon peak, because this peak can only come from the SICON carbon layer and not from the Kapton, while nitrogen, carbon and oxygen exist in both materials. The analysis of the thickness leads to the Figure 7.4. Unfortunately it was not possible to determine the exact thickness of the carbon layer, because of its uneven structure and thinness.

### 7.3 EXPERIMENTAL SETUP

The first testing of the Carbon Coated GEMs has been done inside the test chamber. The parameters for the setup using one single GEM are summarised in Table 7.1. For inserting two GEMs the setup is changed according to the Table 7.2. The induction field has been reduced from 300 V/mm to 200 V/mm since otherwise the output voltages of the power supplies would exceed their limitations of 2 kV.

## 7.4. Pad Readout Calibration of Test Chamber

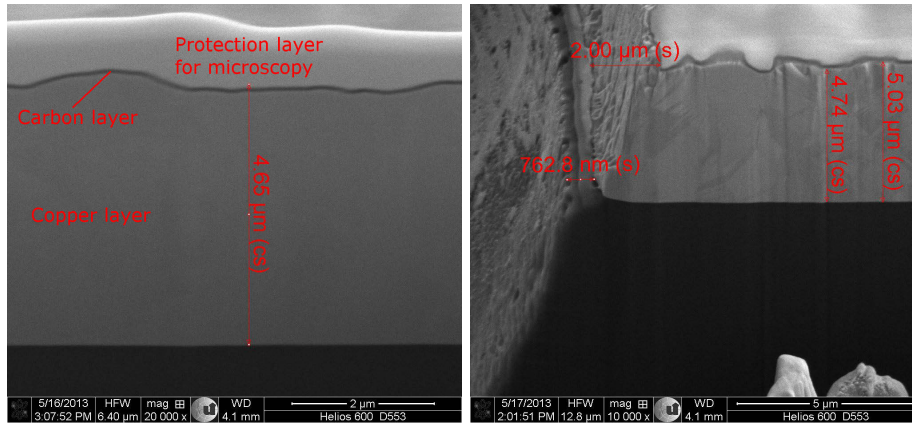


Figure 7.4.: Analysis of the thickness of the carbon coating on top of the copper layers  
The copper shows a thickness of  $4.65 \mu\text{m}$  in the left picture, which is near to the expected value of  $5 \mu\text{m}$ . In the right picture one can see, that the carbon thickness is not constant over the whole surface.

Active GEM area	$50 \times 50 \text{ mm}^2$
Gas mixture	ArCO <sub>2</sub> 80:20
Drift field	50 V/mm
Induction field	300 V/mm
GEM voltage	variable
Drift length	5.4 mm
Distance Pads – GEM	2.4 mm
Ionization source	Fe-55 (without collimator)

Table 7.1.: Experimental setup for the testing one carbon coated GEM

### 7.4 PAD READOUT CALIBRATION OF TEST CHAMBER

In order to measure the gas amplification from the charge, which is created by a single photon from the  $^{55}\text{Fe}$  source, it is necessary to make a calibration of the complete setup. For this purpose a pulse generator is connected via a 1 pF capacitor to the input of the charge sensitive amplifier, which converts the deposited charge into a voltage signal. Due to the size of this capacitor a voltage signal of 1 mV leads to a charge of 1 fC according to the formula  $Q = CU$ .

## 7. CARBON COATED GEMS

Active GEM area	$50 \times 50 \text{ mm}^2$
Gas mixture	ArCO <sub>2</sub> 80:20
Drift field	50 V/mm
Transfer field	200 V/mm
Induction field	200 V/mm
GEM voltages	variable
Drift length	5.4 mm
Distance between GEMs	2.2 mm
Distance Pads – GEM	2.4 mm
Ionization source	Fe-55 (without collimator)

Table 7.2.: Experimental setup for testing a stack of two carbon coated GEMs

In order to make it possible to measure the signal with the MCA, it must be shaped to a gaussian signal with a width of at least  $1 \mu\text{s}$ . This is done by the following shaping amplifier, which is directly connected to a MCA. A scheme of the calibration setup is shown in Figure 7.5.

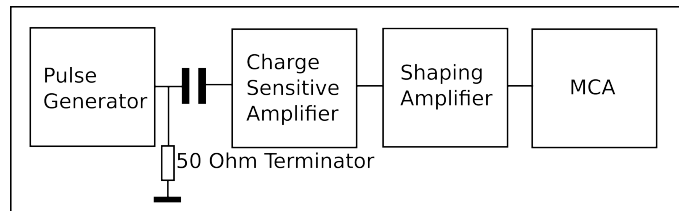


Figure 7.5.: Electrical circuit of the calibration setup

A screenshot from the oscilloscope can be seen in Figure 7.6. The red signal in the middle shows the voltage signal, which is given by the test pulser to the input of the charge amplifier. The upper green signal displays the signal, which is coming from the output of this amplifier and given to the input of the shaping amplifier.

The lower blue signal shows the signal from the shaping amplifier. In this signal one can see two peaks from which the second one has to be neglected, because in this case it is a overshoot and has no physical meaning. One can see both peaks in the spectrum of the MCA and just ignore the one with lower channel numbers. In Appendix C.1 all histograms of the MCA for different input voltages are presented for channel 6, which is connected to the pad with

## 7.4. Pad Readout Calibration of Test Chamber

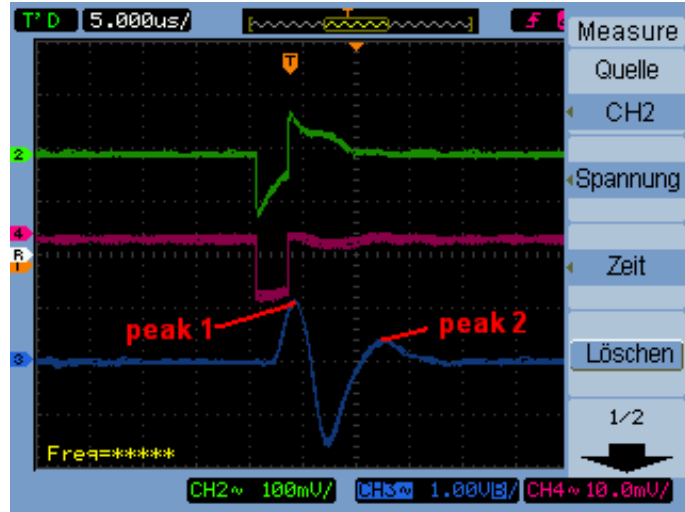


Figure 7.6.: Screenshot of the oscilloscope with all relevant signals for the calibration

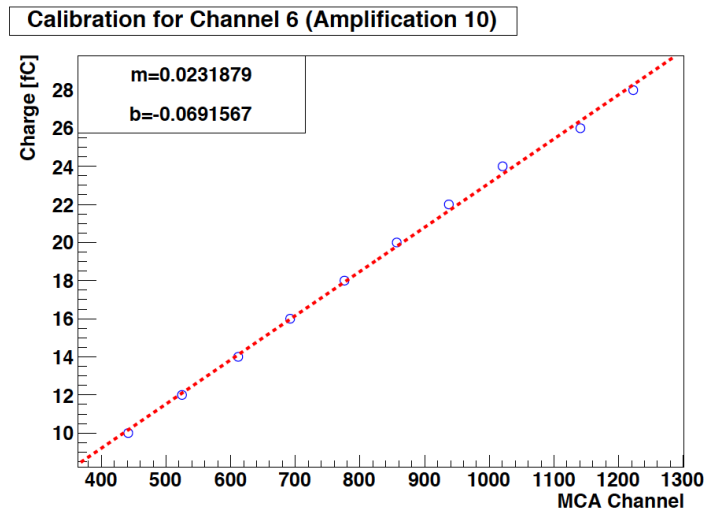


Figure 7.7.: Linear fit for the plot of charge against MCA channel numbers

## 7. CARBON COATED GEMS

the number 26 and also used for the later measurements. In these plots only the relevant peak is shown. By changing the amplitude of the test pulse in the range between 11 mV and 28 mV the signal height is increasing to higher channel numbers.

Fitting a gauss function to the measurement peak gives the value of its maximum, in order to plot it against the signal charge, which is shown in Figure 7.7. Fitting a straight line through the measurement points leads to the following calibration equation:

$$y(x) = [(0.0232 \pm 0.0003) \cdot x - (0.1 \pm 0.3)]\text{fC} \quad (7.1)$$

where  $x$  is the channel number of the MCA and  $y$  the charge.

### 7.5 MEASUREMENT OF GEM BEHAVIOURS

For the first measurement one SICAN GEM has been tested with different gas mixing ratios of ArCO<sub>2</sub>. The following ratios have been investigated: 60:40, 70:30, 80:20 and 90:10. Figure 7.8 shows the final results of the gain against GEM voltage. One can see, that with a higher amount of quencher less amplification can be achieved.

In order to compare the behaviours of the different GEMs, they have been tested separately inside the test chamber. The electric field between their surfaces has been increased in discrete steps until the first spark could be detected. The referring plot can be seen in Figure 7.9. This plot also shows, that the amplification for SICAN coated GEMs is higher than for SICON coated ones for the same GEM voltage and nearly the same as for uncoated GEMs. It has been therefore decided to continue further measurements inside the TPC prototype with SICAN coated GEMs. More graphs are presented in Appendix F.2.

From this plot one can see, that with a single SICAN GEM inside a TPC it is possible to achieve gas amplifications, which are up to a factor four higher than for uncoated GEMs, if a complete absence of sparks is necessary. The reason for this is, that for the carbon coated GEMs sparks appear at much higher voltages than for uncoated ones. However for more than one GEM inside a stack, the achievable GEM voltage is much lower since the sparks are then created due to the uncontrolled electron avalanches inside the GEMs.

Figure 7.10 shows the behaviour of two GEMs in a serial stack. As expected the spark probability is higher than for one single SICON coated GEM. Therefore it is even with SICAN coated GEMs not possible to increase the voltage above 420 V before getting first sparks. Although it is not possible to test a stack of three GEMs inside the test chamber because of its size, a faster spark production at lower voltages is expected.



7.5. Measurement of GEM Behaviours

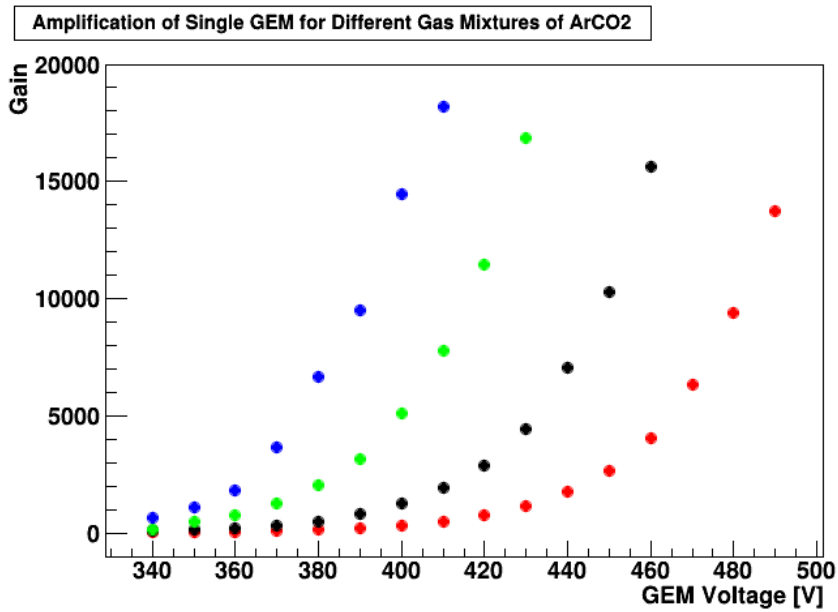


Figure 7.8.: Gas gain of a single SICAN GEM for different mixing ratios: 90:10 (blue), 80:20 (green), 70:30 (black), 60:40 (red).

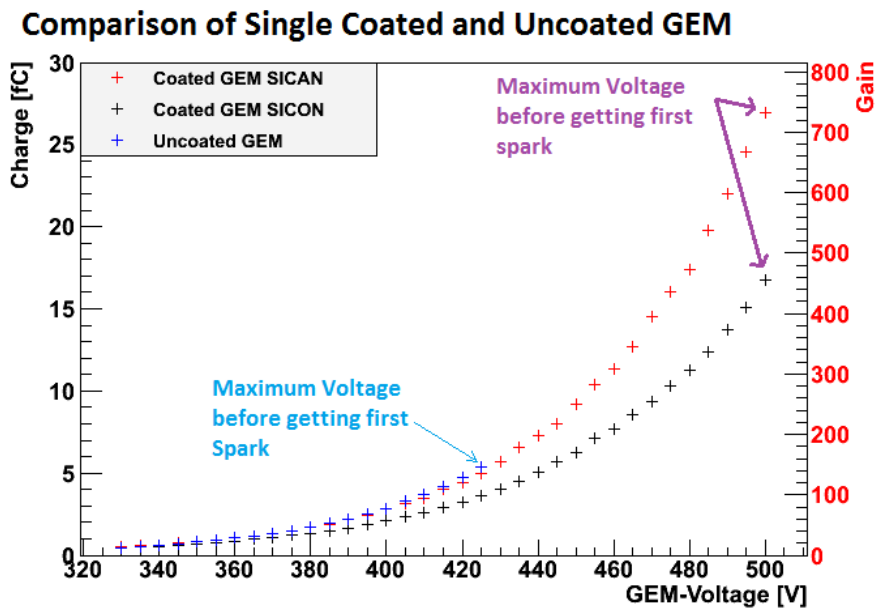


Figure 7.9.: Comparison of GEMs with coated and uncoated surfaces

7. CARBON COATED GEMS

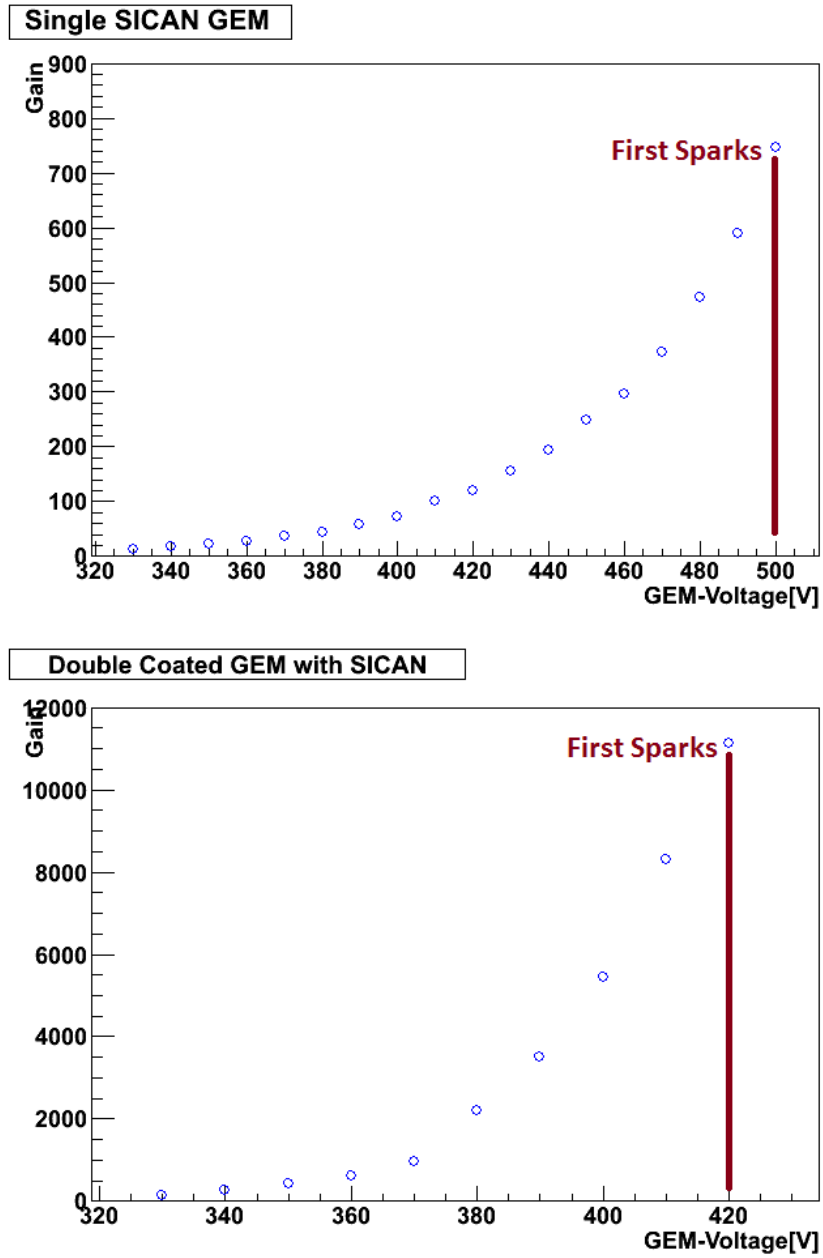
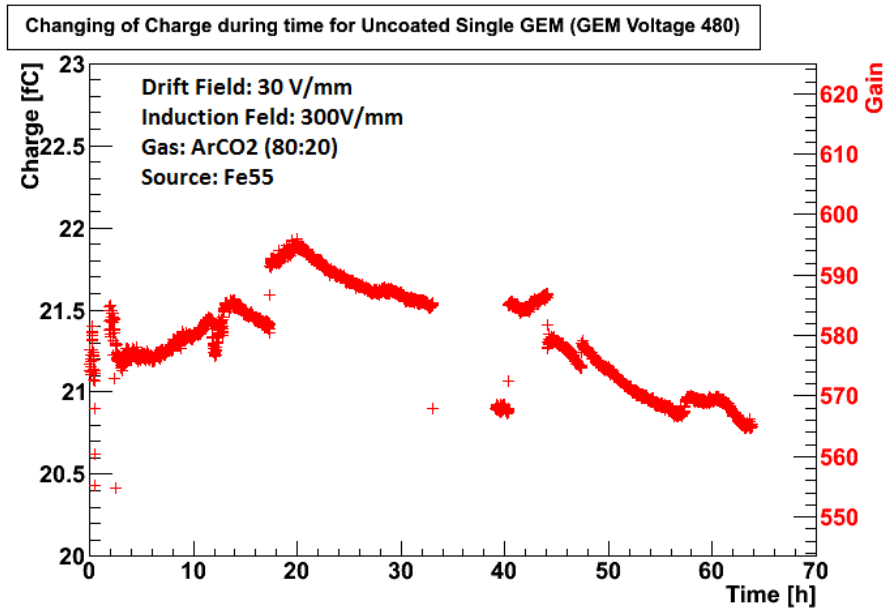
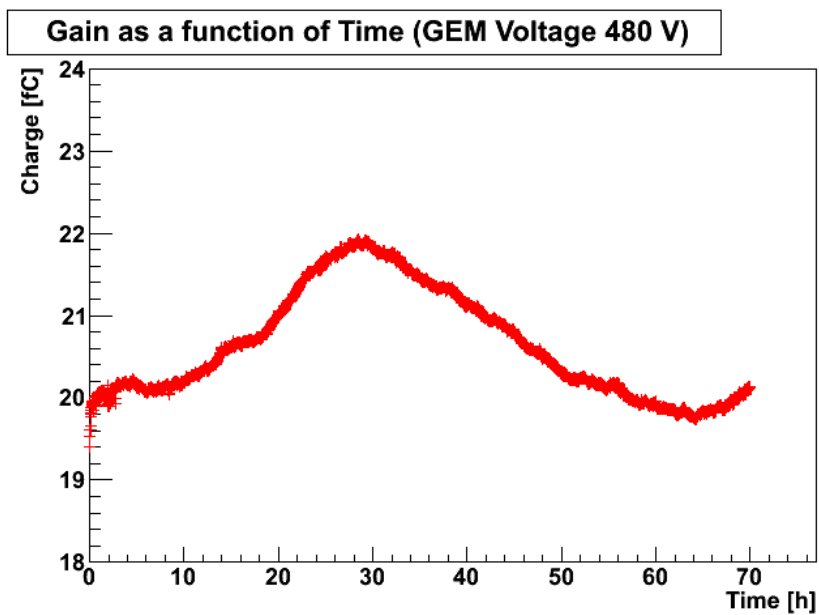


Figure 7.10.: Gain of one single SICAN GEM (up) and two carbon coated GEMs in a stack (down)

## 7.5. Measurement of GEM Behaviours



(a) Gain stability of a single uncoated GEM



(b) Gain stability of a single SICAN GEM

Figure 7.11.: Comparison of gain stabilities for SICON and SICAN coated GEMs. In case of the uncoated GEM the gain drops to almost 0 every time, when a discharge take place. For the SICAN coated GEM this behaviour is not observed for the same GEM voltage. The slight change of the gain in both cases is related to the change of the temperature and pressure during the measurement.

## 7. CARBON COATED GEMS

In order to compare the long time stability of a carbon coated GEM with an uncoated one, the gas amplification has been measured for approx. 70 hours. The result of this comparison is shown in Figure 7.11. In both cases the the GEM voltage was set to 480 V.

The shape of the graph is almost the same for both GEMs, but the most important result is the fact, that in case of the uncoated GEM the gain drops down very often to almost 0, because of several discharges inside these 70 h. Every time, when a discharge takes place, the voltage of the power supplies reaches a local minimum for a short period of time, in which there is almost no gas amplification. After this the GEM normally needs some time to reach back to the previous amplification.

Another effect is the charging up effect of the plastic layer inside the GEM. This also changes the electric field inside the whole and has therefore a big influence on the gain.

For the measurement of the GEM resistivity the setup has been changed to the one presented in Figure 7.12. The used current-to-voltage-converter converts the current through the GEMs into a voltage with the ratio  $1 \text{ nA} \rightarrow 1 \text{ V}$ .

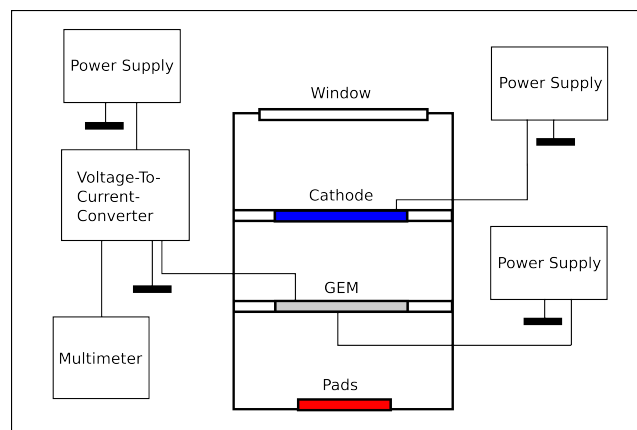


Figure 7.12.: Setup for determining the resistivity of a carbon coated GEM by measuring the current on the upper side with a current-to-voltage-converter

The output voltage can be seen on a standard multimeter, which can also be connected to a PC in order to record a long time measurement. The current limit, which can be measured, is approx. 9 nA because of the 9 V power supply battery for the converter. The results of the measurement are shown in Figure 7.13.

One can see from this plot, that the current for SICON coated GEMs is always higher than for the SICON coated one, i.e. the resistance is smaller over the whole time. Similar measurements can be found in [Bew11]. The only

## 7.6. Long Time Measurements of Gain Stability

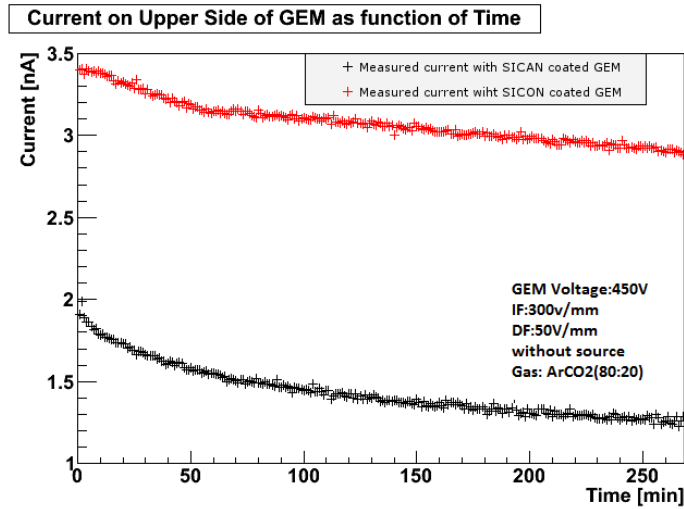


Figure 7.13.: Comparison of currents for two different GEM coatings SICON and SICAN without using  $\gamma$  source. The resistance is inversely proportional to the current.

difference is, that the self cleaning effect, which is also described in this paper, cannot be observed. A higher current, like in the case of SICON, leads to a lower gain because of the decrease in the electric field between both GEM sides.

### 7.6 LONG TIME MEASUREMENTS OF GAIN STABILITY

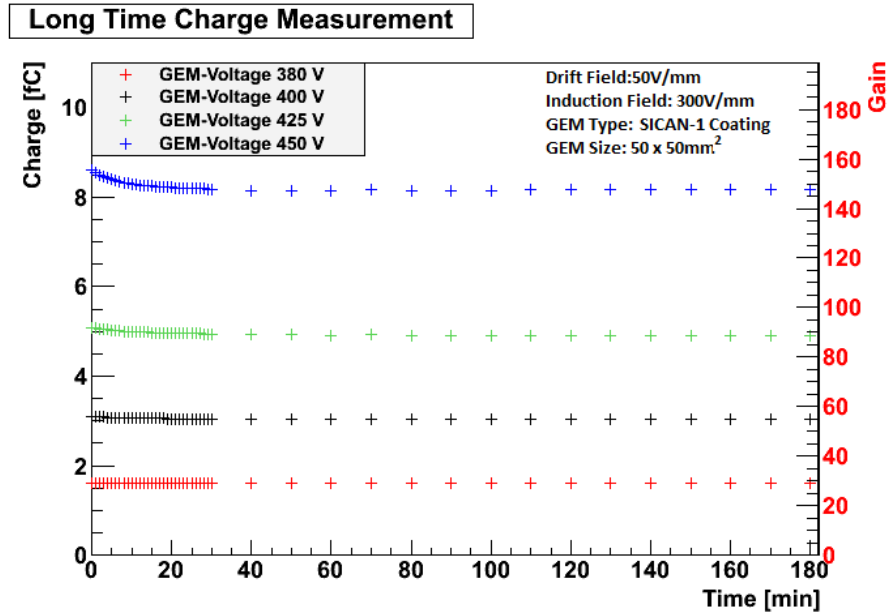
For both coatings SICON and SICAN the gain stability over the time has been measured for 3 h. Figure 7.14 shows the result, where the amplification of SICON is less compared to SICAN for the same voltage as expected from the results of previous measurements. One can see very clearly, that the higher the applied GEM voltage, the longer it needs until the gain becomes stable. The investigation of the long time stability is important, since the data is normally taken for several days or weeks and it is very important to know about the properties of the GEMs for these long time measurements.

In order to quantify the changing of the gain, it is possible to make a fit through the data points. The following fit function for the gain is assumed, which shows good results for the tested data:

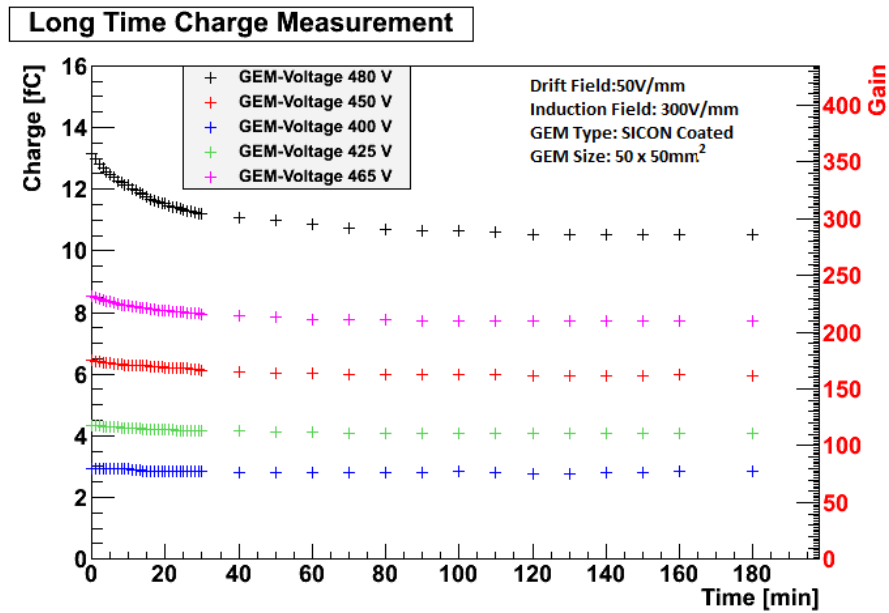
$$G(t) = Ae^{-\mu t} + B \quad (7.2)$$

The parameter  $B$  gives the asymptotically gain for  $t \rightarrow \infty$ , while  $A + B$  can be interpreted as the starting point of the gain at  $t = 0$ .  $\mu = 1/\tau$  is the decreasing constant, while  $\tau$  is the value after which the gain falls to  $1/e$  of the value of

7. CARBON COATED GEMS



(a) Gain stability of a single SICAN GEM



(b) Gain stability of a single SICON GEM

Figure 7.14.: Comparison of gain stabilities for SICON and SICAN coated GEMs. In case of SICON the gain reaches its equilibrium position much quicker compared to SICAN for the same GEM voltage.

## 7.6. Long Time Measurements of Gain Stability

the starting point. It is correlated to the half-life of the gain according to the following formula:

$$T_{1/2} = \frac{\ln 2}{\mu} \quad (7.3)$$

In this case  $t + T_{1/2}$  stands for the time, after which the gain decreases to half of its value at the time  $t$ .

Figure 7.15 shows two plots with the applied fit function for SICON and SICAN coated GEMs. From the values of the decreasing constant  $\mu$  one can see, that the gain for SICAN coated GEMs becomes quicker stable compared to SICON coated ones.

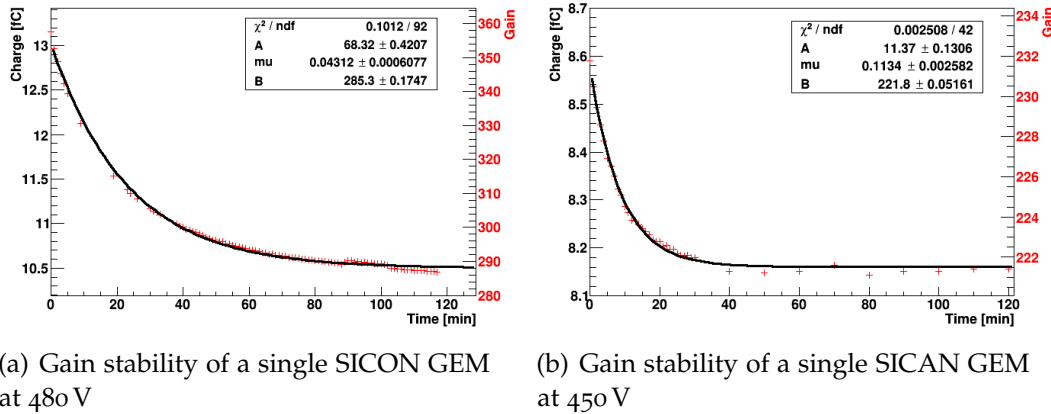


Figure 7.15.: Fit through the gain stabilities for SICON and SICAN coated GEMs. The gain for the SICAN GEMs decreases quicker to the asymptotic value for  $t \rightarrow \infty$  compared to the SICON ones.

Figure 7.16 shows the changing of the outside temperature and pressure during the time and in comparison the changing of the gas amplification for coated and uncoated GEMs. For uncoated GEMs the atmospheric effect is much better to see compared to the coated ones. One can also observe a 24 h periodicity, in which the measured gain reaches a maximum always after the same time interval.

Since air can be seen in general as an ideal gas, the following gas equation can be used:

$$pV = Nk_B T \quad (7.4)$$

where  $p$ ,  $V$  and  $T$  are the gas pressure, volume and temperature.  $N$  represents the number of gas particles and  $k_B$  is the so called Boltzmann constant. In case of the TPC the gas volume  $V$  is constant, i.e. the fraction  $p/T$  is directly proportional to the number  $N$  of particles.

## 7. CARBON COATED GEMS

By plotting the values of  $p/T$  against the gain, as one can see in Figure 7.17(a) for coated GEMs and 7.17(b) for uncoated ones, the result leads to a straight line with a negative falling slope, because the number of created electron-ions-pairs inside the GEMs is proportional to the number of particles inside the gas volume. In both cases the GEM voltage was set to a value of 450 V. However for carbon coated GEMs the result looks clearer than for uncoated GEMs. Two plots, that are showing the direct correlation between gas gain and temperature resp. pressure, can be found in Appendix F.1.



## 7.6. Long Time Measurements of Gain Stability

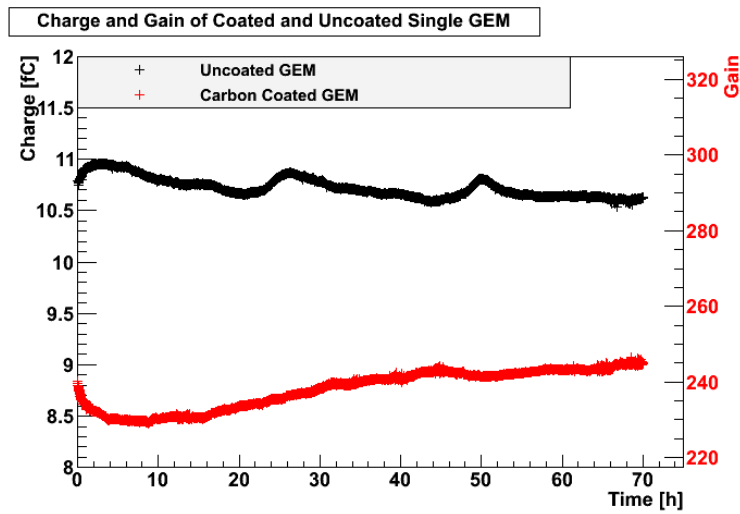
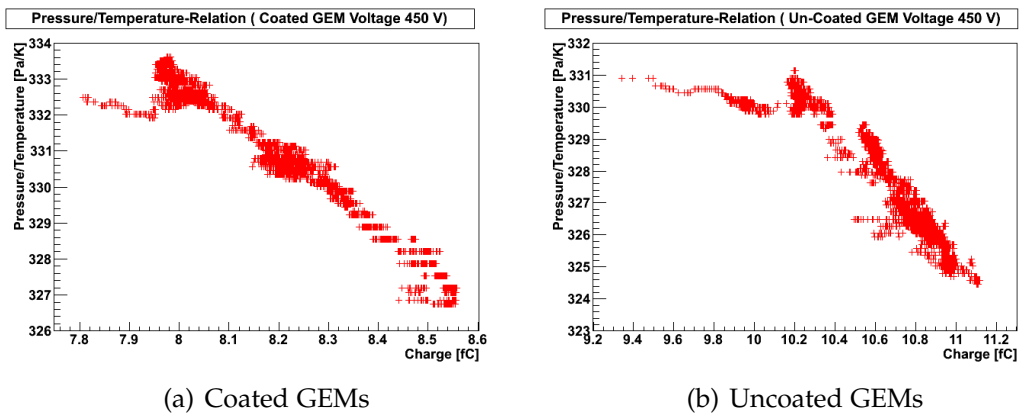


Figure 7.16.: Comparison of changing of gain during time for coated and uncoated GEMs. In the graph of the uncoated GEMs one can see the atmospheric effects due to changing of temperature and pressure very clearly.



(a) Coated GEMs

(b) Uncoated GEMs

Figure 7.17.: Correlation between atmospheric fluctuations and measured charge of coated and uncoated GEMs. First the coated GEM and then the uncoated GEM has been measured. The changed temperature and pressure can have a slight effect on the results as one can also see in the periodic gain changing of the uncoated GEM.



## DATA WITH TPC PROTOTYPE

This chapter describes the data taken with the Timepix chip and the TPC prototype. Two different readout systems were used and will be described in the following sections. Later the analysis of the taken data will be presented in detail.

### 8.1 CALIBRATION WITH USB DEVICE

The first data with the Timepix chip was taken using the USB device (see section 5.5.2). Before starting the calibration process with the USB device a threshold equalisation has been performed. The result recorded with Pixelman is presented in Figure 8.1. The measured mean value is 336.

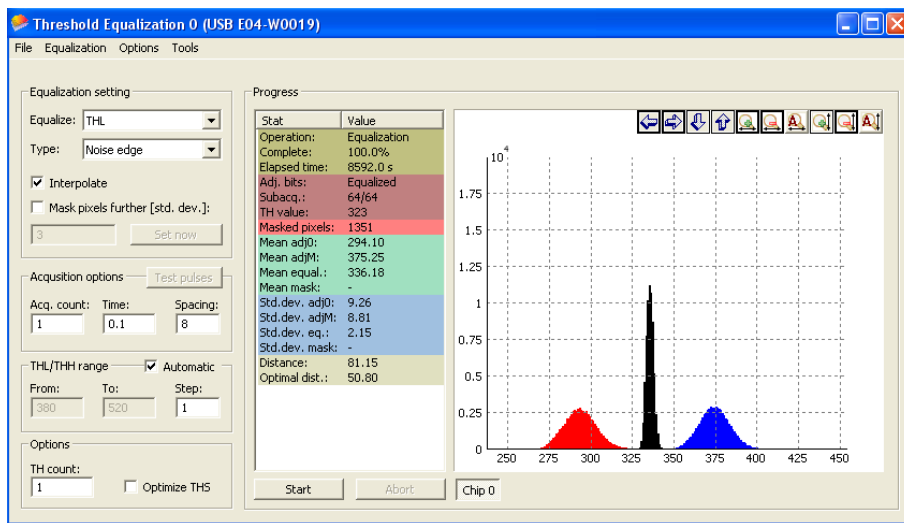
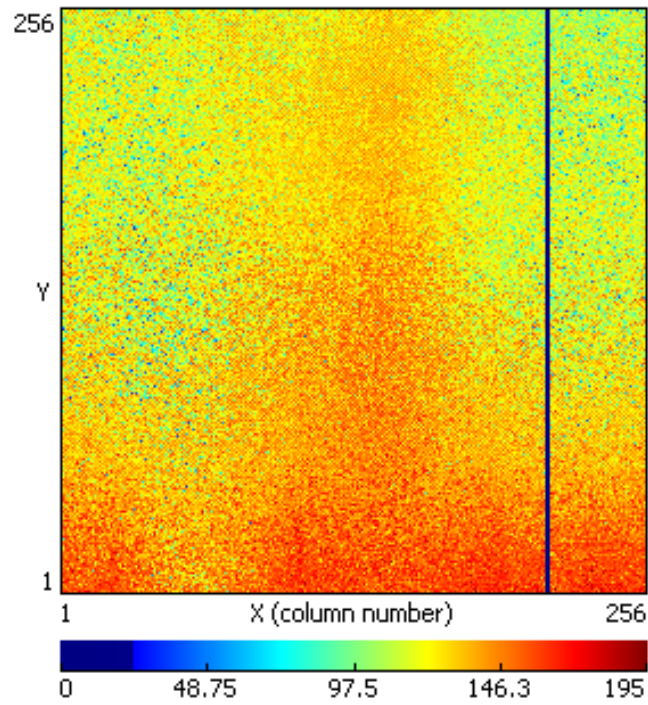


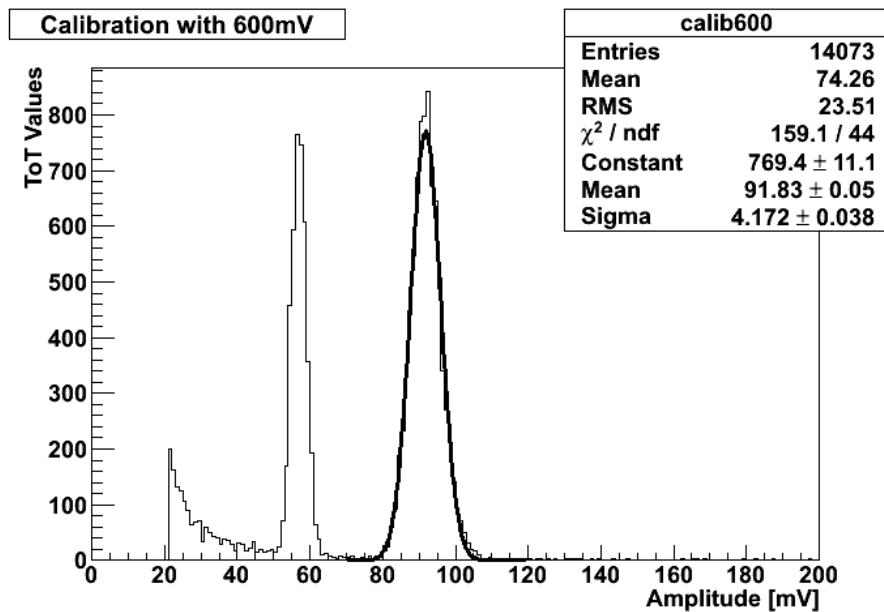
Figure 8.1.: Threshold equalisation done by the Pixelman software. The mean value is shown is 336. The three peaks are explained are section 6.2

The next step was the adjusting of test pulses in order to do the calibration of the Timepix chip. A sample calibration frame and a  $ToT$  distribution measured with the USB device in combination with the Pixelman software can be seen in Figure 8.2. In principle there should be only one peak in the  $ToT$  distribution shifting with the changing of the test pulse voltage. Due to some reasons, which could not be fully investigated, other values without physical meanings

## 8. DATA WITH TPC PROTOTYPE



(a)



(b)

Figure 8.2.: Sample calibration frame and distribution with the USB device and Pixelman software. The blue vertical line inside the pixel matrix indicates a damaged pixel column. Figure (a) shows the pixel matrix for a sample calibration measurement in  $ToT$  mode for a test pulse of 600 mV, while Figure (b) presents the referring  $ToT$  distribution for the same pattern.

also appear. This is already a first indication for problems regarding the calibration with the USB device.

Another problem, which occurred, was the fact, that some captured calibration frames showed a strange behaviour like overflow in the whole pixel matrix. Sometimes some pixel columns were also empty and it seemed, that they did not get the right amount of charge. A reproduction of the same measurements was also not successful, since the  $ToT$  values always differed between every calibration. Some of these problems and further investigations on the calibration problems can be found in [Koh10].

At the end of the calibration it has been concluded, that the expected results of the calibration could not be measured. This gives the motivation to use another readout system in order to record the data from the TPC prototype. Since the MUROS device [Nik14] was not used any longer and a new readout system with the Virtex 6 FPGA card was proposed, it was decided to use this system for further data taking. As the development of this readout device required some time, it seemed to be beneficial to take some test data with the USB device, in order to check the functionality of the TPC prototype.

## 8.2 DATA WITH USB DEVICE

As explained in section 8.1, the data taken with the USB device is not calibrated. The variation between the pixels is in the order of a few percent, so that some measurements were possible.

### 8.2.1 Laser Measurements

The first test data has been taken with the UV laser in combination with the TPC prototype, because in opposite to other ionisation sources the used laser can be set to specific repetition times, which makes every measurement exactly reproducible. The used gas mixture was Argon-CO<sub>2</sub> with a mixing ratio of 80:20. Table 8.1 gives a complete list of the parameters, which have been set to measure the test data.

Figure 8.3 shows the positions of the laser. Due to the large diffusion for long drift distances the third entry hole has not been used. The amplification has been done with a stack of three uncoated GEMs from CERN as described in section 4.3.3. The active area of these GEMs is 100 mm × 100 mm. The pixel chip was placed in the center of the end plate, in order to make sure, that the laser signal passes the active area of the chip.

For the laser repetition rate of 1 Hz a photo diode has been placed at the exit window of the laser beam to use it as a signal output for the trigger system.

## 8. DATA WITH TPC PROTOTYPE

Gas mixture:	Argon-CO <sub>2</sub> 80:20
GEM voltages:	390
Drift field:	9.8 V/mm
Induction field:	250 V/mm
Transfer field 1:	200 V/mm
Transfer field 2:	200 V/mm
Outside temperature:	22°C
Pressure:	Normal atmospheric pressure
Distance Timepix chip – GEM 1:	2.5 mm
Distance GEM 1 – GEM 2:	2.5 mm
Distance GEM 2 – GEM 3:	2.5 mm
Drift distance from 1st hole:	94 mm
Drift distance from 2nd hole:	196 mm
Laser frequencies:	1 . . . 2500 Hz
Clock frequency:	10 MHz
Shutter window for first hole:	26 $\mu$ s
Shutter window for second hole:	36 $\mu$ s

Table 8.1.: Parameters of the test measurement with the TPC prototype for the USB device

Figure 8.4(a) shows a recorded frame for the laser beam for the first entry hole and 8.4(b) for the second one. The diffusion for the second hole is clearly visible.

Measurements with different laser repetition rates have been done (1 Hz, 100 Hz and 500 Hz) as shown in Figure 8.5. The distributions of the laser signals were created by summing up all *ToT* values in one pixel column and plotting the average value against each pixel row. The first and last 15 columns have been cut in order to avoid the disturbances at the edges of the Timepix chip. The referring distributions show, that the position of the center of the laser beam is slightly shifting as a function of the frequency. This seems to be an effect of the optical structure inside the laser, but has to be investigated in further studies.

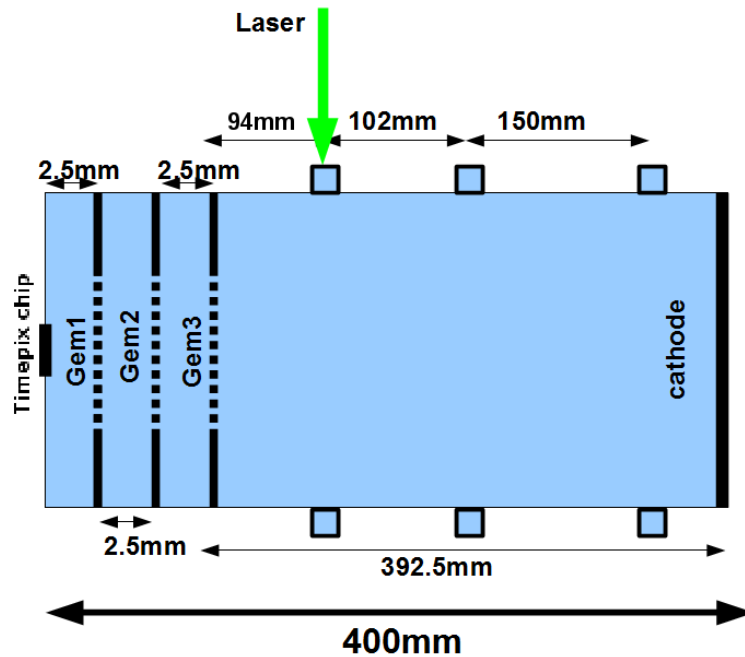


Figure 8.3.: Sketch of the three different entry and exit holes for the laser beam. The green arrow on the upper side displays the direction of the laser beam. The first window is defined as window with the closest distance to the first GEM.

### 8.2.2 Source Measurements

For the prove of the correlation between the photon energy and gas ionisation a data set has been taken with the  $\gamma$ -sources Molybden and Rubidium and a  $\beta$ -ray source ( $^{90}\text{Sr}$ ). Example frames using the  $\gamma$  source taken with the Timepix chip are shown in Figure 8.6. As one expects there are only single clusters for the  $\gamma$  source because of the discrete energy loss of the photons due to the photo effect. From the size of the cluster and the  $ToT$  entries one can see, that the deposited charge for Molybden is higher than for Rubidium, which can be seen by summing up all  $ToT$  values from one frame. The histograms show further the expected Landau distribution very clearly. According to [Aou13] this is the typical distribution for charge deposition inside a semiconducting pixel sensor.

The beam of the  $\beta$ -ray-source is tilted according to the beam angle of the source. Additionally the Timepix chip was tilted by an angle of  $90^\circ$ . The tracks of the  $\beta$ -ray-source can be seen in Figure 8.7. For the  $^{90}\text{Sr}$  source a PMT with a scintillator material in front has been used to create a trigger signal for the chip. Because of this reason, the shutter length has been set to  $35 \mu\text{s}$  for the

## 8. DATA WITH TPC PROTOTYPE

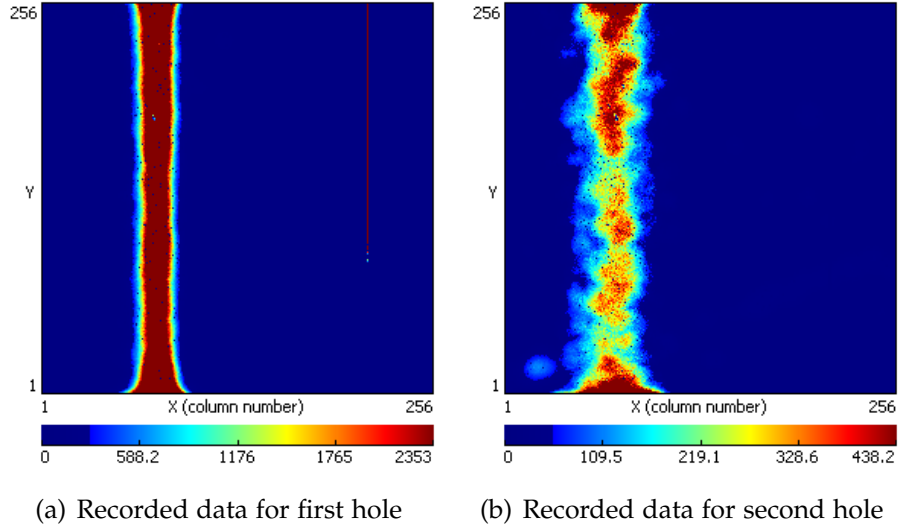


Figure 8.4.: Recorded laser signal for different distances between the laser beam and the GEMs. In this plots the signal has a vertical direction, because the chip is tilted by an angel of  $90^\circ$ . The frequency of the laser pulses was set to 1000 Hz.

first entry hole, which is long enough for the drifting electrons to reach the Timepix chip according to the drift velocity of the used gas mixture.

### 8.3 DATA TAKING WITH VIRTEX 6 READOUT SYSTEM

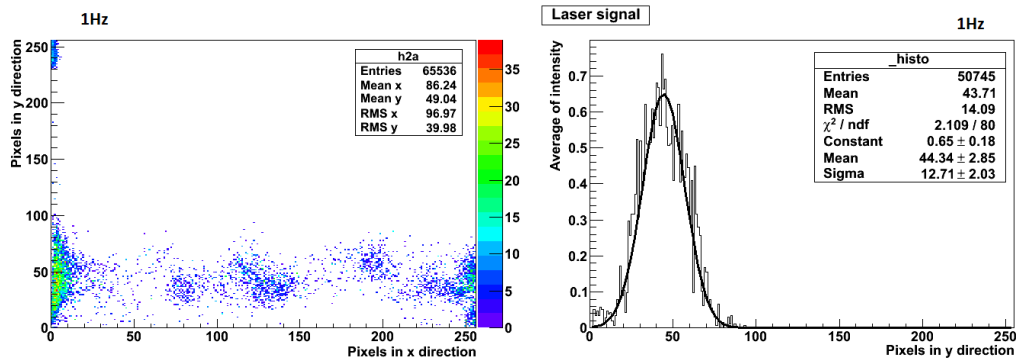
After showing, that electrons can be detected with the Timepix chip using the USB device for the readout, more quantitative measurements are performed with the Virtex 6 readout. During the data taking with the USB device this readout system and its firmware have been developed to a state, in which it is possible to perform calibration and take measurement.

#### 8.3.1 Measurement of the Drift Velocity

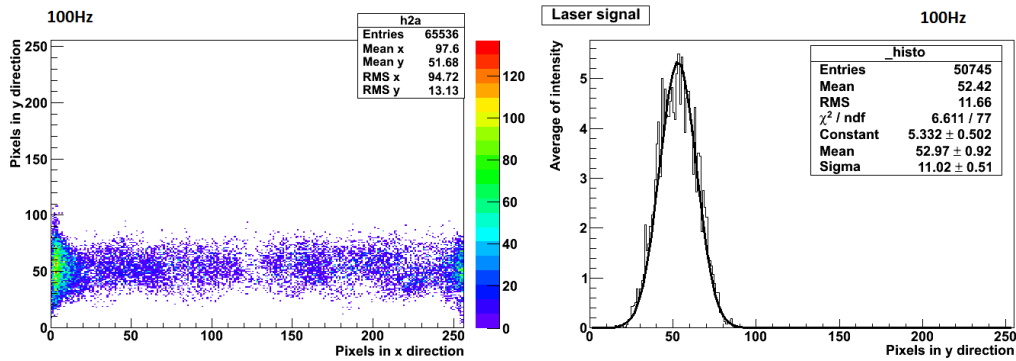
The theoretical value of the drift velocity  $v_{\text{drift}}$  can be calculated with the help of the program **Magboltz** [Bia11], which uses a Monte-Carlo algorithm to determine the scattering of the electrons inside given gas mixtures by solving the Boltzmann transfer equations numerically and taking the cross sections for electron scattering into account. The value for ArCO<sub>2</sub> with the mixing ratio of 80:20 is calculated by this program to  $v_{\text{drift}} = 5.128 \text{ mm}/\mu\text{s}$  and for a ratio of 90:10 it gives  $v_{\text{drift}} = 9.965 \text{ mm}/\mu\text{s}$ .



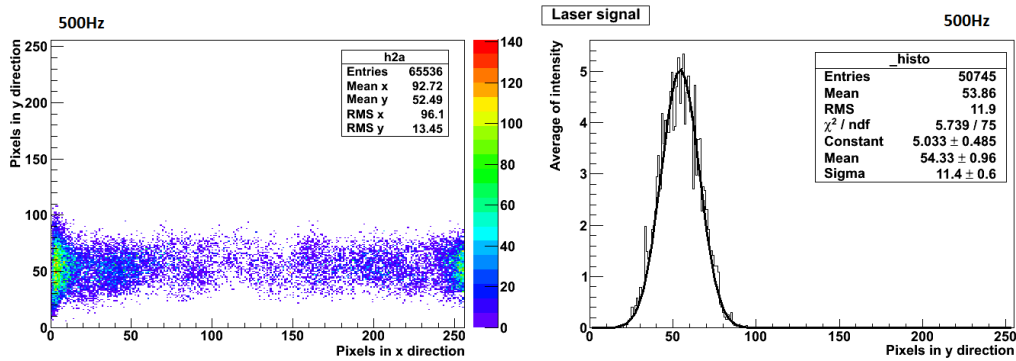
### 8.3. Data Taking with Virtex 6 Readout System



(a) Recorded data for 1 Hz laser frequency (b) Gaussian distribution for 1 Hz laser frequency



(c) Recorded data for 100 Hz laser frequency (d) Gaussian distribution for 100 Hz laser frequency



(e) Recorded data for 500 Hz laser frequency (f) Gaussian distribution for 500 Hz laser frequency

Figure 8.5.: Recorded laser signals with different frequencies and the referring gaussian distributions of the laser beam. For every frame the  $ToT$  values of each column are summed up and plotted into the referring histograms. The first and last 15 columns have been cut in order to avoid the disturbances at the edges of the Timepix chip. The number of entries come from the remaining pixels.

## 8. DATA WITH TPC PROTOTYPE

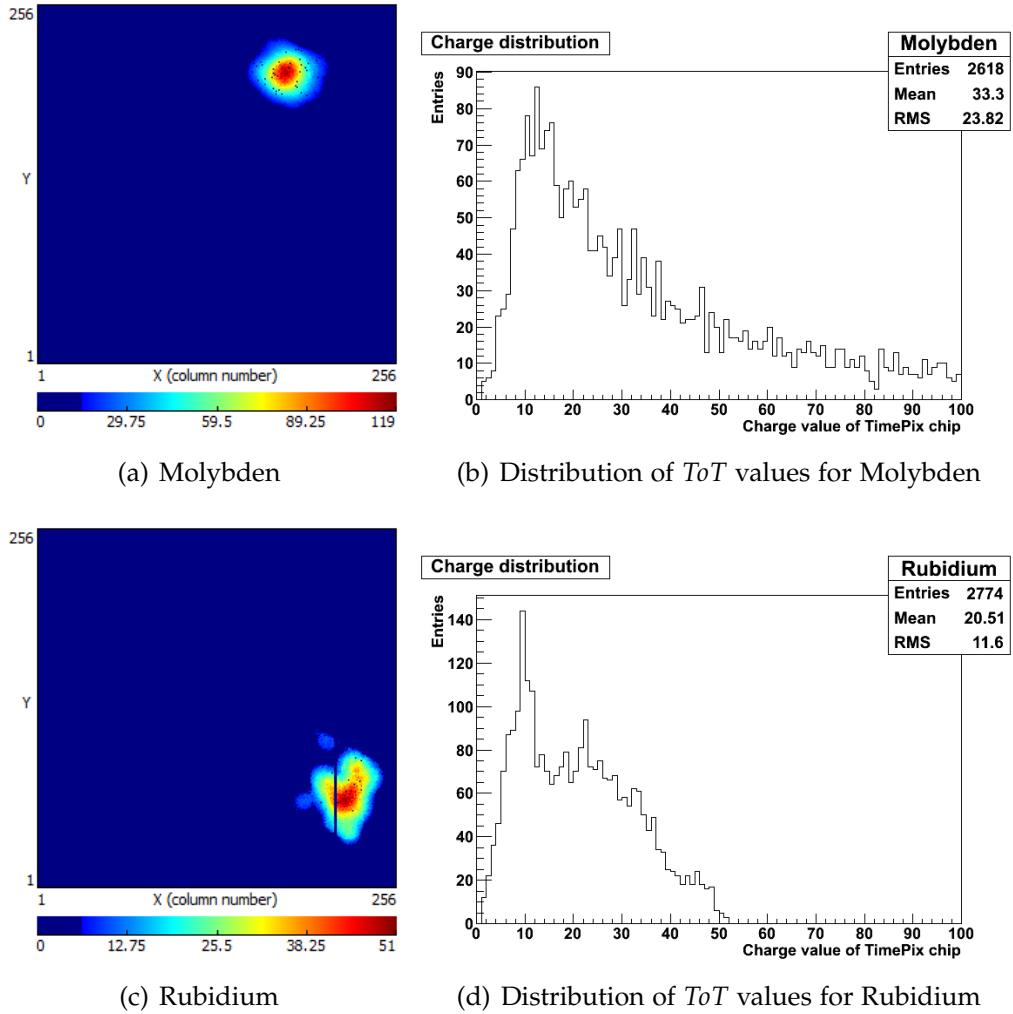
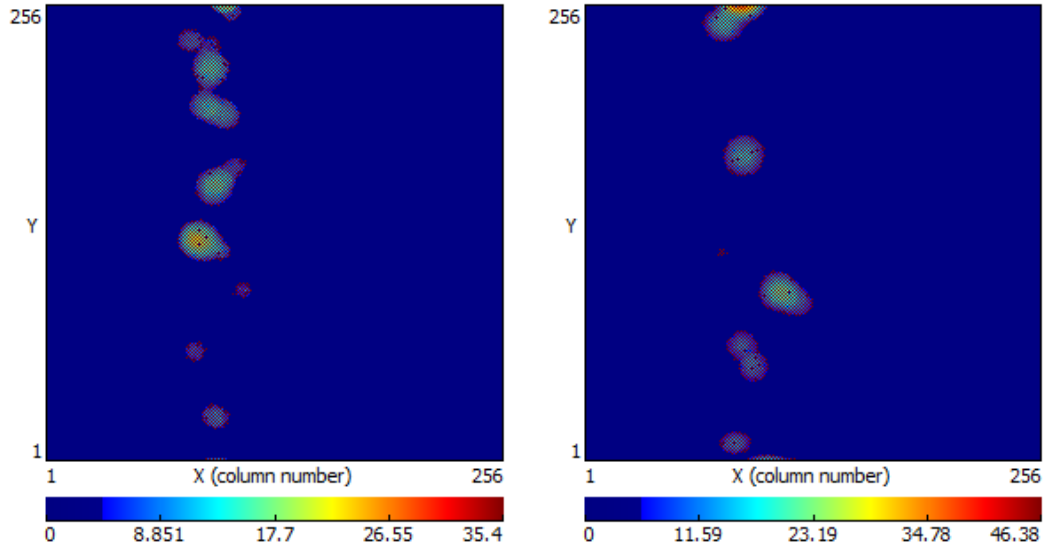
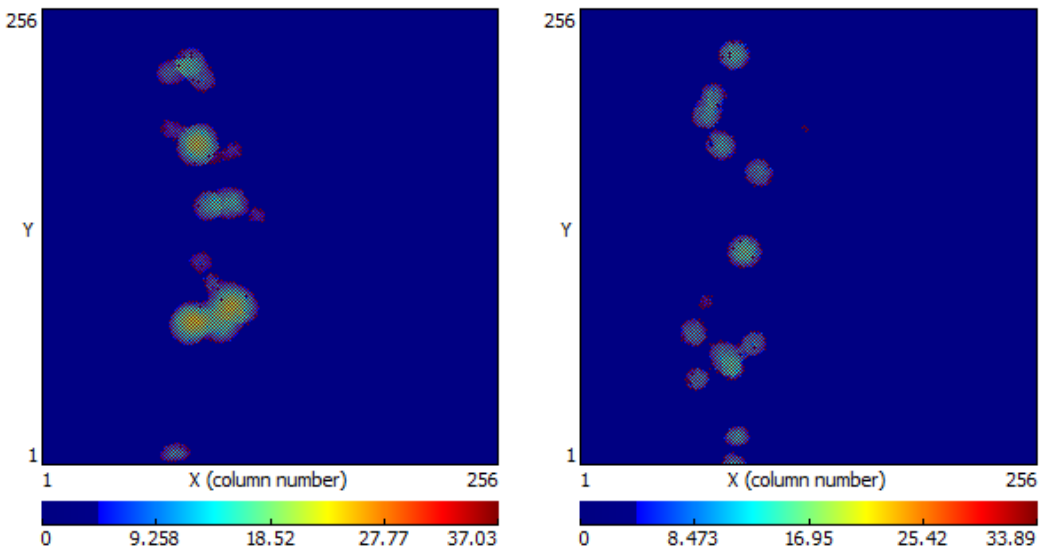


Figure 8.6.: Recorded signals with different radioactive sources. One can see, that the deposited charge for Molybden is higher than for Rubidium since it has a higher photon energy. The two histograms with the charge values of the different pixels show Landau distributions

### 8.3. Data Taking with Virtex 6 Readout System



(a) Recorded data with  $^{90}\text{Sr}$  and a shutter length of  $35\ \mu\text{s}$  (b) Recorded data with  $^{90}\text{Sr}$  and a shutter length of  $50\ \mu\text{s}$



(c) Recorded data with  $^{90}\text{Sr}$  and a shutter length of  $50\ \mu\text{s}$  (d) Recorded data with  $^{90}\text{Sr}$  and a shutter length of  $45\ \mu\text{s}$

Figure 8.7.: Sample tracks with  $^{90}\text{Sr}$  using 3 GEMs with 390 V for  $\text{ArCO}_2$  with a mixing ratio of 80:20 for different shutter windows.

## 8. DATA WITH TPC PROTOTYPE

In order to proof the gas mixing quality of the used gas mixture and to compare it with the theoretical result, the setup of the TPC has been changed to make a usage of the UV laser possible. For this reason the laser output is placed in front of the first entry hole of the TPC. On the opposite side a laser diode is placed, which can be used as a trigger signal for the Timepix chip.

At whole 500 frames for each gas mixture have been taken. Figure 8.8 shows the histograms with the distribution of all  $ToA$  values of every event for  $ArCO_2$  80:20 and 90:10. From that one can calculate the drift velocity according to the following equation:

$$v_{\text{drift}} = \frac{d}{t} \quad (8.1)$$

There  $d = 94$  mm is the distance between the entry hole of the laser and the upper side of the last GEM (near to the drift field). For the calculation of the the time  $t$  the following formula has been used:

$$t = t_s - \frac{ToA}{f} \quad (8.2)$$

Here  $t$  is the time information in  $\mu s$ ,  $t_s$  the shutter time with the same time unit,  $ToA$  the ADC value of the pixels in  $ToA$  mode and  $f = 40$  MHz the clock frequency in MHz. The  $ToA$  values are taken from the peak positions of the gaussian fits in Figure 8.8. In the case of the mixing ratio 80:20 the value of the peak position is 1091 and for 90:10 it is 858.8. The shutter window for 80:20 has been set to  $46 \mu s$  and for 90:10 to  $31.5 \mu s$

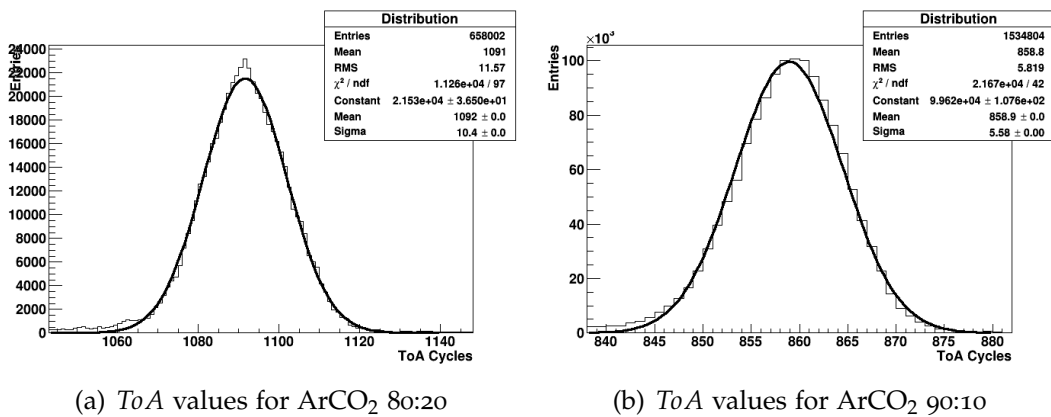


Figure 8.8.: Histogram of  $ToA$  values for two different gas mixtures with laser and photo diode used as a trigger

### 8.3. Data Taking with Virtex 6 Readout System

Inserting these values into equation 8.2 leads in summary to the drift velocities shown in Table 8.2. The errors have been calculated with the method of error propagation according to the following formula:

$$\sigma_v = \sqrt{\left(\frac{\partial v}{\partial(T_0A)}\sigma_{T_0A}\right)^2} = \frac{d}{f\left(t_s - \frac{T_0A}{f}\right)^2} \quad (8.3)$$

The values for  $\sigma_{T_0A}$  are 11.57 for 80:20 and 5.819 for 90:10. A graph for different drift velocities in ArCO<sub>2</sub> can be seen in Figure 8.9, which shows a comparison between the theoretical and experimental results.

This comparison proves, that the mixing of the gases works well, since the theoretical value lies inside the  $3\sigma$  area of the experimental one. Nevertheless for future analysis the experimental results have been taken.

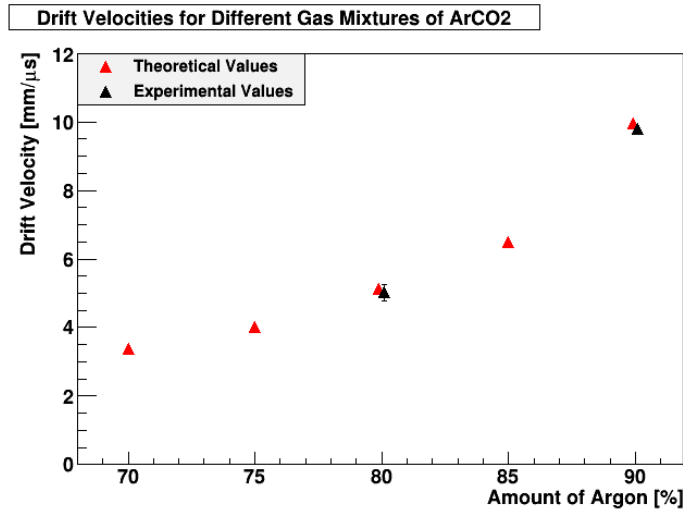


Figure 8.9.: Comparison between the simulated drift velocities with Magboltz [Bia11] and the measured results for different gas mixture ratios of ArCO<sub>2</sub>. The amount of CO<sub>2</sub> has to be calculated with the formula  $100 - x$ .

	ArCO <sub>2</sub> 80:20	ArCO <sub>2</sub> 90:10
<b>Simulation:</b>	5.128 mm/μs	9.965 mm/μs
<b>Experimental:</b>	(5.02 ± 0.07) mm/μs	(9.8 ± 0.15) mm/μs

Table 8.2.: Summary of the experimental and theoretical drift velocities for different gas mixtures

## 8. DATA WITH TPC PROTOTYPE

### 8.3.2 Measurements with Cosmic Muons

Type of GEMs:	Carbon Coated GEMs
Gas mixture:	Argon-CO <sub>2</sub> 80:20
GEM voltages:	420 V (GEM 1) 410 V (GEM 2) 400 V (GEM 3)
Drift field:	15.82 V/mm
Induction field:	300 V/mm
Transfer field 1:	200 V/mm
Transfer field 2:	200 V/mm
Outside temperature:	22°C
Pressure:	Normal atmospheric pressure
Distance Timepix chip – GEM 1:	2 mm
Distance GEM 1 – GEM 2:	1 mm
Distance GEM 2 – GEM 3:	1 mm
Drift distance:	290 mm
Ionisation Source:	Cosmic Muons
Clock frequency:	40 MHz
Shutter window::	80.5 $\mu$ s

Table 8.3.: Parameters of the test measurement with the TPC prototype for Virtex 6 Readout

This time cosmic muons were used for the measurements to check the performance of the TPC and for further analysis. The parameters for the measurement are given in Table 8.3. About 120,000 events have been taken with the gas mixture ArCO<sub>2</sub> and a mixing ratio of 80:20. During the measurement one could see, that approx. every second event was empty. One possibility to explain this effect is the small size of the Timepix chip compared to the width of the scintillators. The result of this is the fact, that some muons pass the TPC outside the active area of the chip and cannot be measured.

For the shutter length a value of 70 have been used, which leads to an effective shutter length of  $t_s = 70 \cdot 46/40 \mu\text{s} = 80.5 \mu\text{s}$ . This value has been chosen to cover all signals over the complete drift length of 290 mm, since the

drift velocity for this gas mixture is assumed as  $5.128 \text{ mm}/\mu\text{s}$  according to simulations. The final analysis of the data has been done with MarlinTPC, which is described below in section 8.5.

A sample frame with the track of a cosmic muon measured with the Virtex 6 readout system can be seen in Figure 8.10. These histograms show the  $ToT$  and  $ToA$  values of the same track separately. The clusters from the primary ionisation are clearly visible. The direction of the track can be determined with the help of the  $ToA$  values. More plots of muon tracks with the Virtex 6 readout system are presented in Appendix E.1.

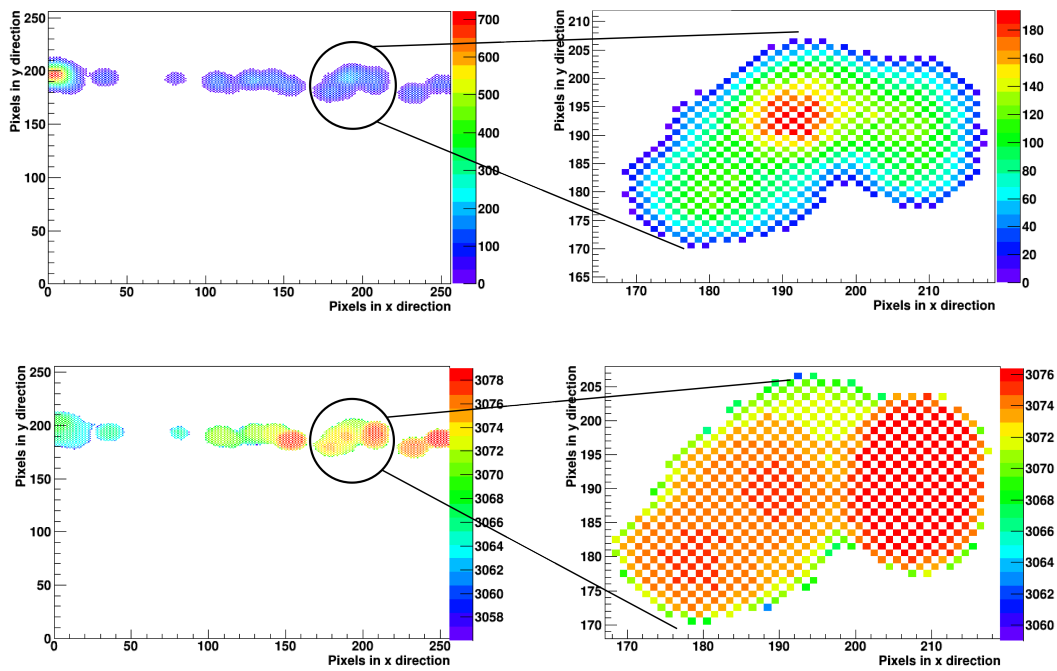


Figure 8.10.: Sample measurement of cosmic muons with the Timepix chip and Virtex 6 readout. The upper plots show a track event, in which only the pixels in  $ToT$  mode are shown. The lower one presents the same track with only pixels in  $ToA$  mode. The direction of the track can be calculated with the help of the  $ToA$  values, where a smaller  $ToA$  values refer to a longer drift distance.

#### 8.4 MARLINTPC

The main purpose to develop the software Modular Analysis & Reconstruction for the LINear Colider (Marlin) was to create a modular reconstruction and

## 8. DATA WITH TPC PROTOTYPE

analysis framework based on Linear Collider Input/Output (LCIO) [Mar14]. The motivation for this purpose is the fact, that different research groups work in principle on the same topic of detector physics, but with different systems like readout electronics and amplification methods.

A proposal was made to use the existing Marlin framework with minor changes inside the ILC TPC community, in order to make data exchange possible by using the same units, same coordinate systems, same data file structures etc.

MarlinTPC [Wie07] itself consists of different modules in the form of processors. It needs a steering file mechanism, which allows to activate and define the parameters of each processor. These parameters are saved in XML files with a special description language. One of the important features was to make usage of a GEAR<sup>1</sup> file, which includes the geometrical details of the TPC and can be used by all processors.

The parameters, which are not fixed for a detector operation, but can change during the measurement, (like drift velocity, amplification) are stored inside LCCD<sup>2</sup>. The parameters and functions of the most important processors inside MarlinTPC will be explained. In order to reconstruct and analyse the data of a TPC with MarlinTPC, the following four steps (including theirs main tasks for the analysis for Timepix data) are essential:

- Conversion of raw data into Zero Suppressed Data (Conversion chain).  
Conversion of the raw data from the Timepix chip into a special file format for MarlinTPC
- Application of calibration parameters (Calibration chain) from the calibration of the Timepix chip.
- Reconstruction of data (Reconstruction chain):
  - Finding clusters in all events
  - Separating clusters into their subclusters
  - Finding and fitting tracks with the Hough transformation and weighted linear regression
- Analysis of data (Analysis chain):
  - Calculating the geometrical distributions for the LCIO parameters
  - Finding residuals for calculation of spatial resolution
  - Analysing the cluster parameters like cluster size, charge etc.

<sup>1</sup> GEometry API for Reconstruction (GEAR) stores informations about e.g. the pad geometry, clock frequency and detector diameters

<sup>2</sup> Linear Collider Condition Data Toolkit (LCCD)



## 8.5 DATA ANALYSIS WITH MARLINTPC

### 8.5.1 *Conversion Chain*

Every Timepix chip has an active area of  $256 \times 256$  pixels. The *ToT* or *ToA* ADC values for all pixels are saved as a matrix in one event file. Multiplying the number of entries with the factor 2 because of the spaces<sup>3</sup> between the values, the minimum file size of such an event is  $2 \cdot 256 \cdot 256 = 131072$  bytes, if all values are either zero or integers below 10. The reason for this is, that each ASCII character is defined by exactly 1 byte. For every event, which includes hits, the file size can only be the same or larger than the above calculated value.

It is not unusual, that the taken data can exceed several Gigabytes after the completion of one single run with thousands of events. Therefore it is recommended to convert the data with Marlin into zero suppressed data with the help of the **TimePixZeroSuppressionProcessor**, which is a part of the LCIO framework. This processor is simply deleting the zero values from every event and arranges the values, which are above zero, into special vectors with defined starting points.

By this method it is also possible to set a specific threshold manually, which neglects all values below this threshold. Since the threshold has been set for the measurement and the calibration of the chip has been already done, this value can be set to 0, i.e. no additional threshold is taken into account.

### 8.5.2 *Calibration Chain*

The next step after the conversion of the data with Marlin is the application of the calibration values. For this the values of the charge calibration, timewalk compensation, the pixel mask and the mask for the bad pixels<sup>4</sup> are taken into account. The parameters of the *ToT* and *ToA* calibration have to be written into one text file.

After this LCIO event files must be created with the processor **TimePix-CalibParamReaderProcessor**. It needs all together eight input parameters: four from the charge calibration and four from the timewalk compensation. With the help of the processor **MyTimePixMaskCreatorProcessor** a mask for

<sup>3</sup> In every event file the *ToT* and *ToA* values are separated by a space, which has the ASCII code 32 and is equal to 1 byte.

<sup>4</sup> Bad pixels are defined as pixels, which always give a value of overflow, that is 11800 for the Timepix chip.

the Timepix chip is created by reading the mask files for the bad pixels in order to ignore them in the following reconstruction chain.

The processor **TimePixModeMapCreatorProcessor** marks the pixels according to their mode during the measurement procedure. An example is the mixed mode, which sets the first pixel into *ToT* resp. *ToA* mode and the following pixel into *ToA* resp. *ToT* mode and continues to cover the whole chip with a chess matrix as explained in section 6.1.

The result of the timewalk calibration has been applied on one sample cluster in order to show the compensation of the timewalk effect as one can see in Figure 8.11. For this purpose the *ToT* value of the pixel, which has been set to *ToA* mode, must be known. In order to get this value, the four *ToT* values around each pixel in *ToA* mode have been taken in order to calculate their average value, which is very near to its real value.

This value must be then calculated into a voltage signal, which is equivalent to a given test pulse with the same signal height according to equation (6.2). With the help of equation (6.4) the referring compensated timewalk coefficient can be calculated for each pixel to be subtracted from the actual *ToA* value. Figure 8.11(a) shows the result before timewalk compensation, while the result after the timewalk compensation can be seen in Figure 8.11(b).

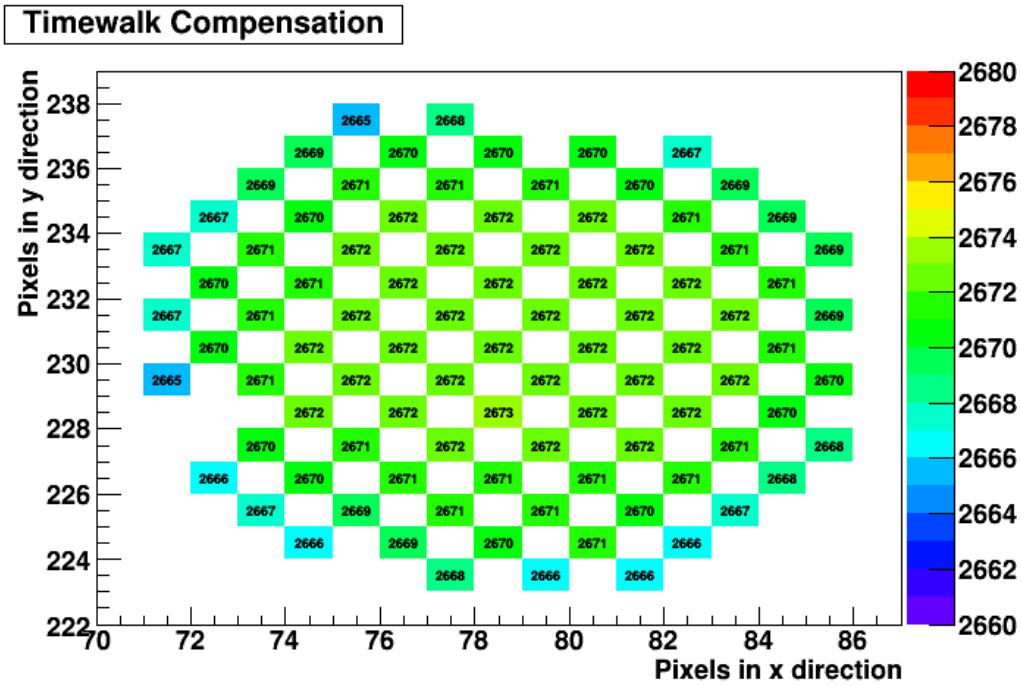
### 8.5.3 Reconstruction Chain

#### *Cluster Finding and Separation in Marlin*

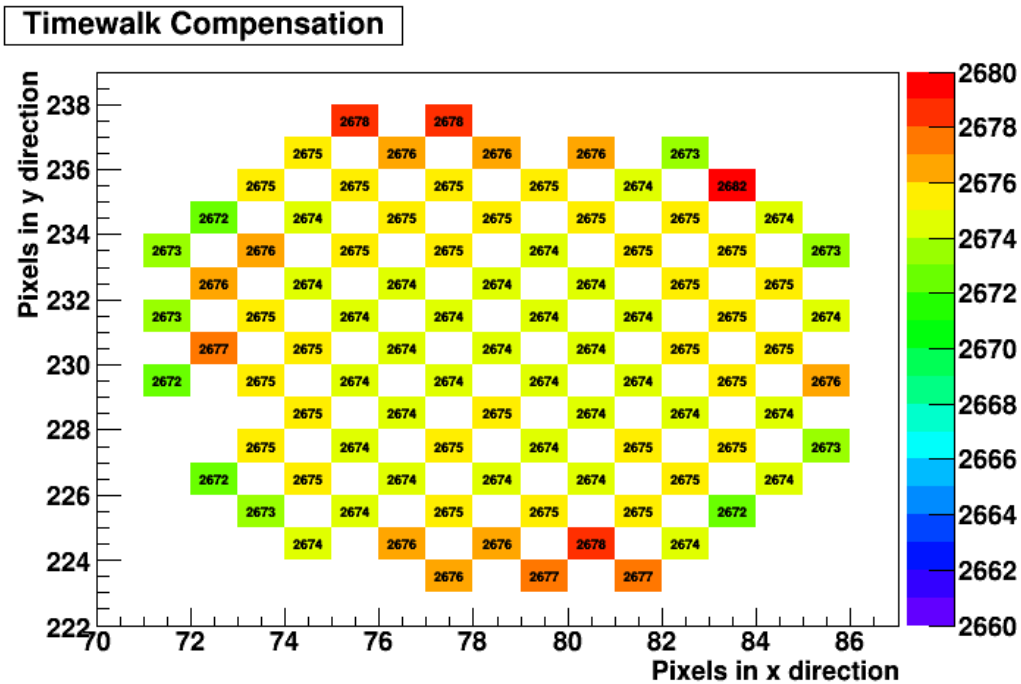
The processor **TimePixClusterFinderProcessor** in Marlin is able to identify clusters inside every event. Before starting the cluster finding process it is necessary to define the minimum amount of pixels in order to be recognised as a cluster. According to [Zim98] a value of 3 leads to good results and is also used in the following analysis chain. A typical result from the output of this processor is shown in Figure 8.12(a).

After finding the clusters, they must be separated into smaller ones, which are normally touching or overlapping each other. This is done with the **TimePixClusterProjectionSeparatorProcessor**. Before the separation, this processor projects the clusters to the cluster axis by calculating a weighted linear regression through all pixels as shown in Figure 8.12(b). After this the charge distribution of one cluster of the shown event leads to the output presented in Figure 8.13, which shows two clusters from one sample track consisting of several subclusters.

After finding the maxima and minima of each cluster, the processor divides the cluster into its subclusters, if they are existing.



(a) Sample cluster before timewalk compensation



(b) Sample cluster after timewalk calibration

Figure 8.11.: The application of the timewalk compensation parameters on a sample cluster. Before the application the pixels near the center of the cluster have a higher  $ToA$  value compared to the outer ones due to the timewalk effect. After compensating this effect, the standard deviation between all pixels becomes smaller.

## 8. DATA WITH TPC PROTOTYPE

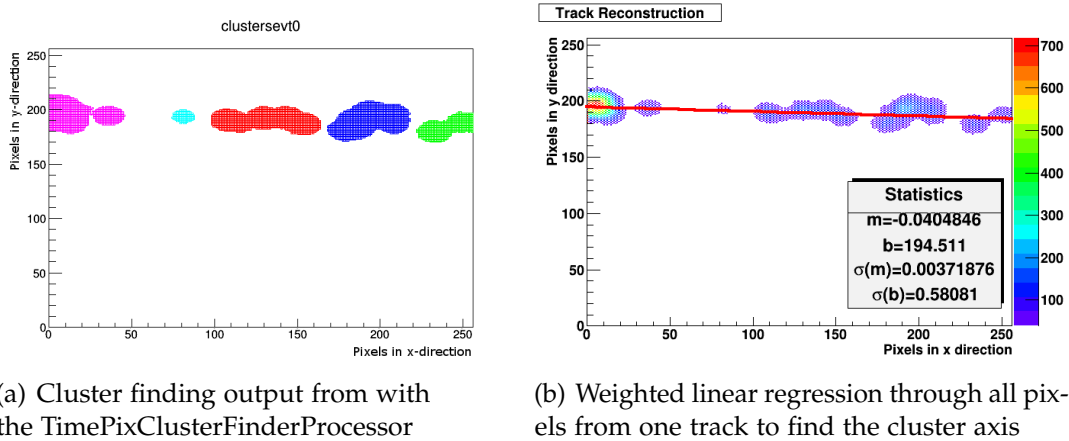


Figure 8.12.: Output of a sample event from the TimePixClusterFinderProcessor and calculated linear regression for finding the cluster axis

The last step, which is being done by the **TimePixHitCenterCalculatorProcessor** is the calculation of the center of each cluster. For this purpose the simple weighted mean functions are used, where the weighting factor is the charge information of each pixel.

### Track Finding in Marlin

For the track finding a Hough transformation [Hei13] is used, which creates for every pixel in the image space a line in the parameter space. In the image space of the Timepix chip a straight line can be described by the linear equation

$$y(x) = a \cdot x + b \quad (8.4)$$

For a single pixel with the coordinates  $x_i$  and  $y_i$  the line in the parameter space will look like follows:

$$b(a) = -a \cdot x_i + y_i \quad (8.5)$$

For using the Hough transformation algorithm it is necessary to plot the lines for all pixels, which have a non-zero  $ToT$  value, for the parameter space into a histogram. The point, in which most of the lines intersect, will give the parameters  $a$  and  $b$  for the reconstructed track in the image space. A sketch of the working principle can be seen in Figure 8.14.

The Marlin processor **TrackFinderHoughTrafoProcessor** uses this method to reconstruct the track of a particle through the TPC. Inside the xml file it is possible to define the minimum amount of pixelspara, which are needed to fit a track. The default value, which gives normally good results, is 5.

## 8.5. Data Analysis with MarlinTPC

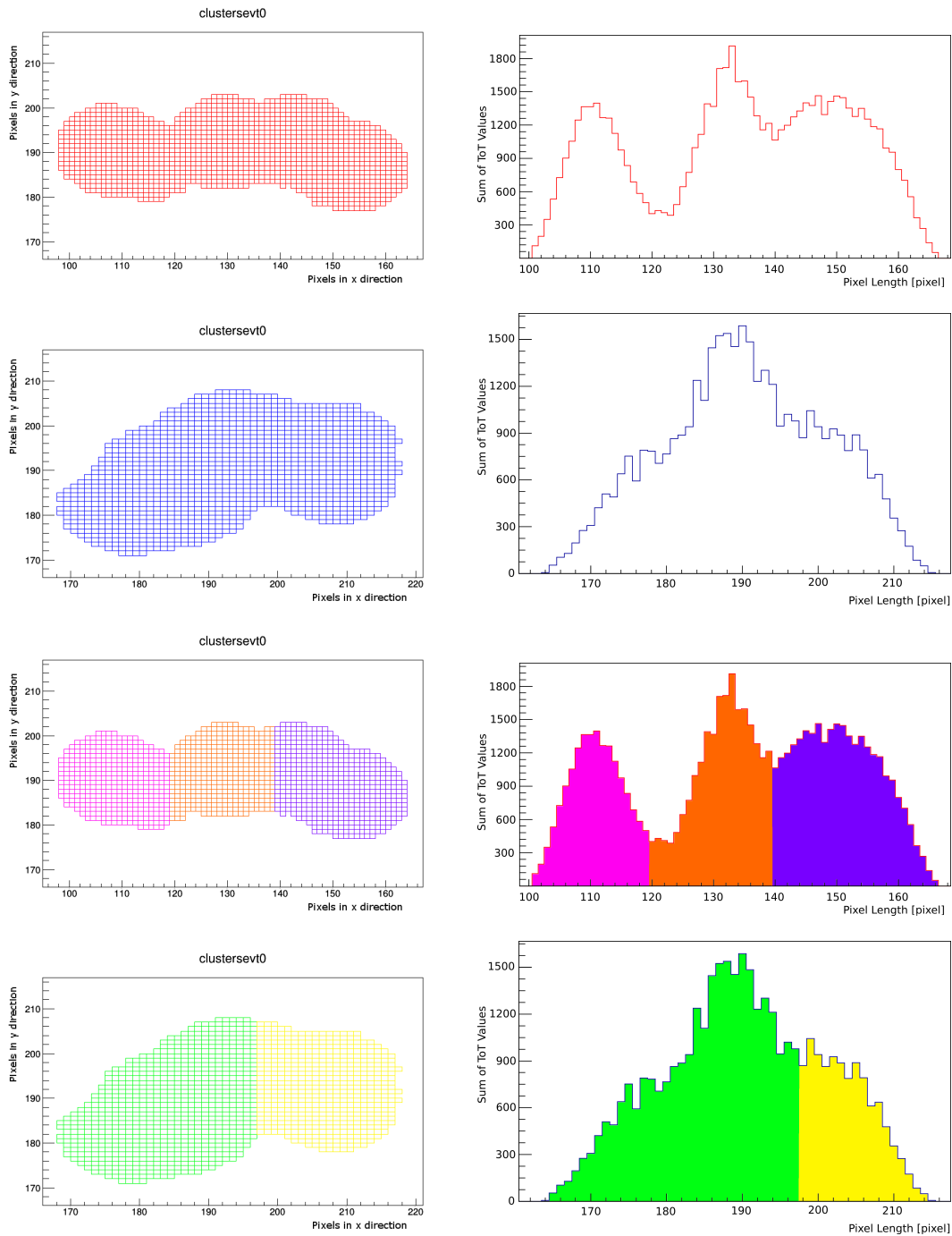


Figure 8.13.: Output of the sample event from the 1st and 2nd `TimePixClusterProjectionSeparatorProcessor`. The shown clusters from the track in Figure 8.12 are the red and blue ones with the corresponding distributions. One can identify the minima inside each cluster, which are used for the separation. The separated clusters are presented in different colours. The top two rows show the cluster and the  $ToT$  sum before the separation and the lower rows after the separation.

## 8. DATA WITH TPC PROTOTYPE

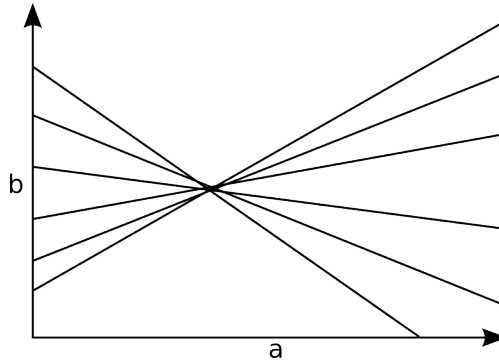


Figure 8.14.: Sketch of the working principle of the track finding with the Hough transformation. The intersection point in the parameter space is giving the parameters for the track reconstruction.

Since it is essential to avoid infinite line slopes, this algorithm is applied two times. First it calculates the lines for values of  $a$  between  $-1$  and  $1$  according to equation (8.4) and then again according to the following formula:

$$x(y) = a \cdot y + b \quad (8.6)$$

which leads to the parameters of an orthogonal line.

One big issue of this method of track finding is the fact, that the errors due to the binning of the parameter lines are relatively large, if the binning is not fine enough. But it is also important to make the binning not too fine, because then the interception point will be too diffused. Finding a optimum binning is one of the most important tasks issues for this processor.

The recalculation is done after this with the help of the processor **Linear-RegressionProcessor**, which is simply calculating the parameters  $a$  and  $b$  via an unweighted linear regression. For the condition  $|\phi| < \pi/4$  the equation (8.4) is used and for  $|\phi| > \pi/4$  the equation (8.6) is taken into account.

For the track reconstruction in three dimensions the linear regression is done in the  $x$ - $z$ -plane and  $y$ - $z$  independently according to the following formulas:

$$z(x) = c \cdot x + d \text{ for } |\phi| < \frac{\pi}{4} \quad (8.7)$$

$$z(y) = c \cdot y + d \text{ for } |\phi| > \frac{\pi}{4} \quad (8.8)$$

From these parameters one can calculate the standard **LCIO** parameters, which are the following:

- The parameter  $\phi$ , which is the angle between the track projection and the  $x$ -axis

$$\phi = \arctan(a) \text{ for } |\phi| < \frac{\pi}{4} \quad (8.9)$$

$$\phi = \pi/2 - \arctan(a) \text{ for } |\phi| > \frac{\pi}{4} \quad (8.10)$$

- The parameter  $\lambda$ , which is the angle between the track and its projection into the  $x$ - $y$ -plane.

$$\lambda = \arctan\left(\frac{c}{\sqrt{a^2 + 1}}\right) \quad (8.11)$$

- The parameter  $d_0$ , which is the shortest distance between the origin of the coordinate system and the track projection

$$d_0 = b \cos(\phi) \text{ for } |\phi| < \frac{\pi}{4} \quad (8.12)$$

$$d_0 = -b \sin(\phi) \text{ for } |\phi| > \frac{\pi}{4} \quad (8.13)$$

- The parameter  $z_0$ , which is the distance between the nearest point of the track projection to the origin and the nearest point to that on the track

$$z_0 = \frac{-a \cdot b \cdot c}{\sqrt{a^2 + 1}} + d \quad (8.14)$$

Figure 8.15 shows the sketch of a track including the definition of the track parameters. The derivation of these parameters can be found in Appendix B.

#### 8.5.4 Analysis Chain

In the analysis chain several parameters of the TPC with a given gas mixture can be determined. The most important ones are the spatial, geometric and LCIO track parameter distributions. All results shown here are from the measurements with cosmic muons.

##### *Spatial Resolution*

One important parameter for the track and consequently the momentum resolution are the diffusion constants for different gas mixtures. They are usually limiting the resolution.

Figure 8.16 shows the longitudinal and transversal diffusion constants as a function of the mixing ratio of ArCO<sub>2</sub>. It is very clear to see, that with

## 8. DATA WITH TPC PROTOTYPE

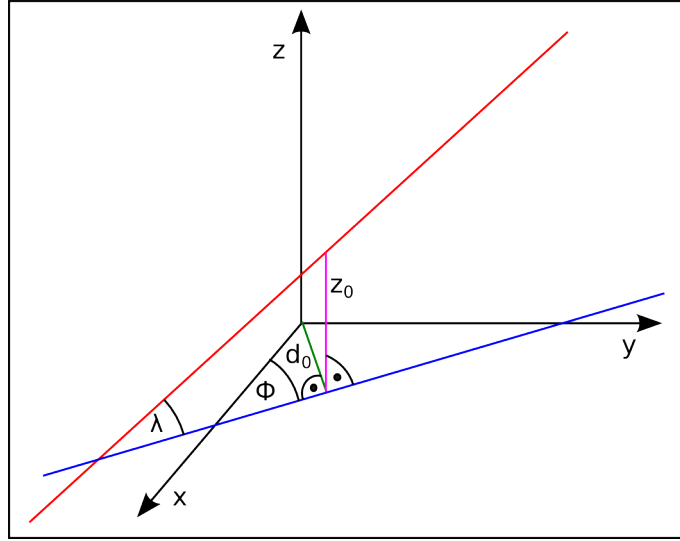


Figure 8.15.: Sketch of a track (red) with its projection into the  $x$ - $y$ -plane (blue) including the definition of the LCIO track parameters.

less quencher the diffusion increases, while for more quencher the diffusion constants fall down asymptotically to a specific value, which is approx.  $183 \mu\text{m}/\sqrt{\text{cm}}$  for the transversal and longitudinal diffusion constant according to Magboltz. For a higher amount of Argon the longitudinal and transversal diffusion constant also differ more than for mixtures with less Argon.

The diffusion constant can also be determined from the taken data. The used method for finding the spatial resolution is the **geometric mean method**, which is used to fit a line through every hit/cluster center. From that one derives the residuals by calculating the distances between the fit and the hits and finding the mean value  $\sigma_N$  of them. This method is illustrated in Figure 8.17.

The index  $N$  is used to show, that all  $N$  hits are included in the data fit. One can show, that the residuals are too large by using this method. Another possibility is to use  $N - 1$  data points for the fit and calculate the residual between the fit and the hit, which is neglected. At the end this method will lead to a residual  $\sigma_{N-1}$ , that is too small. A closer look shows, that the exact value  $\sigma$  for the residual is very near to the geometric mean of both values according to the following formula:

$$\sigma = \sqrt{\sigma_N \sigma_{N-1}} \quad (8.15)$$

For the calculation of the spatial resolution, i.e. the diffusion in the  $x$ - $y$ -plane, the data of all events for the drift length of upto 290 mm is divided into 116



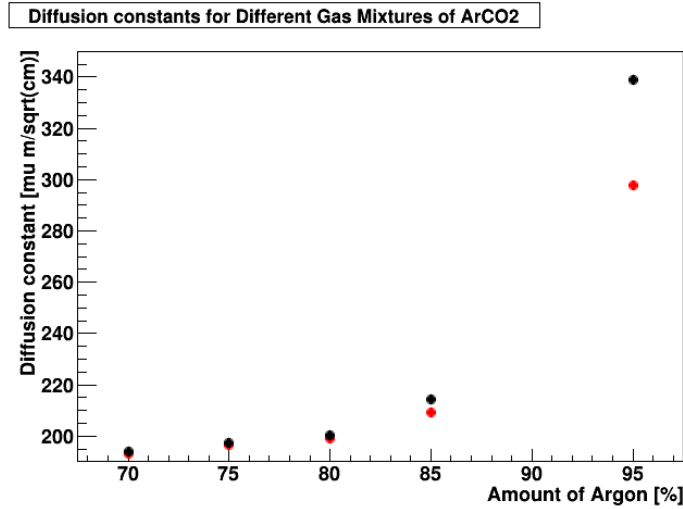


Figure 8.16.: Simulated diffusion constants with Magboltz [Bia11] for different gas mixture ratios of ArCO<sub>2</sub>. The amount of CO<sub>2</sub> has to be calculated with the formula  $100 - x$ . The transversal diffusion constant is shown with red dots and the longitudinal diffusion with black ones.

$z$ -bins. For each  $z$ -bin the residuals are calculated and plotted against the distance in  $z$  direction. Figure 8.18 shows one example for the bin  $40 \text{ mm} < z < 42.5 \text{ mm}$ .

From these calculated RMS values the diffusion constant  $D_t$  of the transversal diffusion can be calculated according to the following equation:

$$\sigma = \sqrt{\sigma_0^2 + D_t^2 z} \quad (8.16)$$

which is used for the fit function in the plot of Figure 8.19. The theoretical value for the used gas mixture ArCO<sub>2</sub> (80:20) according to Magboltz [Bia11] is  $D_t = (199 \pm 1.1) \mu\text{m}/\text{cm}^2$ , which is very near to the experimental measured one  $D_t = (201.6 \pm 0.3) \mu\text{m}/\text{cm}^2$ . For the calculation the data with the cosmic muons have been used. The values for higher drift lengths have been neglected due to less statistics, as one can see in Figure 8.21(c).

For calculating the longitudinal diffusion coefficient  $D_l$  the same method has been used. In this case the theoretical value according to Magboltz is  $D_l = (201.0 \pm 0.8) \mu\text{m}/\text{cm}^2$ . Again the drift distance is divided into 116  $z$ -bins, but in this case the residuals are calculated from the  $ToA$  value to get a distribution for the  $z$ -direction. Figure 8.20 shows the plotted residuals against the drift distance. The experimental value taken from this is  $D_l = (203.0 \pm 0.6) \mu\text{m}/\text{cm}^2$ . The value is again very near to the theoretical coefficient.

## 8. DATA WITH TPC PROTOTYPE

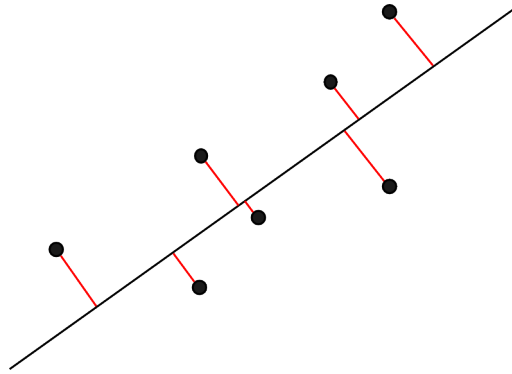


Figure 8.17.: Calculation method to find the residuals  $\sigma_N$  of a line fit

### *Geometric Distributions*

The plots of the different geometric distributions are calculated by the **MyXYZ-DistributionTracksProcessor** and can be seen in Figure 8.21. These plots show either the summed hits of each pixel row (distribution in  $y$ -direction) or of each pixel column (distribution in  $x$ -direction). The distribution in  $x$ - and  $y$ -direction is homogeneous, i.e. the RMS value of each pixel from a calculated average is quite small. This assumption can be proven by the plot for the distribution in  $x$ - $y$ -direction, which shows the summed up charge of every pixel.

The peaks at the highest and lowest values of the  $x$  and  $y$  distributions are explained by the effect, that the center of clusters near the edges of the Timepix chip can have their center outside of the active area of the Timepix chip. In this case the reconstruction process leads to wrong results, because it always calculates the edges of the chip as the center of these clusters. This increases the entries for these pixel rows and columns to higher values than they actually have.

The falling edge of the graph of the  $z$ -distribution behind the maximum around 80 mm can be explained by the diffusion of the electrons. Due to the fact, that the size of each cluster increases during the drift time, the charge of the clusters with less ionisation can be under the threshold of the pixel cells. In this case there is either no hit at all in this event or the cluster is too small to be identified during the reconstruction process. In both cases it will lead to the calculated wrong result, which is discussed above.

### *LCIO Track Parameter Distributions*

Figure 8.22 shows the distributions for the track parameters, which are calculated by Marlin. Since the data is taken with cosmic muons, the distribution

## 8.5. Data Analysis with MarlinTPC

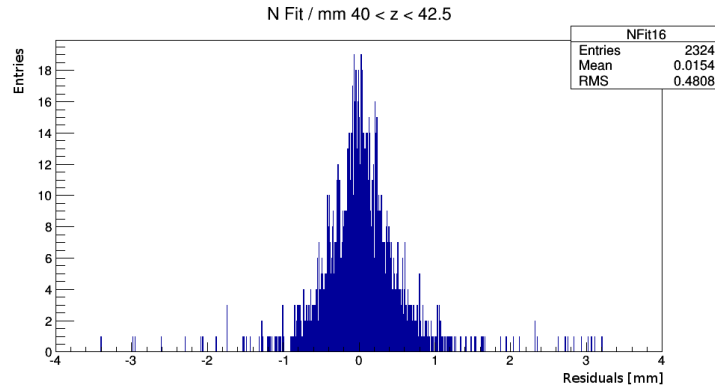


Figure 8.18.: Example for the z-binning to calculate the spatial resolution

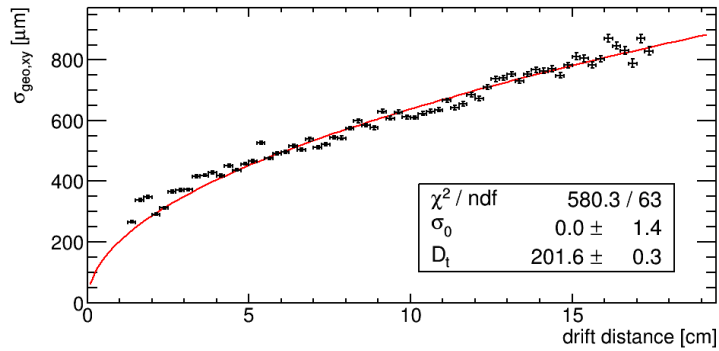


Figure 8.19.: The plot with fit function for calculating the transversal diffusion coefficient  $D_t$

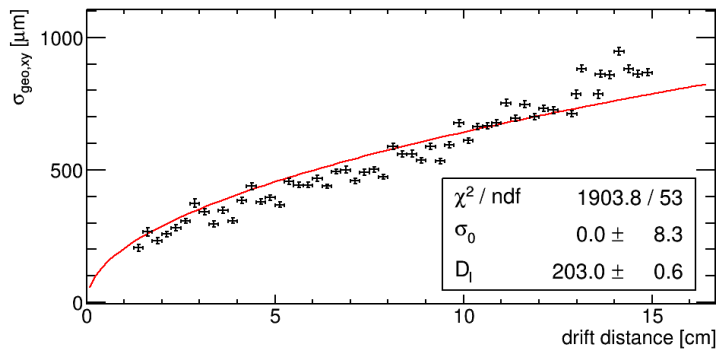


Figure 8.20.: Plot with fit function for calculating the longitudinal diffusion coefficient  $D_l$

## 8. DATA WITH TPC PROTOTYPE

for the angle  $\phi$  between the track and the  $x$ -axis of the Timepix chip plane shows the expected behaviour. For the angle  $\lambda$ , which represents the tilting in  $z$ -direction, the distribution looks almost the same.

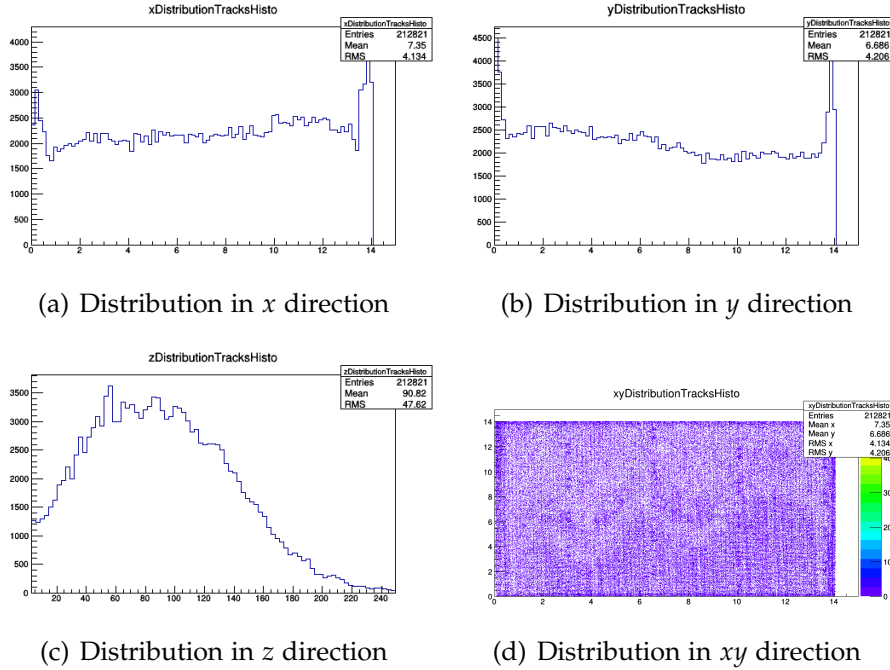


Figure 8.21.: Geometric distributions for different geometrical directions

The parameter  $d_0$  is in principle proportional to  $\sqrt{x^2 + y^2}$ . Therefore the distribution looks similar to the one of the  $x$ - and  $y$ - direction and the edge effect of the higher entries can be observed again. The distribution for the parameter  $z_0$  is almost the same like the one shown in Figure 8.21.

### Cluster Analysis with Marlin

Cluster finding and analysis is very important to determine the quality of the reconstructed tracks in different events. Normally one primary electron creates one single cluster. If the distance between the point of primary ionisation and gas amplification is too small, two or more clusters can overlap and create a cluster, which includes more charge than one single cluster has. For larger drift distances the diffusion takes into account and the space between two different clusters increase until they are totally separated. This phenomena is called declustering effect.

If two clusters from different primary ionisations overlap, the charge is approx. twice the one for a single cluster. In opposite to this the cluster size

## 8.5. Data Analysis with MarlinTPC

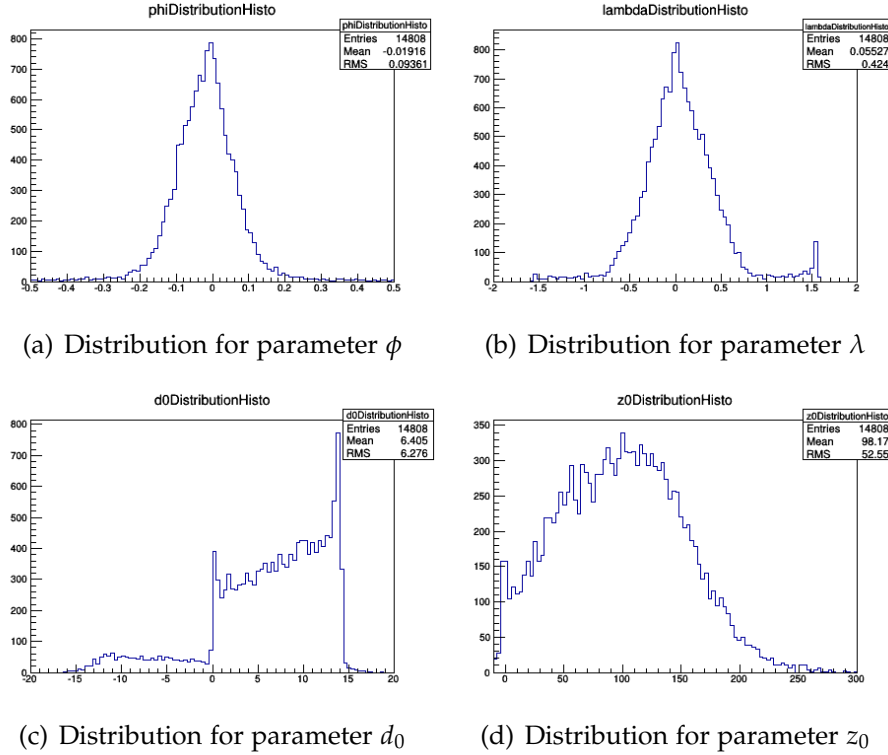


Figure 8.22.: Distributions for the track parameters calculated by Marlin

does not change and is almost the same like for a single ionisation. Due to this reason, the cluster size is not increasing proportional to the cluster charge in the case of smaller drift distances. It was found experimentally, that the average cluster size  $s$  can be described as a function of the drift distance  $z$  according to the following equation [Brz13]:

$$s(z) = \alpha \exp(-\beta z) + \gamma \quad (8.17)$$

The free parameters  $\alpha$ ,  $\beta$  and  $\gamma$  can be found by fitting a curve through all measured data points. Therefore one expects an increase in the number of clusters for larger drift distances in case of the same amount of primary ionisations. On the same time another effect has to be taken into account, which is caused by a small quantity of oxygen inside the gas volume. Oxygen captures the drifting electrons and decreases the number of clusters the more far away they are from the point of gas amplification.

It can be therefore assumed, that the number of electrons  $n_e$ , that reach the readout plane, can be calculated with the formula

$$n_e = A \exp(-Bz) \quad (8.18)$$

## 8. DATA WITH TPC PROTOTYPE

where  $A$  is the number of initially created electrons and  $B$  the absorption coefficient for the electrons drifting along the  $z$ -axis.

From equation (8.17) it can be derived, that the number of primary electrons per cluster is as follows:

$$n_{e/\text{cluster}} = 1 + C \exp(-Dz) \quad (8.19)$$

Dividing equation (8.18) by (8.19) leads as a result to the function, which describes the number of clusters per drift length reaching the readout plane after drifting the distance  $z$ :

$$n_{\text{cluster}} = \frac{A \exp(-Bz)}{1 + C \exp(-Dz)} \quad (8.20)$$

The result of the data set with the fit function according to this equation can be seen in Figure 8.23. This plot shows, that for the given gas mixture, TPC geometry and gas amplification the maximum of detected clusters per track length lies around  $z = 4$  cm.

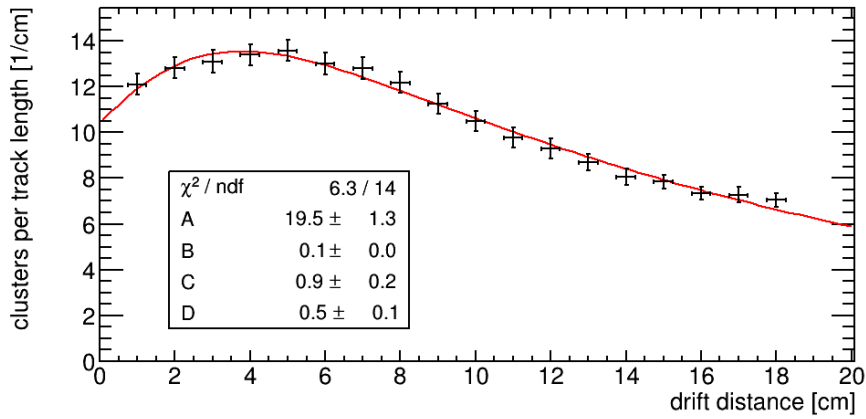


Figure 8.23.: Plot of the number of clusters per drift length against the drift distance  $z$

## CONCLUSION AND OUTLOOK

---

A TPC combines the advantages of a low material budget and a high resolution for track reconstruction and analysis. Another advantage is the low energy loss of particles due to few collisions with atoms inside the gas volume. Together with GEMs, which are used for gas amplification, a very good spatial resolution of less than  $100\ \mu\text{m}$  can be achieved.

In this thesis it was shown, that it is possible to exchange the pad readout by a single pixel chip with a much smaller detection area on the one hand, but on the other hand with a much higher spatial resolution due to a finer detection grid, which is essential for a track reconstruction. In order to increase the active detectable area, the next step is usage of a pattern consisting of up to 96 pixel chips on one end plate.

During the study of the Timepix chip it was found out, that the calibration with the USB device lead to incorrect and non-reproducable results. These problems are not fully investigated until now, but could be solved together with its developers in Prague. Another important feature, which is planed to be implemented in the near future, is to create the possibility for the Timepix chip to accept internal test pulses, so that an external pulse generator will not be needed. It is expected, that the new version of the pixel chip Timepix 3 will be released soon. It will come with a higher TDC accuracy and the possibility to read the  $ToA$  and  $ToT$  value of one pixel at the same time.

For this thesis the existing TPC prototype at the University of Siegen has been changed in this way, that it can hold a stack of three GEMs, which is necessary to guarantee a signal above the threshold of the Timepix chip. It was also necessary to change the setup of the prototype in this way, that the carbon coated GEMs can be inserted easily, after they have been tested effectively inside the small test chamber.

Another task was to install a complete new readout system by changing the previous used pads to a pixel chip. For this purpose the new FPGA card has been also tested successfully to make an extension to more than one chip possible for the future.

With the analyses, which are presented in the previous chapters, it could be shown, that carbon coated GEMs show a better gain stability and resistance against sparks for higher GEM voltages. The next step is to investigate ceramic GEMs, which should show the same behaviour like carbon coated GEMs but with a higher stability against surface damages. Until now no investigation

## 9. CONCLUSION AND OUTLOOK

regarding this topic has been done. It was possible to analyse the data taken with the TPC prototype inside the MarlinTPC analysis framework. The results fit very well to the theoretical values, which shows, that the whole system is working well.

At the end it can be concluded, that the analysis of the taken data with laser and cosmic muons show good similarities to the theoretical values. The measurements with the Timepix chip lead to the result, that a sufficient spatial resolution can be achieved by analysing electron clusters with a fine grid of charge sensitive pixels. The advantage of detecting single electrons gives the possibility to make a deeper analysis of charge clouds like calculating the diffusion coefficient or the number of electrons per drift length. The disadvantage is the necessity of a higher gas gain compared to a pad readout structure, which can make the whole system unstable and increases the possibility for discharges. This problem could be solved with the help of the used carbon coated GEMs, which make it possible to operate the TPC at higher gas gains compared to standard GEMs. As a conclusion it appears, that a carbon coated GEM based TPC in combination with a general CMOS pixel readout system seems to be the best choice as the main tracking detector for the future linear collider.





## TOS COMMANDS

---

In this chapter the basic commands for TOS are presented, which have been used for the calibration and measurements for this thesis.

### A.1 COMMANDS FOR INITIALISATION OF CHIP

- How many chips are on the board?  
enter **1** (used for this thesis)
- enter **1f** (Loading from DAC values from fsr.txt )
- enter **5** (reading of fsr.txt and writing DAC values into chip)

### A.2 COMMANDS FOR THRESHOLD EQUALISATION

- enter **6** (THS optimisation is starting)  
How many chips you want to optimise → enter **1**  
start THS with extended coarse → enter **0**
- enter **7** (THL equalisation is starting)  
How many chips you want to optimise → enter **1**  
Equalisation will be done for chip 1. How many pixels per row at same time? → enter **2**  
Do you want to use the extended coarse range? → enter **0**

### A.3 COMMANDS FOR CHARGE CALIBRATION

- enter **8a** (starting the a fast calibration)  
TOT(**0**) or TOA(**1**) → enter **0**  
(choose option 0 to start charge calibration measurement)
- For the spacing how many pixel per row at the same time? 1,2,4,8,16 ?  
→ enter **8**
- Shutter length: press **1** for short shutter (0-255 clock cycle) press **2** for long shutter (256- 65280 clock cycle)  
→ enter **1** (in the case of this thesis)

## A. TOS COMMANDS

- What is the voltage you set at the external test pulser in mV?  
→ enter 30 (starting from 30 mV to 800 mV)
- After finishing all the measurement with different voltage values at the end it is saved a file with name TOTCalib.txt

### A.4 COMMANDS FOR TIMEWALK COMPENSATION

- enter 8a ( starting the a fast calibration)  
TOT(0) or TOA(1) → enter 1  
(choose option 0 to start time calibration measurement)
- For the spacing how many pixel per row at the same time? 1,2,4,8,16 ?  
→ enter 8
- Shutter length: press 1 for short shutter (0-255 clock cycle) press 2 for long shutter (256- 65280 clock cycle)  
→ enter 1 (in the case of this thesis)
- What is the voltage you set at the external test pulser in mV?  
→ enter 30 (starting from 30 mV to 800 mV)
- After finishing the complete measurement with different voltage values, it is saved in a file with the name TOACalib.txt

### A.5 COMMANDS FOR TRIGGERED/UNTRIGGERED MEASUREMENT

- enter Run
- Do you want to use a defined run time (0) or a record a defined number (1)?  
enter 1 (choose trigger option for muons in this thesis)
- Number of triggers you want?  
enter e.g 1000 (any quantitative number of triggers you want)
- Shutter mode: untriggered (0) or triggered (1)  
enter 1
- shutter time: in [ $\mu$ s]  
enter calculated shutter time (considering parameters gas velocity, electric field, chamber length)

## A.6. List of other Commands

- Run mode: zero suppressed (o), complete matrix(1)  
enter **choose according to data saving type**
- After this data taking starts
- All data files are in ASCII format with txt extension and saved in a folder **data** with subfolders according to date and time of measurement

### A.6 LIST OF OTHER COMMANDS

- enter **1** (Reset the chip)
- enter **2** (Opening shutter window manually)
- enter **2s** (Close shutter window manually)
- enter **2z xxx** (for opening shutter window fro xxx units)
- enter **3** (Readout full matrix)
- enter **3a** (Readout o suppressed maximum 4096 hits)
- enter **4** (Set Matrix)
- enter **um** (Set uniform matrix: creates  $P_0$ ,  $P_1$  mask see Chapter 5)
- enter **LoadMatrix** (Load matrix from file matrix.txt)
- enter **SaveMatrix** (Save matrix to file matrix.txt)
- enter **LoadThreshold** (Load THL equalization values from file threshold.txt)
- enter **SetDAC x y** (Use to test THL value according to noise)



## LCIO PARAMETERISATION

---

### B.1 CALCULATION OF $d_0$

In this section the derivation of the track parameters will be presented. A line  $g$  in the three dimensional space can be defined as follows:

$$\vec{g}(x) = \begin{pmatrix} x \\ ax + b \\ bx + c \end{pmatrix} \quad (\text{B.1})$$

where the entry  $y(x) = ax + b$  represents the line in the  $x$ - $y$ -plane. From this one can see, that the slope  $a$  and the angle  $\phi$  is correlated with the following formula:

$$a = \tan(\phi) \quad (\text{B.2})$$

The origin of the coordinate system is equal to the origin of the Timepix chip. Due to this reason the distance  $d_0$  from the origin to the nearest point on the track can be calculated according to the following formula:

$$d_0 = \cos(\phi) \quad (\text{B.3})$$

### B.2 CALCULATION OF $z_0$

Since  $z_0$  is the vertical distance between this nearest point, with  $x_0$  as its assumed value, and the original track, the equation for  $z_0$  can be easily derived as follows:

$$z_0 = cx_0 + d \quad (\text{B.4})$$

## B. LCIO PARAMETERISATION

For finding  $x_0$  the (squared) distance between the origin and the track projection must be optimised according to the following calculation:

$$d^2 = x^2 + (y(x))^2 \quad (\text{B.5})$$

$$\Leftrightarrow d^2 = x^2 + (ax + b)^2 \quad (\text{B.6})$$

$$\Rightarrow \frac{d}{dx^2} d^2 = 0 \Leftrightarrow 2(a^2 + 1)x + 2ab = 0 \quad (\text{B.7})$$

$$\Rightarrow x_0 = \frac{abc}{a^2 + 1} \quad (\text{B.8})$$

$$\Rightarrow x_0 = \frac{abc}{a^2 + 1} \quad (\text{B.9})$$

$$\Rightarrow z_0 = \frac{abc}{a^2 + 1} + d \quad (\text{B.10})$$

$$(\text{B.11})$$

### B.3 CALCULATION OF $\lambda$

For calculating the angle  $\lambda$  between the track and the projection of the track the following equation can be taken into account:

$$\tan \lambda = \frac{z}{\sqrt{(x - x')^2 + (y - y')^2}} \quad (\text{B.12})$$

Here the variables  $x'$  and  $y'$  are the values for the point, where both lines intersect each other. Since this point must lie inside the  $x$ - $y$ , for  $z'$  must be 0 for this point, so it yields to the equation:

$$z' = cx' + d' = 0 \quad (\text{B.13})$$

with which  $x'$  can be written as:

$$x' = -\frac{d}{c} \quad (\text{B.14})$$

Inserting this result into the definition of  $y'$ , this leads to:

$$y' = -\frac{d}{c} + b \quad (\text{B.15})$$

Since equation (B.12) must be valid for all  $x$  and  $y$  values, one can set  $x = 0$ , which gives  $y = b$ . Putting this result into the equation (B.12), one gets:

$$\tan \lambda = \frac{c}{d/c\sqrt{a^2 + 1}} = \frac{d}{\sqrt{a^2 + 1}} \quad (\text{B.16})$$

B.4 CALCULATION OF  $\phi$ 

For calculating the angle  $\phi$  one has to parameterise the track line with  $y$  instead of  $x$ , which leads to the following formula:

$$\vec{g}(y) = \begin{pmatrix} ay + b \\ y \\ cy + d \end{pmatrix} \quad (\text{B.17})$$

From this one can derive the correlation between the slope  $a$  the angle  $\phi$  to:

$$a = \tan\left(\frac{\pi}{2} - \phi\right) \quad (\text{B.18})$$

which finally gives the following formula for the angle parameter  $\phi$ :

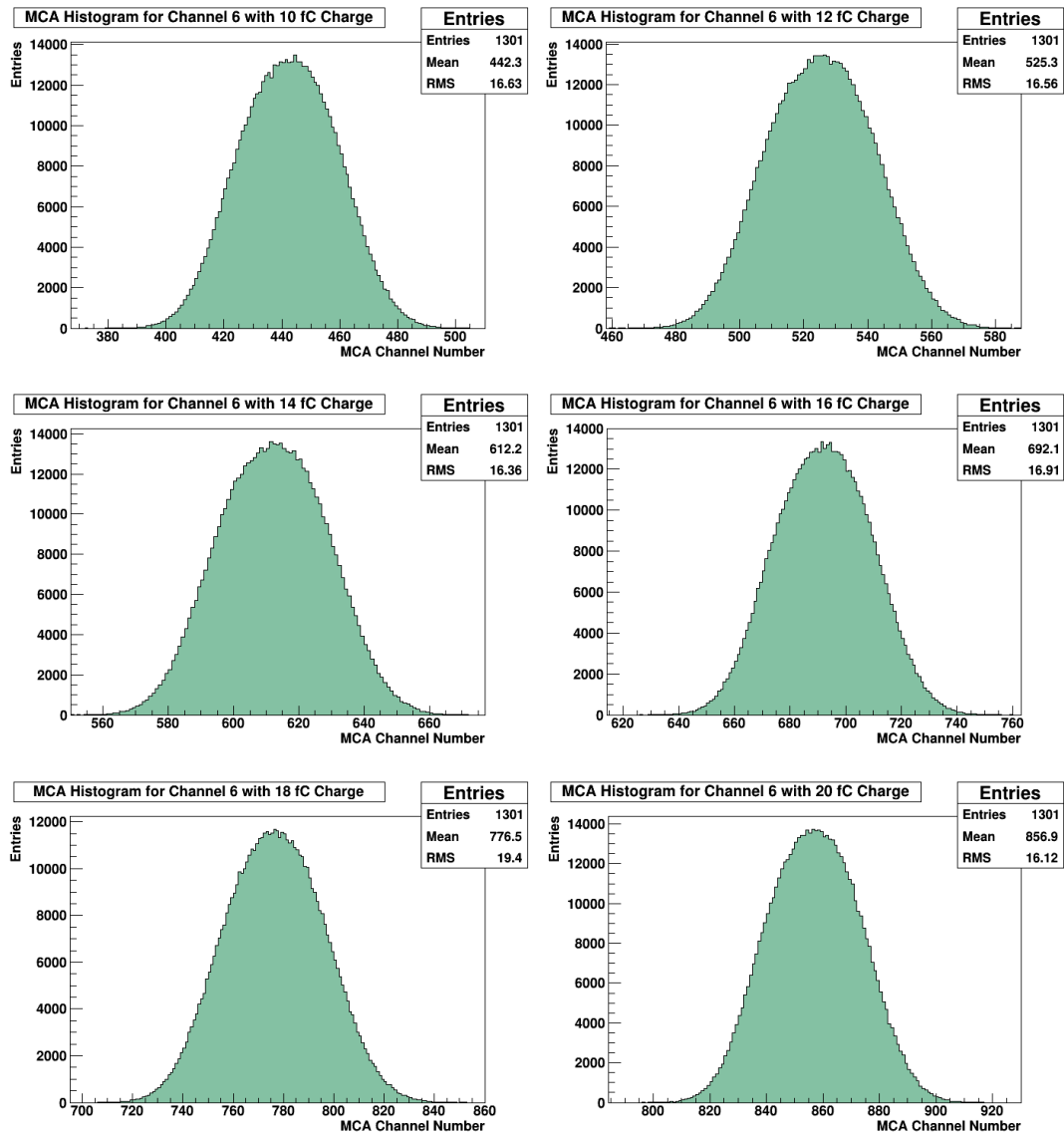
$$\phi = \frac{\pi}{2} - \arctan a \quad (\text{B.19})$$





## CALIBRATION AND MEASUREMENT RESULTS

### C.1 CHARGE CALIBRATION FOR TEST CHAMBER



### C. CALIBRATION AND MEASUREMENT RESULTS

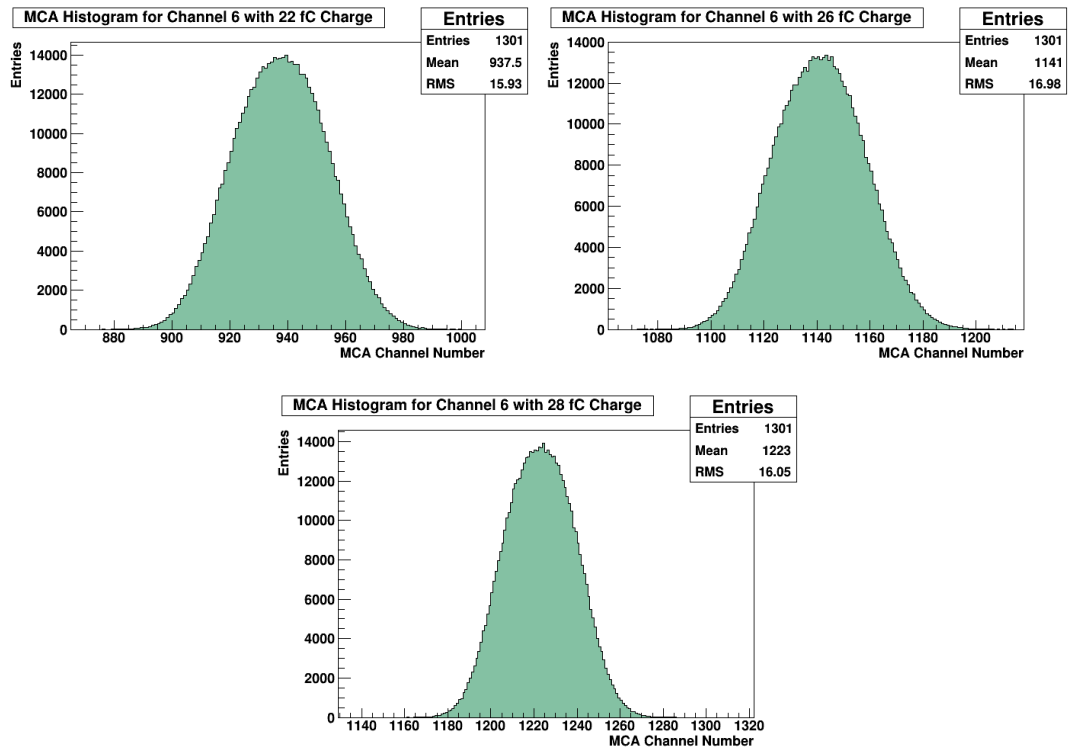


Figure C.1.: Complete calibration histograms for test chamber using one channel of the charge sensitive amplifier

## C.2. Charge Distributions for Different Voltages

### C.2 CHARGE DISTRIBUTIONS FOR DIFFERENT VOLTAGES

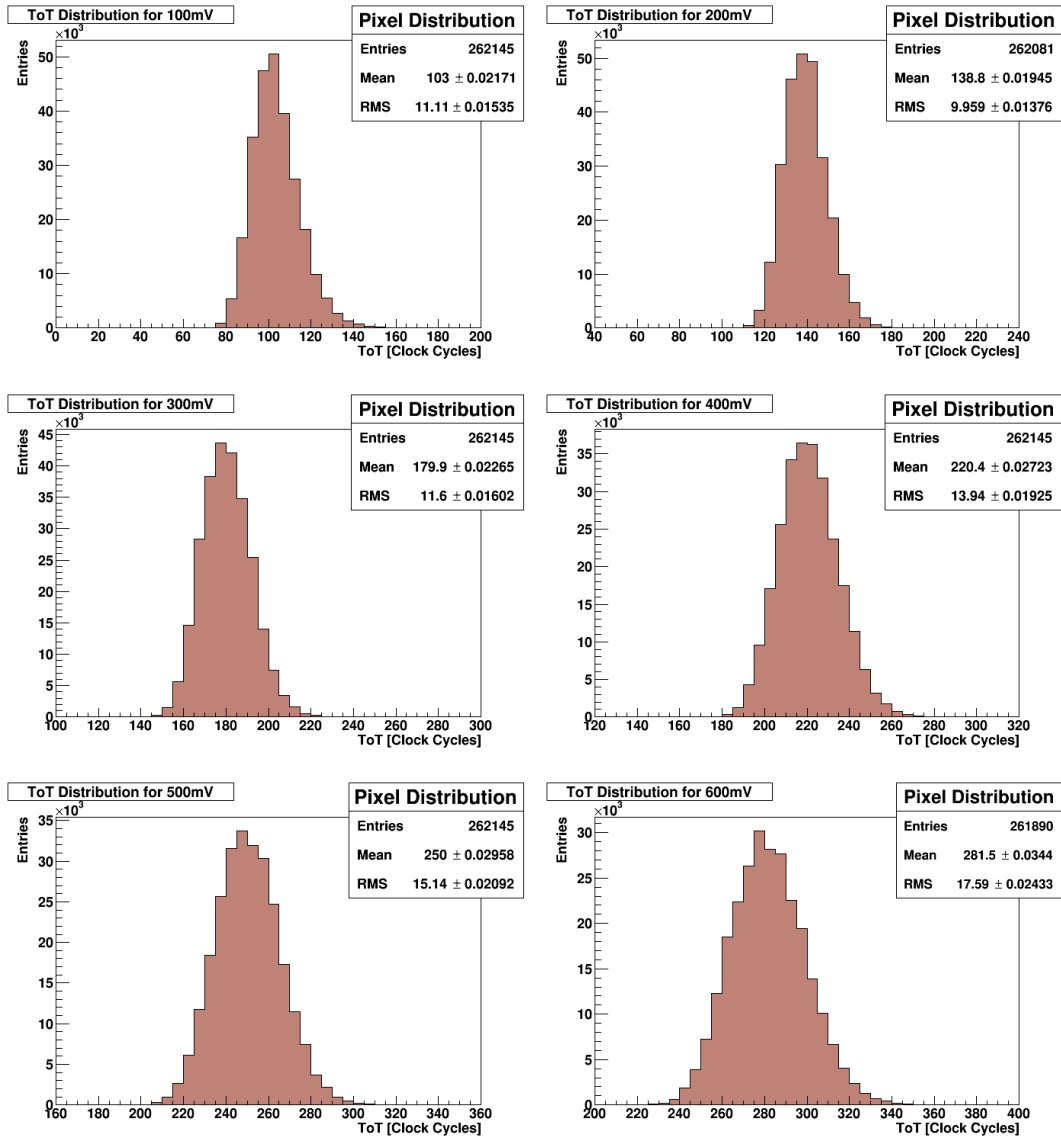


Figure C.2.: Complete measurement of *ToT* pixel distributions for different pulse heights

## C. CALIBRATION AND MEASUREMENT RESULTS

### C.3 TIME DISTRIBUTION FOR DIFFERENT VOLTAGES

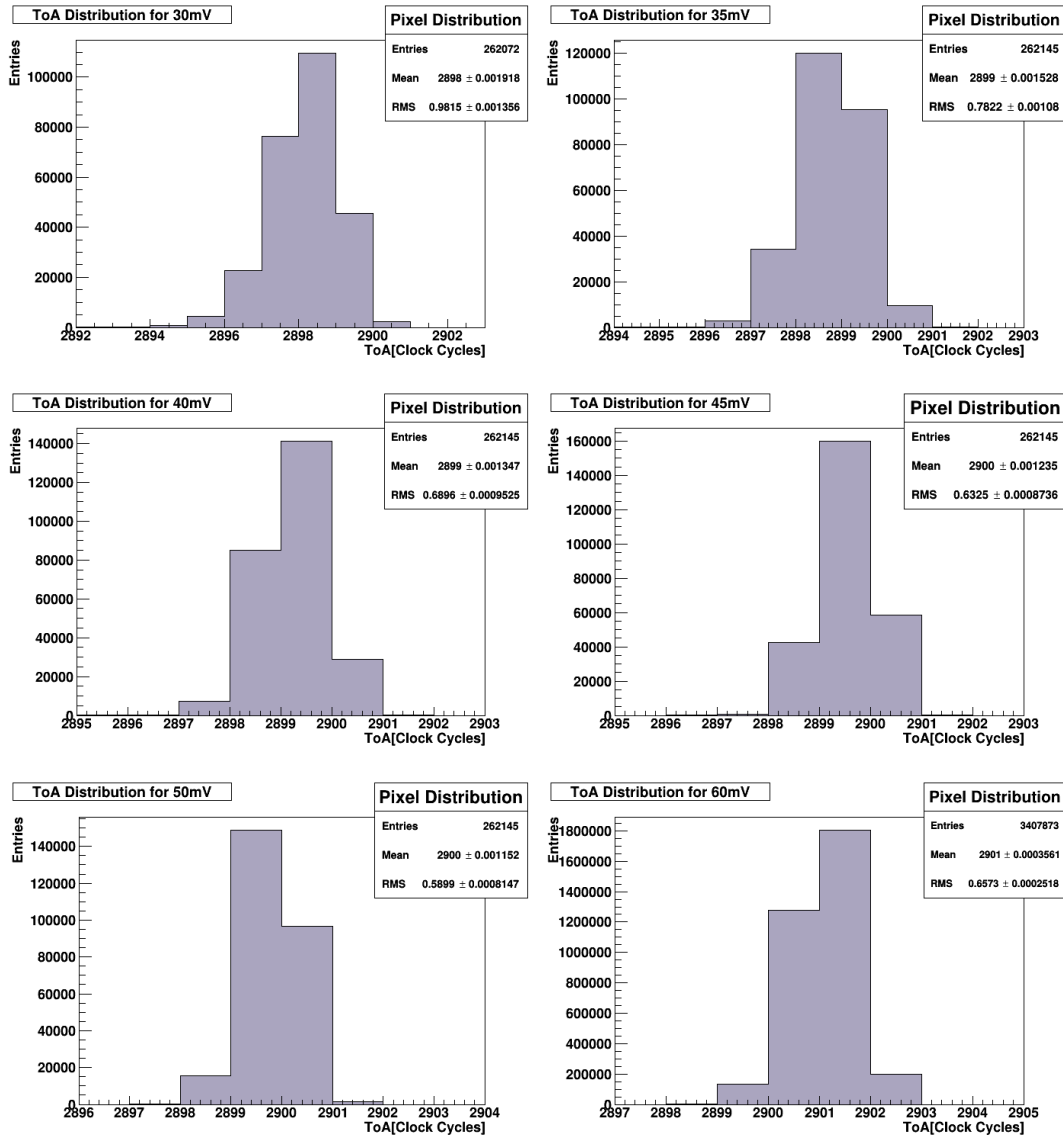


Figure C.3.: Calibration measurements of the *ToA* pixel distributions for different pulse heights

## TPC AT UNIVERSITY OF SIEGEN

## D.1 SMALL TEST CHAMBER

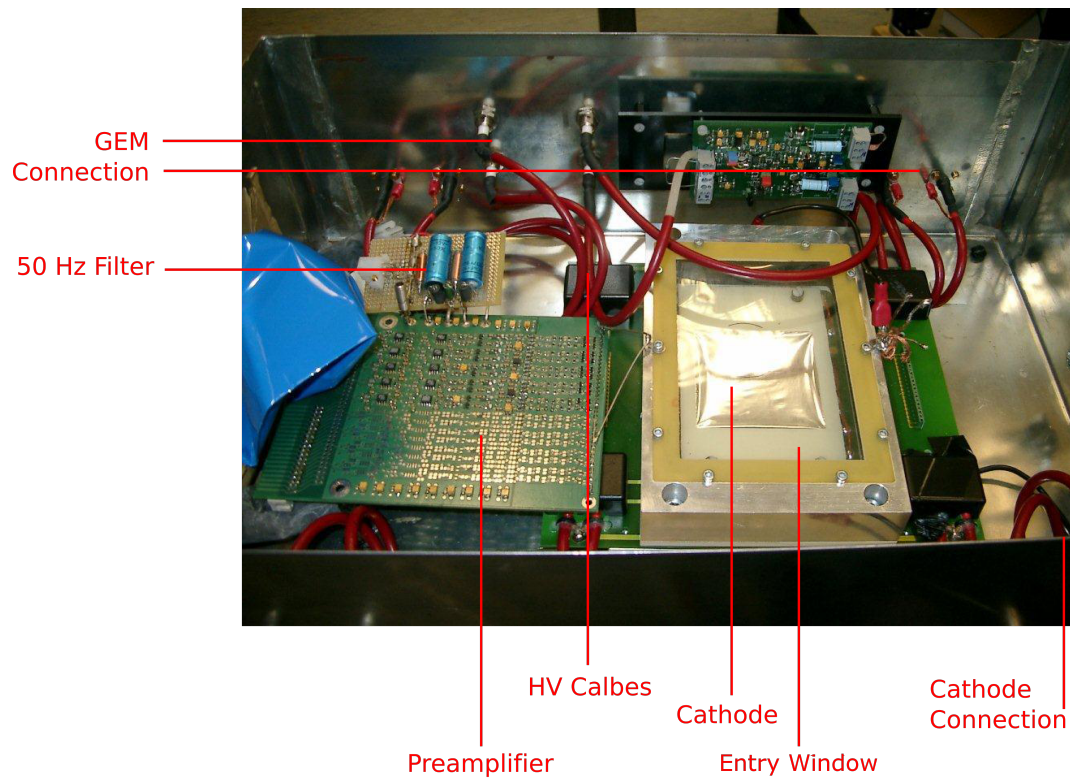


Figure D.1.: TPC test chamber at the University of Siegen including marks to all compenents. The 50 Hz filter is used to suppress noise from the power supply.

## D. TPC AT UNIVERSITY OF SIEGEN

### D.2 LARGE TPC PROTOTYPE

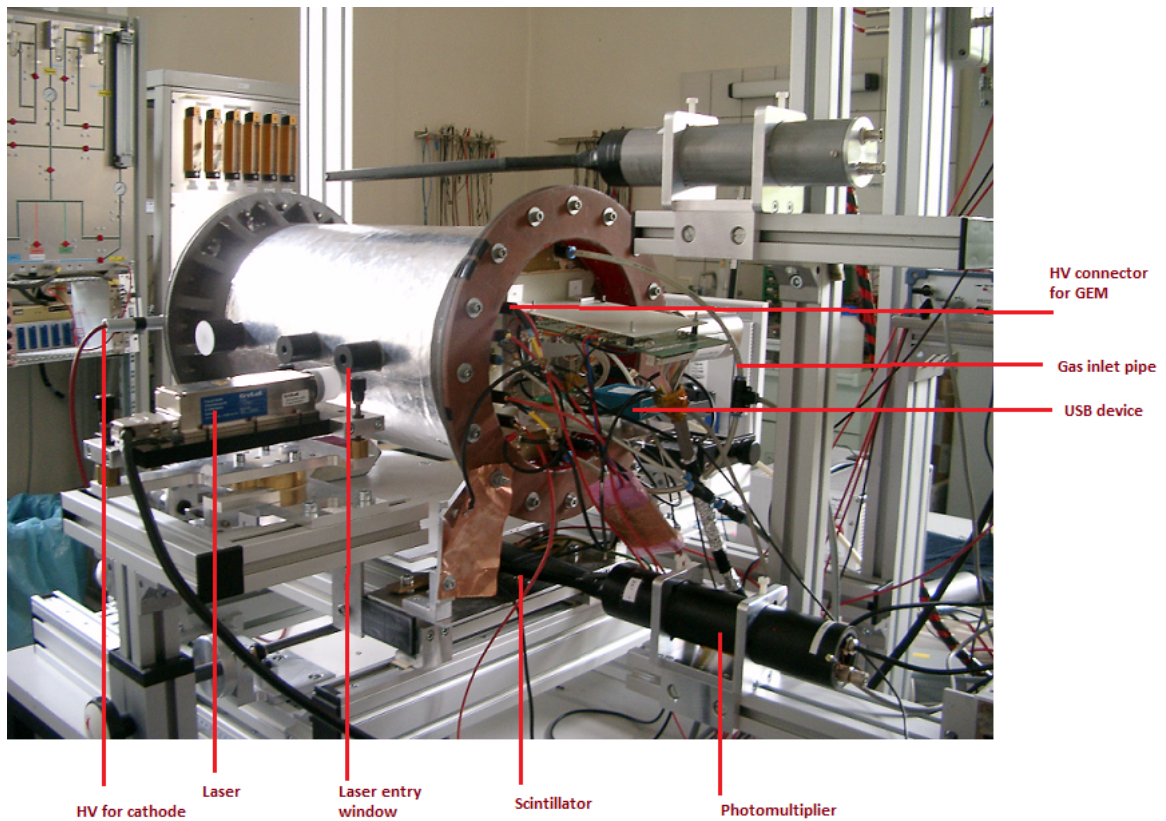


Figure D.2.: Large TPC prototype at the University of Siegen showing the setup for Muon measurements. Above and under of the TPC are the Scintillators of the hodoscope, while in front one can see the UV laser used for laser ionisation.

D.3. Printed Circuit Board as Base for Test Chamber

D.3 PRINTED CIRCUIT BOARD AS BASE FOR TEST CHAMBER

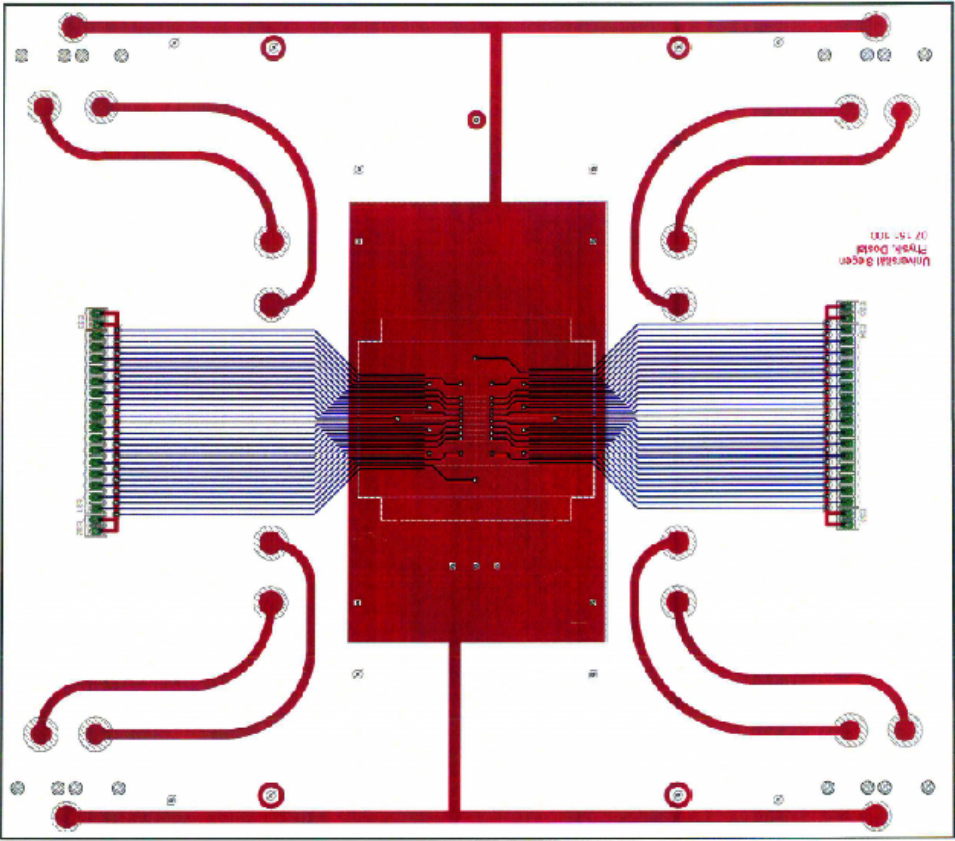


Figure D.3.: PCB with the pads for the test chamber. One can see the conductor path between the pads and the connectors for the amplifier.

D. TPC AT UNIVERSITY OF SIEGEN

D.4 VIRTEX 6 FPGA SETUP

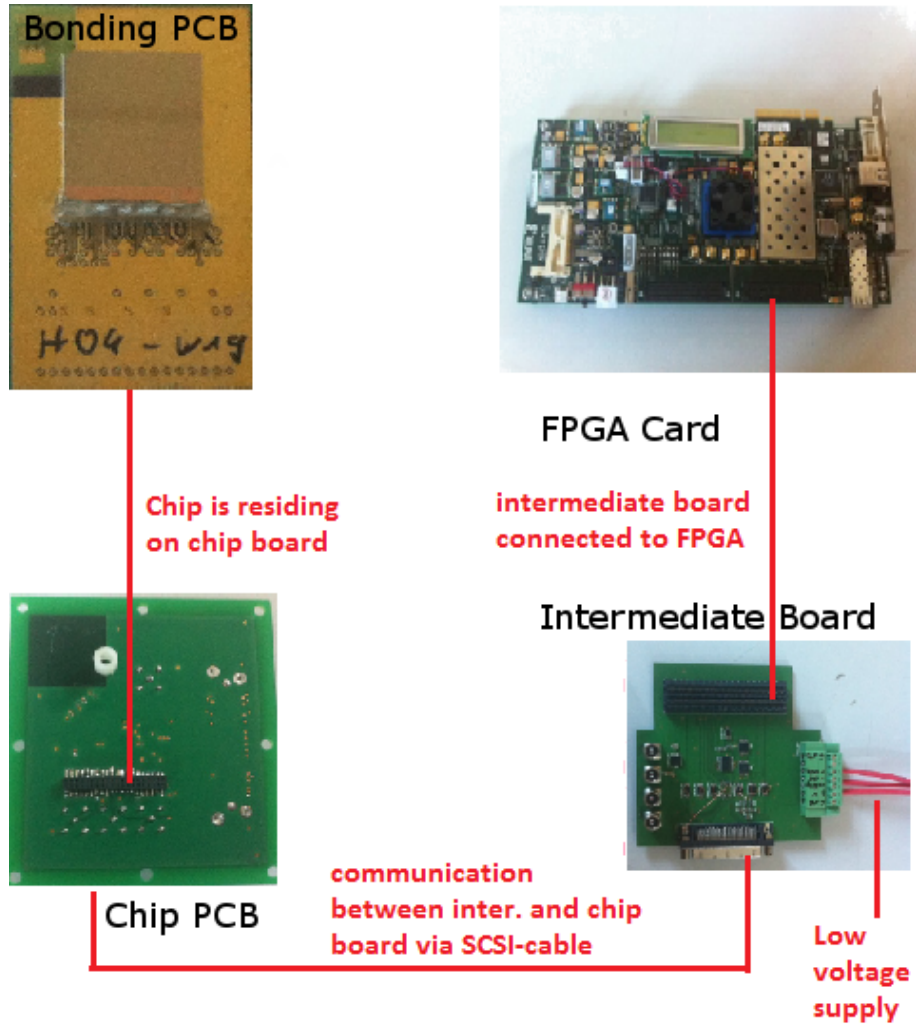


Figure D.4.: Connection scheme of the Timepix chip and the Virtex 6 FPGA card. The bonded Timepix chip is connected to the chip board, which communicates with the intermediate board via an SCSI cable. The intermediate board is directly placed on the FPGA card and supplied by two low voltage supplies.



## DATA WITH TPC PROTOTYPE

## E.1 DATA WITH VIRTEX 6 USING USING COSMIC MUONS

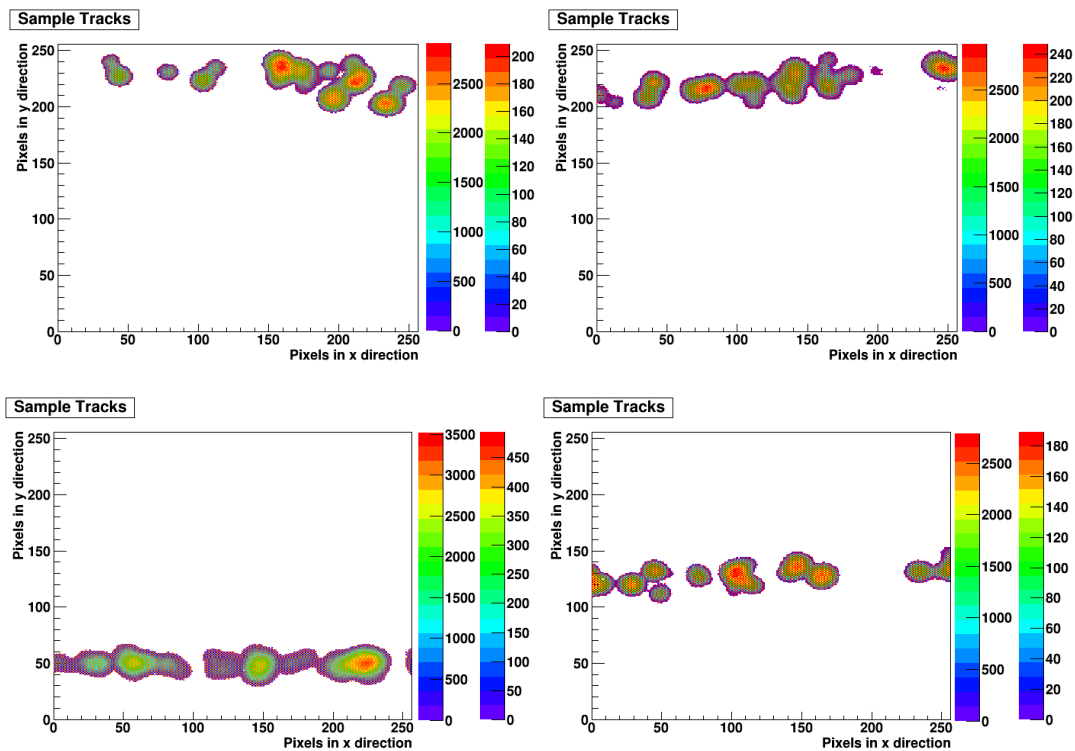


Figure E.1.: Sample tracks with cosmic muons using 3 carbon coated GEMs for ArCO<sub>2</sub> with a mixing ratio of 80:20. The shutter window was set to  $80.5\mu\text{s}$ . The left z-axis shows the values for the  $ToA$  pixels and the right axis the values for the  $ToT$  pixels



## CARBON COATING

### F.1 CORRELATION BETWEEN GAS GAIN AND TEMPERATURE RESP. PRES- SURE

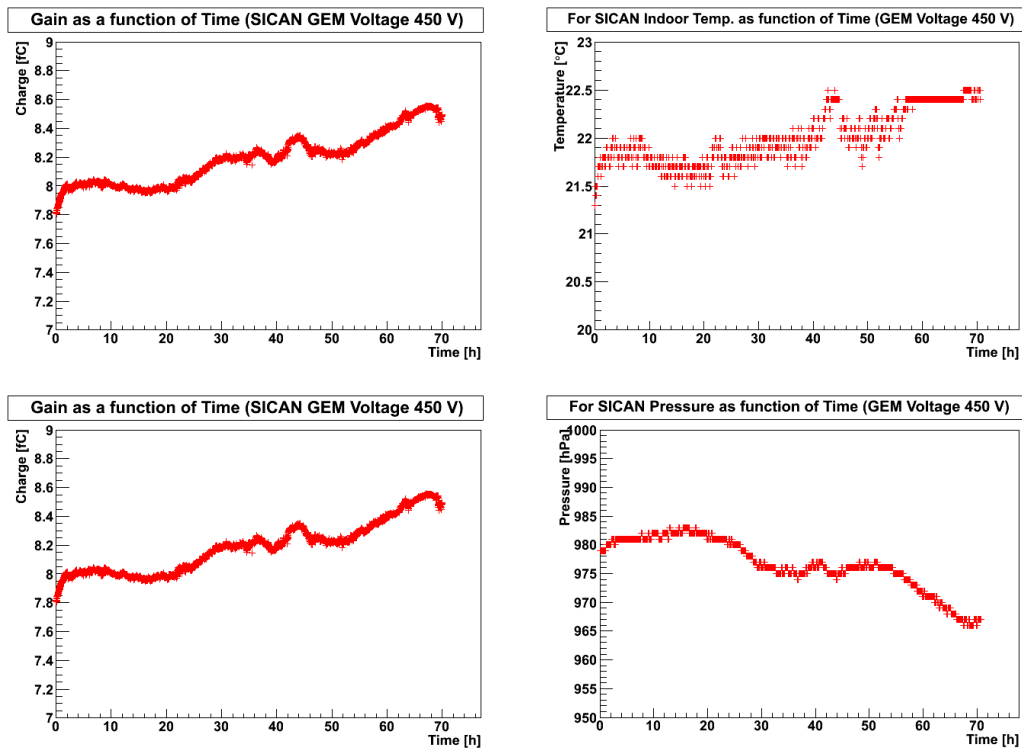


Figure F.1.: Correlation between gas gain and temperature resp. pressure for carbon coated SICAN GEMs with a GEM voltage of 450 V

## F. CARBON COATING

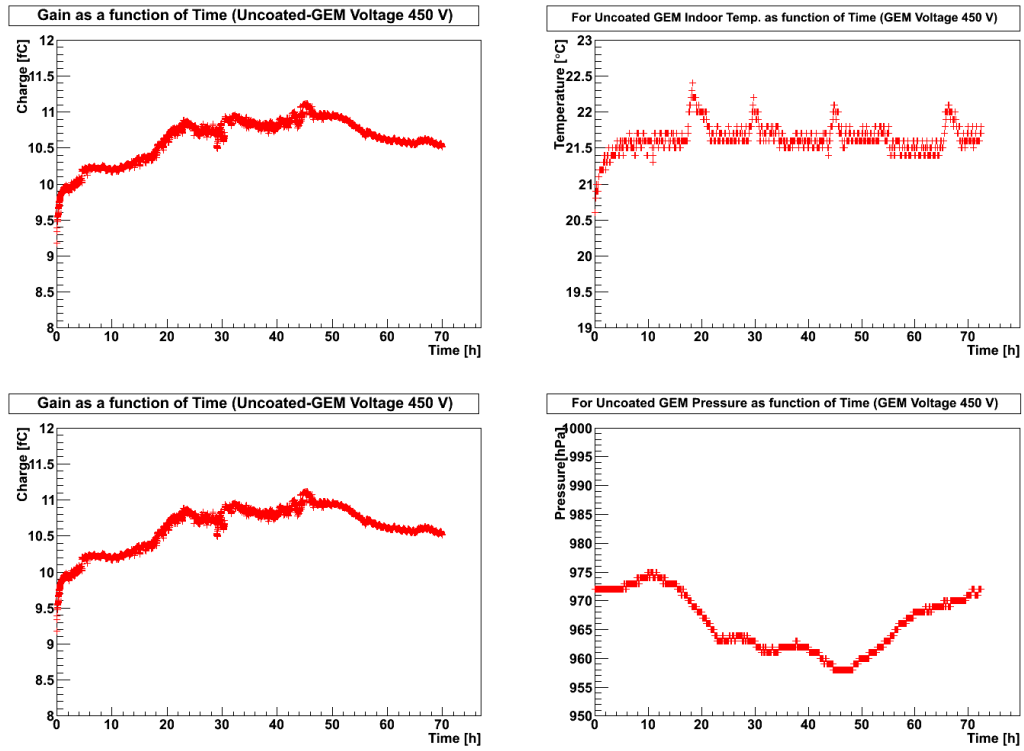


Figure F.2.: Correlation between Gas Gain and Temperature resp. Pressure for uncoated GEMs

## F.2. Correlation between Gas Gain and GEM Voltage

### F.2 CORRELATION BETWEEN GAS GAIN AND GEM VOLTAGE

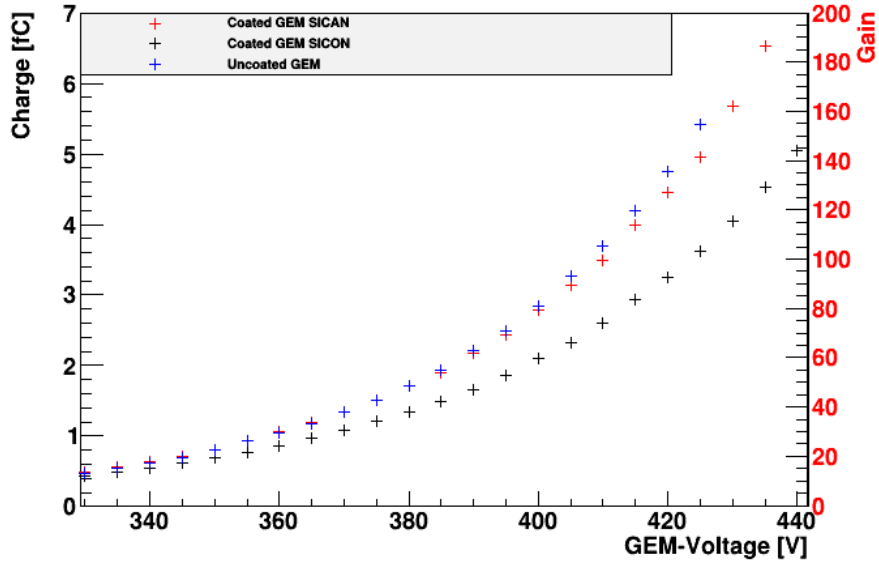



Figure F.3.: Comparison of GEMs with coated and uncoated surfaces. The gain of the SICAN coated GEM is slightly lower than the one for the uncoated GEM and much higher than the gain for the SICON coated GEM. At the end it was decided to make further investigations with the SICAN coated GEM.

## F. CARBON COATING

### F.3 SICON DATA SHEET



**Fraunhofer**  
IST

FRAUNHOFER-INSITUT FÜR SCHICHT- UND OBERFLÄCHENTECHNIK IST  
FRAUNHOFER INSTITUTE FOR SURFACE ENGINEERING AND THIN FILMS IST

### Schichtsystem SICON® (a-C:H:Si:O)

**Eigenschaften:**

Struktur	amorph
Dichte	1,3 – 1,5 g/cm <sup>3</sup>
Härte	7 – 9 GPa
E-Modul	60 – 90 GPa
Druckeigenspannungen	< 1 GPa
Reibkoeffizient trocken gegen Stahl	$\mu \leq 0,6$
Abrasivverschleiß (Al <sub>2</sub> O <sub>3</sub> )	etwa um den Faktor 3-4 niedriger der von 100Cr6 Lagerstahl (62 HRC)
Oberflächenenergie	ca. 24 mN/m (Wasserkontaktwinkel 95–105°)
Temperaturstabilität	300 – 350 °C
Thermischer Ausdehnungskoeffizient	$2 - 3 \times 10^{-6} \text{ K}^{-1}$ (a-C:H)
Wärmeleitfähigkeit	ca. $10^{-2} \text{ W cm}^{-1} \text{ K}^{-1}$ (a-C:H)
Elektrischer Widerstand	$> 10^{10} \Omega \text{ cm}$
Dielektrische Konstante	1 – 3 (a-C:H)
Durchschlagsspannung	100 – 200 V $\mu\text{m}^{-1}$
Brechungsindex	1,7 – 1,9 ( $\lambda$ : 200 – 400 nm)
Typische Schichtdicke	0,5 – 5 $\mu\text{m}$
Abscheidetemperatur	< 200 °C

**Größte verfügbare Beschichtungsanlage:**

Kammervolumen	1 m <sup>3</sup>
Kammerdurchmesser	900 mm
Kammerhöhe	1400 mm
Beschichtungsvolumen	max. Ø 700 mm, Höhe 1100 mm
Max. Bauteilgewicht	800 kg

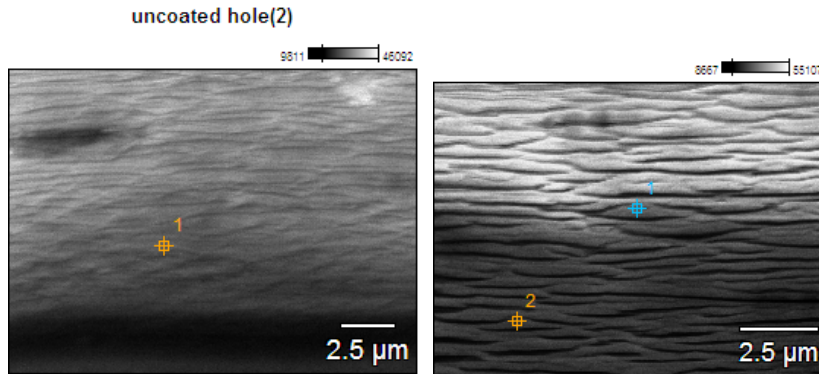
Fraunhofer-Gesellschaft zur Förderung der angewandten Forschung e.V., München  
**Vorstand**  
Univ.-Prof. Dr.-Ing. habil. Prof. e.h. mult. Dr. h.c. mult. Hans-Jörg Bullinger, Präsident  
Prof. Dr. rer. nat. Ulrich Buller  
Dr. rer. pol. Alfred Gossner  
Prof. Dr. phil. Marion Schick

**Bankverbindung** Deutsche Bank, München  
**Konto** 752193300 BLZ 700 700 10  
**IBAN** DE86 7007 0010 0752 1933 00  
**BIC (SWIFT-Code)** DEUTDE33  
**USt-IdNr.** DE129515865  
**Steuernummer** 143/215/20392

Figure F.4.: Datasheet of SICON [Fra14]

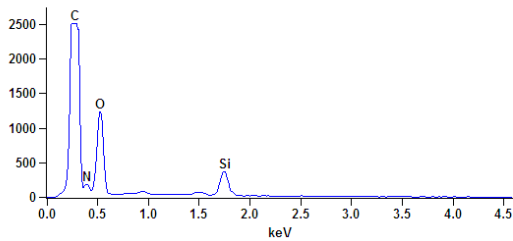
## F.4. Carbon Coating inside GEM Holes

### F.4 CARBON COATING INSIDE GEM HOLES

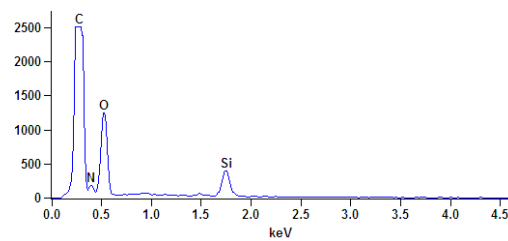


(a) Microscopic analysis of an uncoated hole

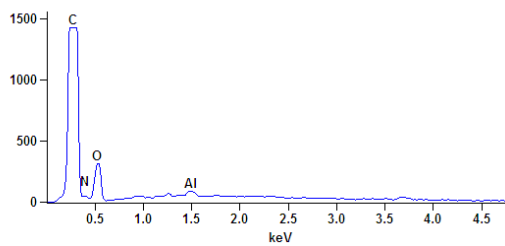
(b) Microscopic analysis of a SICON coated hole. Point 1 and 2 identify the two measurement points.



(c) Analysis of a SICON coated hole at measurement point 2



(d) Analysis of a SICON coated hole at measurement point 1



(e) Analysis of an uncoated hole. The peak of Aluminium cannot be explained by the structure of Kapton or SICON. It is very likely, that it comes from test chamber case, since these GEMs have been used before.

Figure F.5.: Measurements to prove the carbon coating inside the GEM holes





## BIBLIOGRAPHY

---

- [AAA02] C. Grimani et al.: *Measurements of the absolute energy spectra of cosmic-ray positrons and electrons above 7 GeV*, A&A, Volume 392, Number 1, September II 2002, Pages 287–294
- [Aar07] G. Aarons et al.: *International Linear Collider Reference Design Report*, Volume 2: Physics at the ILC, 2007, arXiv:0709:1893
- [Acc07] International Linear Collider Reference Design Report: *Detectors*, August 2007
- [ACF13] ACFA Working Group Webpage. <http://acfahep.kek.jp/> Accessed, 2013.
- [Ack09] K. Ackermann *Cosmic Ray Tests of the Prototype TPC for the ILC Experiment*, 2009, arXiv:0905.2655 [physics.ins-det]
- [Ans14] Ansys Workbench: <http://www.ansys.com/Products/Workflow+Technology/ANSYS+Workbench+Platform>, 2014.
- [Aou13] Rafael Aoude, Daniel Pitzl: *Study of CMS Pixel Sensors*, DESY Summer Student, 2013
- [ATL12] The ATLAS Collaboration: *Observation of a New Particle in the Search for the Standard Model Higgs Boson with the ATLAS Detector at the LHC*, Physics Letter B, 716:1 - 29, 2012
- [Bae12] H. Baer, J. List: *Post LHC7 SUSY benchmark points for ILC physics*, 2012, arXiv:1205.6929
- [Bar07] B. Barrish et al.: *Reference Design Report*, ILC-Report-2007-001, August 2007
- [Bei98] S. Beirle: *Carbon Coated Gas Electron Multipliers*, University of Siegen, 1998, physics/9807039
- [Ber13] J. Beringer et al. (Particle Data Group): *Review of particle Physics*, Physical review D, 86, 2012. <http://pdg.lbl.gov> , 2013
- [Bew11] Klaus Bewilogua et al.: *Easy-clean surfaces built to order*, European Coatings Journal, May 2011, Pages 24–29

## Bibliography

- [BGK05] H. Bichsel, D.E. Groom and S.R. Klein: *Passages of particles through matter*, <[http://pdg.lbl.gov/2005/reviews/contents\\_sports.html](http://pdg.lbl.gov/2005/reviews/contents_sports.html)>, Review, 2005
- [Bia11] Stephen Biagi: *Magboltz -Transport of Electrons in Gas Mixtures*, <<http://wwwconsult.cern.ch/writeup/magboltz/>>, 2011
- [Bie08] Adeline Bieker: *Aufbau eines Szintillator - Hodoskops für kosmische Myonen*, Bachelorthesis, University of Siegen, 2008
- [Blu93] W. Blum and L. Rolandi: *Particle Detection with Drift Chambers*, Springer-Verlag, 1993
- [Blu94] W. Blume, K. Rolandi: *Particle Detection with Drift Chambers*, Springer-Verlag, Berlin, Heidelberg, New York, 1994
- [Bow95] Ch. K. Bowdery: *The AlePH handbook*, CERN, Geneva, 1995
- [Brz13] Christoph Brezina: *A GEM Based Time Projection Chamber with Pixel Readout*, PhD Thesis, University of Bonn, 2013
- [CDF12] The CDF and DØ Collaboration: *Evidence for a particle produce in association with weak bosons and decaying to a bottom-antibottom quark pair in Higgs boson searches at Tevatron*, Physical Review Letters, 109, 2012.  
arXiv:1207.6436
- [ChT14] Chem Tube 3D: <[http://http://www.chemtube3d.com/polymer/\\_KaptonF.html](http://http://www.chemtube3d.com/polymer/_KaptonF.html)>, 2014
- [CMS12] The CMS Collaboration: *Observation of a New Boson at a Mass of 125 GeV with the CMS Experiment at the LHC*, Physics Letter, 716:30, 2012
- [Cry14] Crylas: [http://www.crylas.de/products/pulsed\\_laser.html](http://www.crylas.de/products/pulsed_laser.html), Laser manufacturer, 2014
- [Del00] G. Dellacasa et al.: *ALICE Technical Design Report of the Time Projection Chamber*, CERN - OPEN - 2000 - 183
- [Din07] Michael Dine: *Supersymmetry and String Theory: Beyond the Standard Model*, Cambridge University Press, 2007
- [Fer86] Richard Fernow: *Introduction to Experimental Particle Physics*, Cambridge University Press, 1986

- [FLC11] FLC - Forschung mit Lepton Collidern: <<http://www-flc.desy.de>>, 2011
- [Fra14] Fraunhofer Institute for Surface Engineering and Thin Films: <<http://www.ist.fraunhofer.de/en.html>>, 2014
- [Gar14] Garfield: <<http://garfield.web.cern.ch/garfield/>>, 2014
- [Gau08] Bakul Gaur: *First studies of a prototype GEM readout for a future ILC-TPC*, PhD Thesis, University of Siegen, 2008
- [GDG10] Gas Detector Development Group CERN: <<http://gdd.web.cern.ch/GDD>>, September 2010
- [Gio96] Y. Giomataris: *MICROMEGAS: a high-granularity position-sensitive gaseous detector for high particle-flux environments*, Nuclear Instruments and Methods in Physics Research Section A: Accelerators, Spectrometers, Detectors and Associated Equipment, Volume 376, Issue 1, June 21 1996, Pages 29–35
- [Grfo7] David Griffith: *Introduction to Electrodynamics*, 3rd Edition, Pearson Education, Dorling Kindersley, 2007
- [Grfo8] David Griffith: *Introduction to Elementary Particle Physics*, Wiley-VCH Verlag GmbH & Co. KGaA, 2008
- [Grp08] C. Grupen, B. Schwartz: *Particle Detectors*, 2nd edition, Cambridge University Press, 2008
- [Gru99] Magali Gruwe: *Gas Studies for a TPC of a Detector for the Future Linear Collider TESLA*, 1999. LC-DET-1999-003-TESLA
- [Hal03] David Halliday: *Physik*, 2003
- [Heb02] Thomas Hebbeker, Charles Timmermans: *A Compilation of High Energy Atmospheric Muon Data At Sea Level*, Astroparticle Physics, Volume 18, Issue 1, August 2002, Pages 107 – 127
- [Hei13] Isa Heinze: *Development of a Hough Transformation Track Finder for Time Projection Chambers*, PhD Thesis, DESE-THESIS-13-055, DESY, Hamburg, 2013
- [Hig64] P. W. Higgs: *Broken Symmetries, Massless Particles and gauge Fields*. Physics Letters, 12:132, 1964

## Bibliography

- [Hig66] P. W. Higgs: *Spontaneous Symmetry Breakdown without Massless Bosons*. *Physical Review*, 145:1156, 1966
- [HLi10] H. Li: *Higgs Recoil Mass and Higgs-strahlung Cross-Section Study for the ILD LOI*, 2010, arXiv:1007.2999
- [Hqe14] Institute for High Frequency and Quantum Electronics: [<https://www.hqe.eti.uni-siegen.de/>](https://www.hqe.eti.uni-siegen.de/), 2013
- [Hua12] P. Huang, X. Tata, H. Baer, V. Barger: *Natural Supersymmetry: LHC, dark matter and ILC searches*, 2012, arXiv:1203.5539
- [ILC13] Website of the Linear Collider: [<http://www.linearcollider.org/>](http://www.linearcollider.org/), 2013
- [ILC132] *The International Linear Collider Technical Design Report, Volume 4: Detectors*, 2013. CERN-ATS-2013-037, DESY 13-062, ILC-Report-2013-040
- [Kilo6] Martin Killenberg: *Resolution Studies of a GEM-Based TPC*, PhD Thesis, RWTH Aachen 2006
- [Koh10] Markus Köhli: *Charakterisierung postprozessierter TimePix-Chips*, Masterthesis, Freiburg, 2010
- [Krao8] Thorsten Krautscheid: *Simulation zur Ionenrueckdrift in einer Zeit-Projektionskammer am ILC*, Diploma thesis, University of Bonn, 2008
- [Kro12] Viola Kroner: *Signal Development and Pad-Size Studies in a GEM TPC with pixel readout*, Masterthesis, University of Bonn, 2012
- [Lah07] Robert Lahmann: *Experimentelle Methoden der Teilchen- und Astroteilchenphysik*, Lecture of University of Erlangen, [<http://www.ecap.nat.uni-erlangen.de/members/lahmann/lehre/exp\\_meth\\_ss07.html>](http://www.ecap.nat.uni-erlangen.de/members/lahmann/lehre/exp_meth_ss07.html)
- [Lea10] H. Lea: *Analysis of GEM Properties and Development of a GEM Support Structure for the ILD Time Projection Chamber*, DESY-THESIS-2010-015, April 2010
- [Leo94] W. R. Leo: *Techniques of Nuclear and Particle Physics Experiments, A how to Approach*, Berlin: Springer, pages 368p., 1994
- [Llo06] X. Llopart: *Timepix Manual v1.0*, August 2006, CERN

- [Loh92] T. Lohse and W. Witzeling: *The Time Projection Chamber*, Adv. Ser. Direct. High Energy Phys. 9, pages 81–155,
- [Loto6] Sven Lotze: *Ion Backdrift Minimisation in a GEM-Based TPC Readout*. PhD thesis, University of Aachen, 2006
- [Lot14] Chair of Surface and Materials Technology: <http://www.mb.uni-siegen.de/lot/index.html.en?lang=en>, 2014
- [Lup14] Michael Lupberger: *The Pixel-TPC: first results from an 8-InGrid module*, University of Bonn, 2014, arXiv:1311.3125
- [Mar14] Marlin: [http://ilcsoft.desy.de/portal/software\\_packages/marlin/](http://ilcsoft.desy.de/portal/software_packages/marlin/), 2014
- [Med14] Medipix: <http://medipix.web.cern.ch/medipix/>
- [Nik14] Website of Nikhef: <http://medipix.web.cern.ch/medipix/>, 2014
- [Nyg74] D.R. Nygren: *Time Projection Chamber: A New 4 Pi Detector for Charged Particles*, Lawrence Berkeley Laboratory, 1974
- [PhL64] P. W. Higgs: *Broken Symmetries, Massless Particles and Gauge Fields*, Physics Letter, Volume 12, Issue 2, 1964
- [Pix13] Pixelman Software: <http://aladdin.utef.cvut.cz/ofat/others/Pixelman/Pixelman.html>, 2013
- [Pla13] Planck Collaboration: *Planck 2013 results. XVI. Cosmological parameters*. 2013
- [PoPo7] N. J. Carron: *An Introduction to the Passage of Energetic Particles through Matter*. Taylor & Francis Group, New York, 2007
- [PTE14] Periodic Table of Elements: <http://environmentalchemistry.com/yogi/periodic/Sr-pg2.html>, 2014
- [Sad80] B. Sadoulet and J. Bourotte: *Ionizing of Multiwire Proportional Chamber Gas by Double Photon Absorption*, Nuclear Instruments and Methods 173, 1980, pages 463–470
- [Sau03] F. Sauli: *Development and Application of Gas Electron Multipliers Dectectors*. Nuclear Instruments and Methods, A 505, 2003

## Bibliography

- [Sch11] Marc Schmidt: *Untersuchungen an einer TPC mit einer GEM als Gasverstärkung und Programmierung zugehöriger Simulationen*, Masterthesis, University of Siegen, 2011
- [Sha98] A. Sharma: *Properties of some gas mixtures used in tracking detectors*, In: *SLAC- Journal-ICFA* 16.3 (1998)
- [Sil05] G. Bertone, D. Hooper, J. Silk. *Dark matter: Evidence, Candidates and constraints*. *Physics Reports*, 405:279, 2005
- [Sli77] F. Sauli: *Principle of Operation of Multiwire Proportional and Drift Chambers*, Lectures at Cern, Geneva, 1977
- [Sob02] B. Sobloher: *Simulationstudien zu GEM-Folien für die Auslese einer TPC*, Master Thesis, TPC Group Aachen, 2002
- [Str74] A. Salam and J. Strathdee: *Super-symmetry and non-abelian gauge*. *Physics Letters B*, 51, 1974
- [TDR13] *The International Linear Collider Technical Design Report, Volume 4: Detectors*, 2013. CERN-ATS-2013-037, DESY 13-062, ILC-REPORT-2013-040
- [TES01] TESLA Technical Design Report, Part IV: *A Detector For TESLA*, DESY 2001-011, ECFA 2001-209 (2001).
- [Ulm11] Radion Ulmann: *Calibration of the Timepix Pixel Chip for the Readout of Gaseous Particle Detectors*, Masterthesis, University of Bonn, 2011
- [Ulr11] Ulrich Stroth: *Online-Skript Physik III*  
<<http://www.ipf.uni-stuttgart.de/lehre/online-skript/quant1/wq2.gif>>, 2011
- [Umme08] Martin Ummenhofer: *Inbetriebnahme einer Zeitprojektionskammer mit Pixel-Auslese*, Diplomathesis, University of Bonn, July 2008
- [Ung91] Eugen Unger: *Die Erzeugung dünner Schichten. Das PECVD-Verfahren: Gasphasenabscheidung in einem Plasma*, *Chemie in unserer Zeit*, Volume 25, Issue 3, pages 148–158, June 1991
- [Wei04] Steven Weinberg: *The Making of the Standard Model*, 2004, arXiv:hep-ph/0401010
- [Wie07] Peter Wienemann et al.: *MarlinTPC: A Marlin based common TPC software framework for the LC-TPC collaboration*, 2007

- [Vyk14] Zdenek Vykydal: <[http://aladdin.utef.cvut.cz/ofat/others/USB\\_Interface/USB\\_Interface.html](http://aladdin.utef.cvut.cz/ofat/others/USB_Interface/USB_Interface.html)>, 2014
- [Yao06] Wand Yao et al. *Review of Particle Physics*. Journal of Physics, G, 33, 2006
- [Zim98] Simone Zimmermann: *Data Reconstruction and Analysis of GEM-Based Time Projection Chambers with Pixel Readout*, Diploma thesis, University of Bonn, 1998
- [Zum74] J. Wess and B. Zumino: *A Lagrangian Model Invariant under Super-gauge Transformations*. Physics Letters B, 49, 1974